IPP-Report

Max-Planck-Institut
für Plasmaphysik

Christian Karl Kiefer

Application of theory-based transport models on tokamak plasmas with different main ion species

IPP 2021-02
Januar 2021

Max Planck Institute
for Plasma Physics

ulm university universität
uulm

Faculty of Natural Sciences

Application of theory-based transport models on tokamak plasmas with different main ion species

Master Thesis at Ulm University

Author:
Christian Karl Kiefer
christian.kiefer@uni-ulm.de
Student number: 830643

Examiners:
Apl. Prof. Dr. Emanuele Poli
Prof. Dr. Johannes Hecker Denschlag

Supervisor:
Dr. Clemente Angioni

2020

Version November 8, 2020

Typesetting system: PDF-LaTeX 2_ε

Contents

1 Introduction

ITER, the International Thermonuclear Experimental Reactor, will be the next step pushing forward the limits of nuclear fusion technology. It aims to produce $500\ \mathrm{MW}$ of fusion energy with only $50\ \mathrm{MW}$ of auxiliary heating power. If this energy was injected into the German electricity grid, it would be enough for the peak consumption of about a half million German citizens.
The First Pre-Fusion Power Operation (PFPO-1) phase already aims to establish plasmas in the high-confinement mode although only a very limited amount of auxiliary heating power will be available at this early stage. Reliable predictions of transitions to this high-confinement regime require precise predictions of the ion heat flux close to the edge of the plasma. Furthermore, accurate estimates of central electron temperatures are necessary for the prediction of third harmonic absorption of EC radiation. In plasmas with dominant electron heating, edge ion heat fluxes as well as central electron temperatures are almost fully determined by turbulent particle and heat transport in the core plasma.
Nonlinear gyrokinetic codes provide very precise calculations of local turbulent transport fluxes, but with enormous computational effort of several millions of CPU hours even for a single time step. Quasi-linear transport models such as TGLF and QuaLiKiz allow for significantly faster computations by employing reduced physics models. This master thesis presents a validation of these two quasi-linear transport models against experimental results from ASDEX Upgrade and JET and against a set of linear gyrokinetic simulations performed with GKW.

2 Basic principles of tokamaks

2.1 Toroidal magnetic confinement

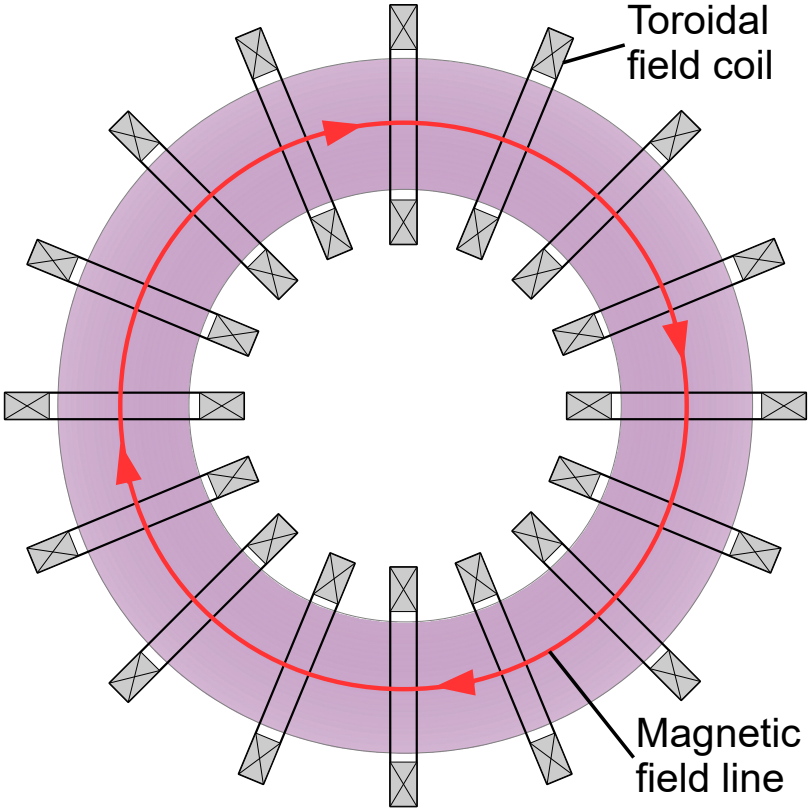

Figure 2.1: Scheme of a toroidal magnetic confinement machine with 16 toroidal field coils (like in ASDEX Upgrade).

The idea of magnetic confinement fusion is to confine a hot plasma of deuterium and tritium ions in a magnetic cage from which charged particles cannot escape. Several magnetic configurations have been tested in the past with respect to their

confinement properties. Since linear configurations like the θ-pinch and the mirror machine suffer from too large particle losses at their ends, modern-day machines like the tokamak and the stellarator bend the magnetic field lines into a ring shape (see figure 2.1).
Two consequences of the ring shape are the curvature of the field lines and the inhomogeneity of the magnetic field strength [51]. To demonstrate the inhomogeneity of the magnetic field strength, we will first consider a hypothetical device with a purely toroidal magnetic field ($B = B_t$). Integrating Ampère's law

$$\vec{\nabla} \times \vec{B} = \mu_0 \vec{j} \tag{2.1}$$

over a circular area with radius R, for which the contour follows a magnetic field line inside the plasma (see figure 2.1) leads to the following expression for the magnetic field:

$$B(R) = \frac{\mu_0 I}{2\pi R} \propto \frac{1}{R}. \tag{2.2}$$

In this equation, μ_0 denotes the vacuum permeability and I the total current of all toroidal field coils. Since in all tokamaks, the toroidal magnetic field B_t is dominant, the $1/R$-dependence holds approximately also in real machines.
Another simplification made here are the perfectly circular magnetic field lines. Due to a discrete number of toroidal field (TF) coils (for example in JET, there are 32 TF coils and in ITER, there will be only 18 TF field coils), the magnetic field strength in a real machine is not perfectly axisymmetric. At one third field operation in ITER ($B_t = 1.8\,\mathrm{T}$ and $I_p = 5\,\mathrm{MA}$) in the second Pre-Fusion Power operation phase, a comparably large magnetic field ripple of $\delta_{\mathrm{rip}} := (B_{max} - B_{min})/(B_{max} + B_{min}) \approx 1.3\%$ is expected [76]. Such large magnetic field ripples are always an area of concern since this leads to enhanced particle losses.

2.2 Magnetic confinement in a tokamak

In a purely toroidal magnetic field ($B = B_t$), the grad-B drift [54]

$$\vec{v}_{\nabla B} = \frac{m v_\perp^2}{2} \cdot \frac{\vec{B} \times \vec{\nabla} B}{q B^3} \tag{2.3}$$

resulting from the inhomogeneity of the B-field (see equation 2.2) and the curvature drift

$$\vec{v}_{\mathrm{curv}} = m v_{\parallel}^2 \cdot \frac{\vec{B} \times (\vec{B} \cdot \vec{\nabla})\vec{B}}{qB^4} \tag{2.4}$$

due to the curved magnetic field lines would lead to a charge separation in the plasma. In these equations, m and q denote the mass and the charge of the considered particle, respectively. The velocity is split up into a velocity parallel to the field lines $v_{\parallel}$ and a velocity perpendicular to the field lines $v_{\perp}$.

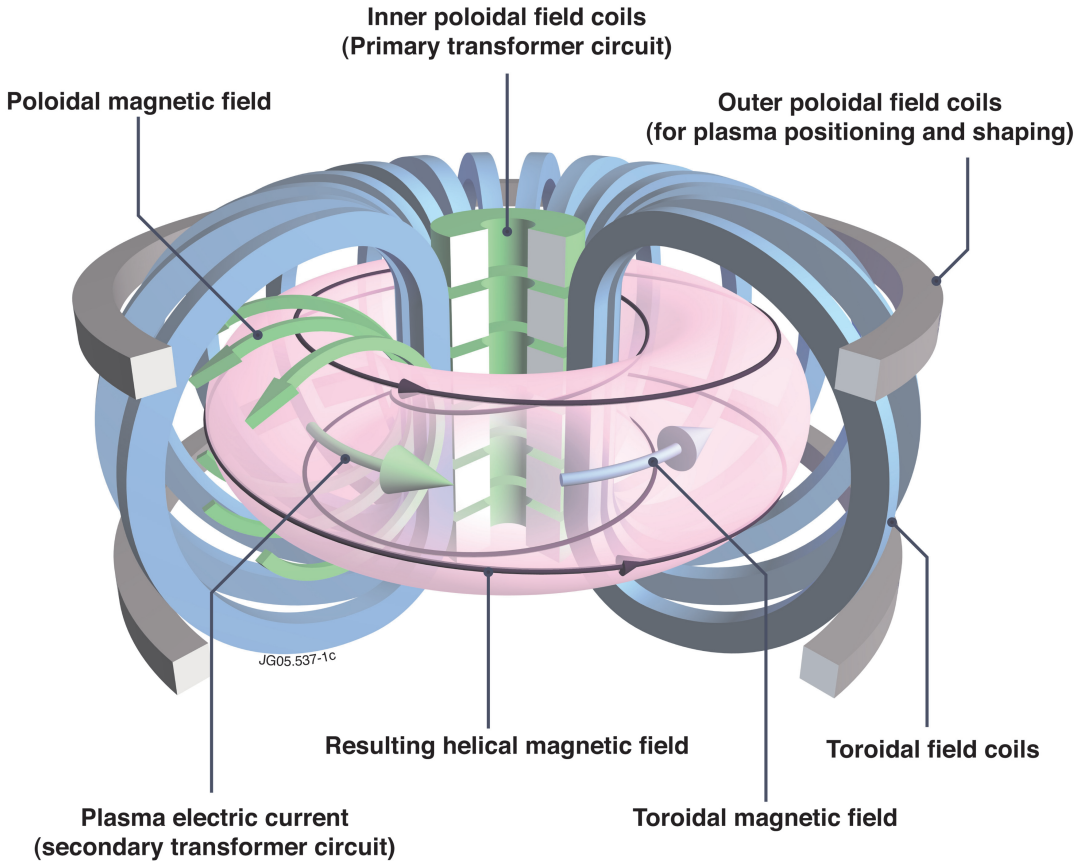

Figure 2.2: Basic setup of a tokamak. Superposition of toroidal magnetic field and poloidal magnetic field leads to helically twisted magnetic field lines. [13]

This charge separation would generate a vertical electric field $\vec{E}$ which leads to an $E \times B$ drift

$$\vec{v}_E = \frac{\vec{E} \times \vec{B}}{B^2} \tag{2.5}$$

that pushes the particles radially outwards towards the wall of the machine. [51] Note that in contrast to the grad-B drift and the curvature drift, the direction of the $E \times B$ drift does not depend on the charge.

To avoid these particle losses arising from a charge separation, magnetic confinement devices add a poloidal magnetic field B_p to the toroidal magnetic field B_t which in total leads to twisted magnetic field lines, as it is shown in figure 2.2 for the example of a tokamak. The resulting magnetic field lines form an infinite set of nested magnetic flux surfaces on which the field lines wind helically around the plasma. [48] Therefore, top and bottom of the plasma are connected by magnetic field lines which prevents charge separation and resulting particle losses.

In a tokamak, the poloidal magnetic field B_p is produced by a plasma current I_p which is induced by a set of transformer coils in the centre of the tokamak (see figure 2.2). The plasma acts as the secondary winding of this transformer.

This approach has one severe disadvantage: As one can see in the Maxwell-Faraday equation

$$\vec{\nabla} \times \vec{E} = -\frac{\partial \vec{B}}{\partial t}, \tag{2.6}$$

conventional tokamaks rely on a monotonically time-varying magnetic field which produces the necessary toroidal electric field that generates the plasma current. Therefore, all present-day tokamaks run in pulsed operation. Advanced tokamak concepts attempt to replace the inductively driven plasma current by means of other external current drive and bootstrap currents to achieve steady-state operation. [6] Nevertheless, the tokamak concept remains the leading solution towards practical fusion energy. Compared to the technically highly complex stellarator concept, tokamaks benefit from better confinement, especially with respect to neo-classical transport. [72]

2.3 Coordinate systems

A commonly used coordinate system for the description of axisymmetric systems is the cylindrical coordinate system (see figure 2.3, left). In this coordinate system, every point is described by the three coordinates (R, φ, z), where the radius R is given by $R := \sqrt{x^2 + y^2}$ and $\varphi \in [0, 2\pi)$ is the toroidal angle rotating counter clockwise in the xy-plane. The system (R, φ, z) is right-handed.

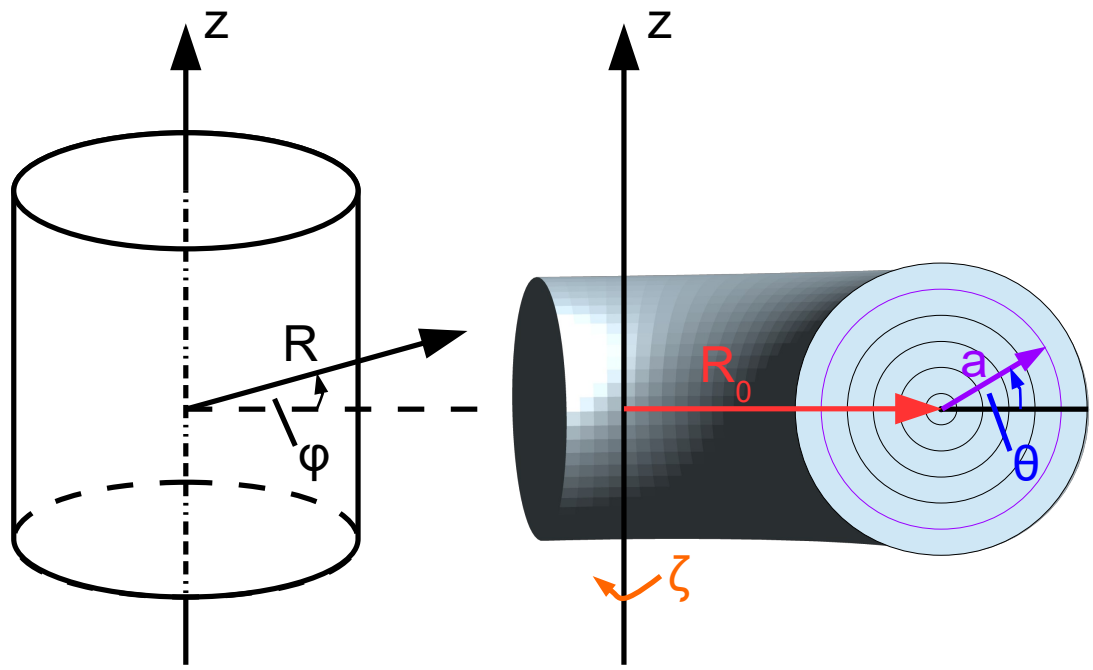

Figure 2.3: Left: Cylindrical coordinate system. Right: Toroidal coordinate system.

Inspired by the torus shape of a tokamak, another coordinate system which is often used is the toroidal coordinate system (see figure 2.3, right). In the toroidal coordinate system, every point is described with the three coordinates (a, θ, ζ) where a is a placeholder for a variable pointing on a specific magnetic surface and θ is the poloidal angle. To adopt the convention of the ASTRA framework [49], the toroidal angle here is chosen to rotate clockwise in the xy-plane ($\zeta = -\varphi$) which makes the system right-handed.

Let us consider a simplified model of a magnetic configuration with concentric circular magnetic flux surfaces, i. e. without Shafranov shift [62] and vertical shift. In this case, the variable a could simply denote the radius of the specified magnetic flux surface. Then, the cylindrical coordinates R, z can be recovered by

$$R = R_0 + a \cdot \cos(\theta), \qquad z = a \cdot \sin(\theta). \tag{2.7}$$

The parameter R_0 which (in our simplified geometry) describes the distance between major axis and magnetic axis is known as the major radius of a tokamak plasma. Furthermore, the radius a of the Last Closed Magnetic Surface (LCMS) is

called minor radius a_0. The ratio R_0/a_0 of these two quantities is called the aspect ratio. Based on the aspect ratio, one distinguishes between conventional tokamaks with a relatively large aspect ratio (example: ASDEX Upgrade with $R_0/a_0 \approx 3.3$ [23]) and spherical tokamaks with a relatively small aspect ratio (example: NSTX with $R_0/a_0 \approx 1.27$ [75]).

2.4 Limiter versus divertor

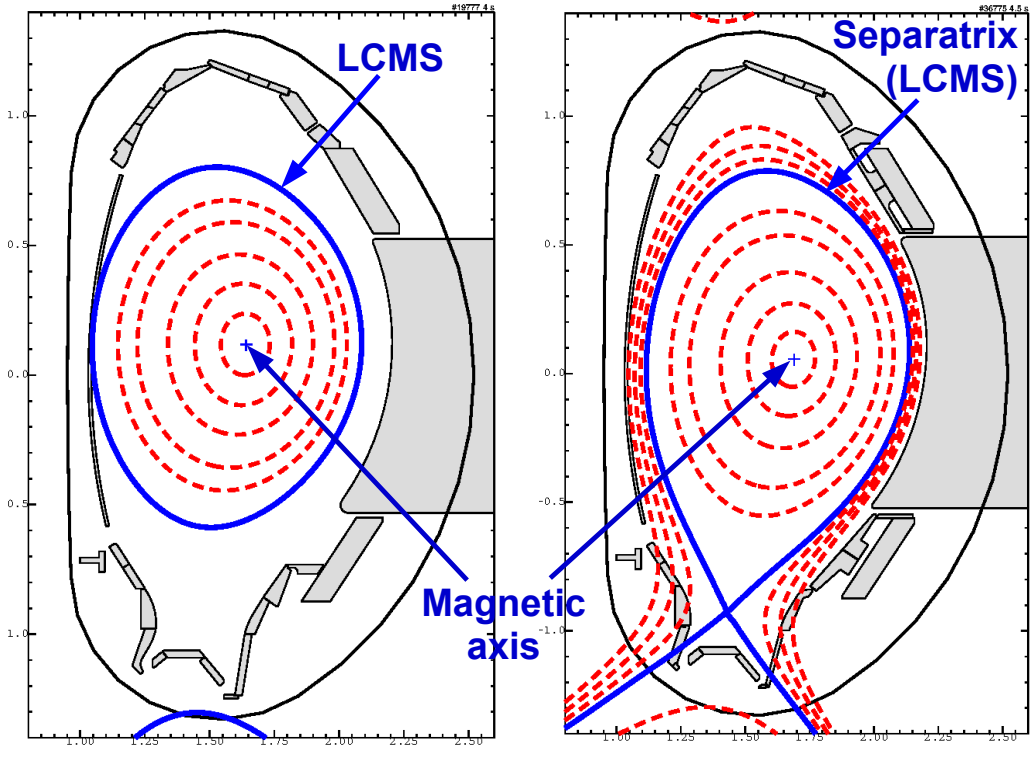

Figure 2.4: Left: Magnetic equilibrium for a plasma in limiter configuration (shot #19777, $t = 4$ s). Right: Magnetic equilibrium for a plasma in divertor configuration (shot #36775, $t = 4.5$ s).

In early experiments, tokamak plasmas were delimited by a limiter as in the example in figure 2.4 (left). In the limiter configuration, the Last Closed Magnetic Surface (LCMS) is determined by a material object that protrudes into the plasma. Such a magnetic configuration protects the walls from damage since outwards travelling

ions hit the limiter instead of arbitrary positions at the wall. However, impurities being released from the limiter can lead to large heat losses.
To reduce heat losses due to impurities, present-day tokamak devices employ a divertor. In divertor configuration, a so-called separatrix separates the confined plasma from regions with open magnetic field lines that have intersections with material surfaces (see figure 2.4, right). This magnetic configuration allows to remove impurities and helium ash from fusion plasmas by directing these particles onto the divertor plates where they are cooled down. In the framework of this thesis, only plasmas in divertor configuration have been examined.

2.5 Non-circular poloidal cross section

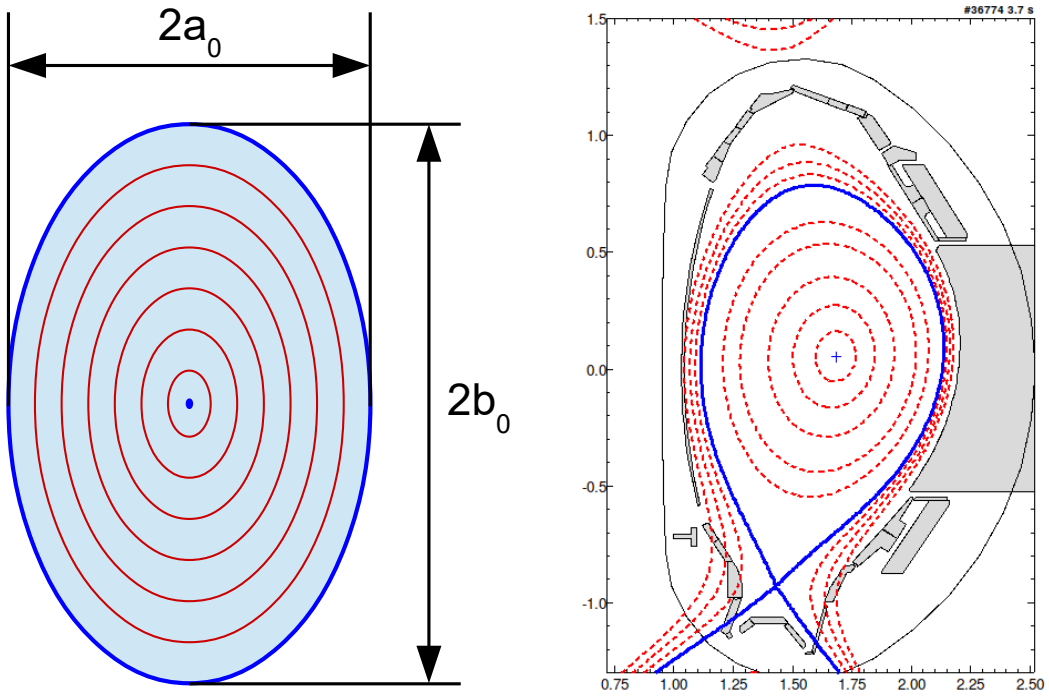

Figure 2.5: Left: Simplified model of an elliptical poloidal cross section. Right: Magnetic equilibrium for a real plasma (shot #36774, $t = 3.7\,\mathrm{s}$) in divertor configuration, created with diaggeom. Separatrix and magnetic axis are coloured in blue, red lines correspond to other magnetic flux surfaces.

In a real plasma, the magnetic equilibrium differs in two aspects from the simplified model in section 2.3: The poloidal cross section is not (necessarily) circular and the magnetic flux surfaces are not concentric since they have a horizontal shift with respect to the magnetic axis (usually called Shafranov shift) and can also have a vertical shift (see figure 2.5, right). In such a geometry, the minor radius a_0 needs to be generalized. If $R_{\max}$ denotes the maximum radius R of a point on the LCMS and $R_{\min}$ denotes the minimum radius R of a point on the LCMS, the minor radius is defined as

$$a_0 := \frac{R_{\max} - R_{\min}}{2}. \tag{2.8}$$

To characterize the shape of a real plasma, there are several parameters. If we define a parameter b_0 analogously to the minor radius as $b_0 := (z_{\max} - z_{\min})/2$ where $z_{\max}$ and $z_{\min}$ are the maximum and the minimum values of z on the LCMS, then the elongation (or ellipticity) of the plasma is defined as

$$\kappa := \frac{b_0}{a_0} = \frac{z_{\max} - z_{\min}}{2a_0}. \tag{2.9}$$

This definition is illustrated on the left in figure 2.5 for the simplified model of elliptical magnetic surfaces. Present-day tokamaks preferably use elongated plasmas ($\kappa > 1$) since it has been shown that for a given plasma current density, higher values of the line-averaged density $\overline{n}_e$ can be achieved before a disruption of the discharge occurs. [22]

If the plasma shape is not symmetric with respect to a horizontal line, one can also define upper and lower elongation. [36] Further parameters to describe the shape of the plasma would be the (upper and lower) triangularity and the squareness of the plasma. Currently, there is also a large interest in studying plasmas with negative triangularity since these could offer favourable Edge Localized Mode (ELM) behaviour and reduced electron heat transport. [77]

Other important physical quantities for labeling magnetic flux surfaces are magnetic fluxes and corresponding derived quantities. The poloidal flux is defined as the integral

$$\Psi := \int_{S_{\mathrm{pol}}} \vec{B} \cdot \mathrm{d}\vec{S} = \int_{S_{\mathrm{pol}}} \vec{B}_{\mathrm{pol}} \cdot \mathrm{d}\vec{S} \tag{2.10}$$

over a ring-shaped surface S_{pol} that stretches from the magnetic axis of the plasma to a specified magnetic flux surface (see figure 2.6, left). The convention for the

poloidal flux is chosen here like in the ASTRA framework [49] such that at the magnetic axis, it is $\Psi = 0$. Alternatively, one can also define a poloidal flux $\widetilde{\Psi}$ by choosing a surface S_{pol} that stretches from the centre at $R = 0$ to the specified magnetic surface (these two definitions are related to each other by the transformation $\Psi = \widetilde{\Psi} - \widetilde{\Psi}_{\mathrm{axis}}$).
The area S_{pol} does not need to be horizontal. As one can see from Gauss's law $\vec{\nabla} \cdot \vec{B} = 0$, any connection between the magnetic axis and the specified flux surface with arbitrary poloidal angle θ leads to the same value for Ψ. [48] Therefore, the poloidal flux Ψ is well-suited to serve as a radial coordinate that labels the magnetic flux surfaces.

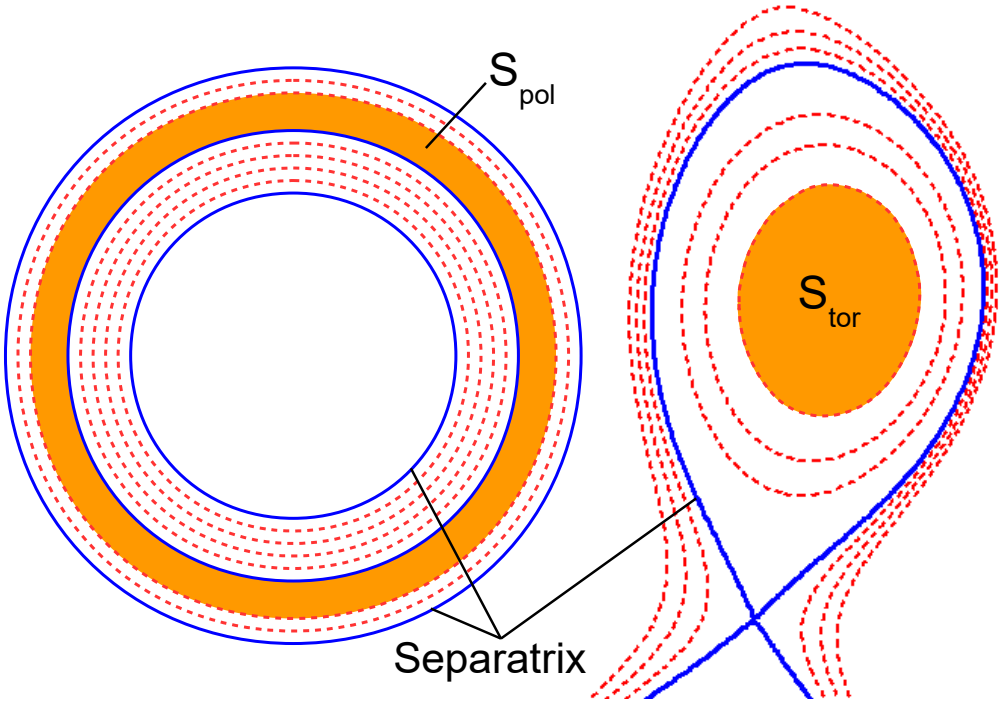

Figure 2.6: Left: Toroidal cross section with integration area S_{pol} for the definition of the poloidal flux. Right: Poloidal cross section with integration area S_{tor} for the definition of the toroidal flux.

Another physical quantity that can be used to label magnetic flux surfaces is the toroidal flux being defined as the integral

$$\Phi := \int_{S_{\mathrm{tor}}} \vec{B} \cdot \mathrm{d}\vec{S} = \int_{S_{\mathrm{tor}}} \vec{B}_{\mathrm{tor}} \cdot \mathrm{d}\vec{S} \tag{2.11}$$

over an area S_{tor} encircled by a specific magnetic flux surface (see figure 2.6, right). From the toroidal flux, one can derive an effective minor radius for the plasma. If B_0 is the magnetic field at $R = R_0$, the toroidal flux radius is defined as

$$\widetilde{\rho} := \sqrt{\frac{\Phi}{\pi B_0}}. \tag{2.12}$$

2.6 Safety factor

Two important quantities describing the helicity of the field lines are the safety factor q and the rotational transform μ. In this section, we will first introduce them in an abstract way and then show their geometrical meaning. The rotational transform is defined as [49]

$$\mu := \frac{\partial \Psi}{\partial \Phi} = \frac{1}{2\pi B_0 \widetilde{\rho}} \cdot \frac{\partial \Psi}{\partial \widetilde{\rho}}. \tag{2.13}$$

In the second equality, we made use of the derivative of the toroidal flux radius (equation (2.12)).
The safety factor is defined as the inverse of the rotational transform:

$$q := \frac{1}{\mu} = \frac{\partial \Phi}{\partial \Psi}. \tag{2.14}$$

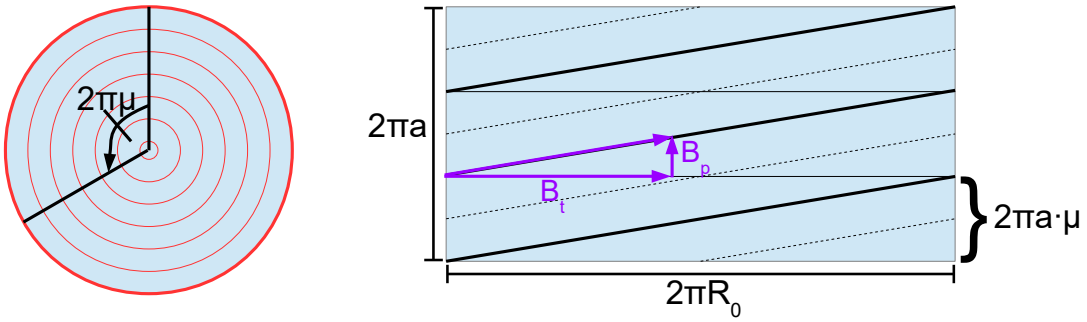

Figure 2.7: Left: Poloidal cross section for the definition of the rotational transform. Right: Unfolded torus. In this example, the safety factor would be $q = 3$.

To visualize the geometrical meaning of these quantities, we will consider again the simplified model of a circular poloidal cross section. In this model, the safety factor

describes the number of toroidal revolutions that a magnetic field line has to make to sweep over an angle of $\Delta\theta = 2\pi$ in poloidal direction:

$$q = \frac{\#\text{toroidal turns}}{\#\text{poloidal turns}}. \tag{2.15}$$

Analogously, the rotational transform μ refers to the poloidal angle θ over which the magnetic field line sweeps while travelling in toroidal direction. During one revolution in toroidal direction, the magnetic field line sweeps over an angle of $2\pi\mu$ in poloidal direction (see figure 2.7, left).
To obtain another expression for the safety factor q, we will consider a flux surface with minor radius a such that $a \ll R_0$. If we unfold the torus of this magnetic flux surface, we obtain a rectangle with length $2\pi R_0$ an height $2\pi a$ (see figure 2.7, right). In this geometry, the ratio between the arc segment $2\pi a/q$ and the length $2\pi R_0$ is equal to the ratio of the poloidal magnetic field B_p and the toroidal magnetic field B_t. This leads to another useful expression for the safety factor in the limit of $R_0/a \gg 1$:

$$q = \frac{a}{R_0} \cdot \frac{B_t}{B_p}. \tag{2.16}$$

In a real tokamak plasma, the safety factor is not radially constant, but mostly increases with increasing minor radius a. Therefore, to describe the helicity of a plasma, one normally refers to the safety factor at a particular radial position. For plasmas in limiter configuration, one usually gives the safety factor at the LCMS $q(a_0)$ and for plasmas in divertor configuration, the safety factor at the 95% flux surface is usually given which is denoted as q_{95}.

3 ITER

ITER is an acronym for International Thermonuclear Experimental Reactor. After construction, ITER will be the world's largest tokamak with a major radius of $R_0 = 6.2\,\mathrm{m}$ and a minor radius of $a_0 = 2.0\,\mathrm{m}$. With its superconducting magnets, ITER will be able to reach toroidal magnetic fields up to $B_t = 5.3\,\mathrm{T}$ and plasma currents up to $I_p = 15\,\mathrm{MA}$. In most scenarios, this will lead to an edge safety factor of $q_{95} = 3.0$.
From the physics side, the ITER project has three major goals which all rely essentially on two factors: The burn duration and the fusion power multiplication factor Q being defined as

$$Q := \frac{P_{\mathrm{fus}}}{P_{\mathrm{aux}}}. \tag{3.1}$$

In this equation, P_{fus} denotes the produced fusion power and P_{aux} denotes the injected heating power from external sources. With this power multiplication factor Q, the mission goals read as follows [43]:

- In inductively driven plasmas, ITER should reach a power multiplication factor of at least $Q = 10$ for burn durations of at least $300\,\mathrm{s}$ such that the plasma is in a stationary state.
- ITER should open up the way towards long-pulse operation by demonstrating burn durations up to $3000\,\mathrm{s}$ in hybrid or fully non-inductive scenarios while maintaining a power multiplication factor of at least $Q = 5$.
- Ignition ($Q = \infty$) is not directly an aim of ITER. However, if controlled ignition proves to be possible, also experiments in this direction should be carried out.

Besides these scientific goals, the ITER project also aims to contribute to technological progress, for example by the development of the necessary superconducting magnets and testing of different Test Blanket Module (TBM) concepts.

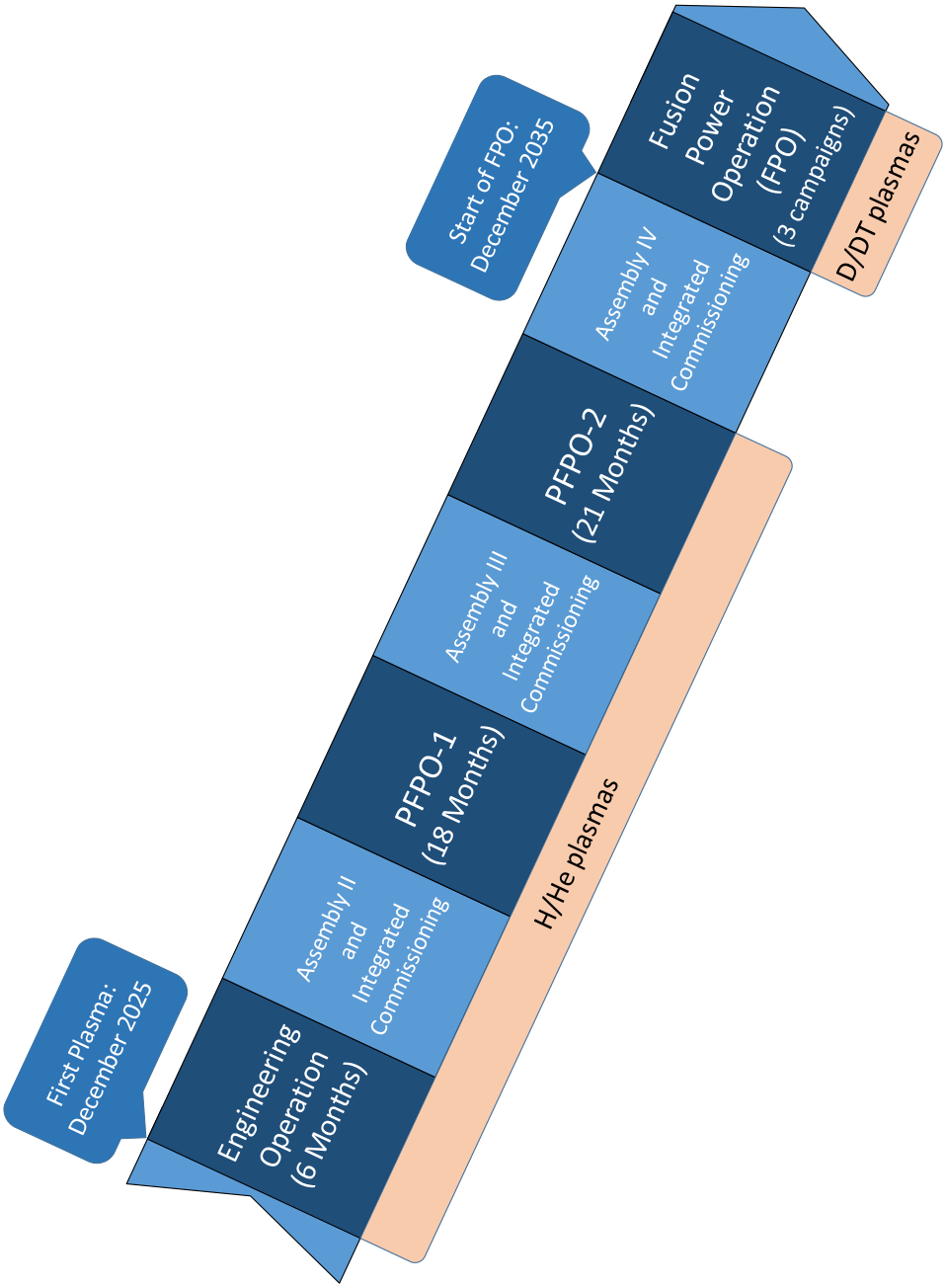

Figure 3.1: The schedule of ITER according to the Staged Approach is divided into four phases of operation and phases of assembly and integrated commissioning.

As one can see in figure 3.1, the current schedule for the project foresees a Staged Approach [43] with four phases of operation which are interleaved by phases of

assembly and integrated commissioning. In the assembly phases, a progressive installation of all tokamak sub-systems will take place whereas in the operational phases, commissioning of these sub-systems with plasma will take place in parallel to experiments studying the plasma behaviour on large-scale tokamaks. The major goals and activities in the operational phases include the following:

- ITER operation is expected to start with the **First Plasma** and the subsequent **Engineering Operation** phase in December 2025. All plasmas in this phase will be in limiter configuration because there will be no divertor yet at this early stage. Auxiliary heating will be provided exclusively from one upper launcher for ECRH heating with $P_{ECRH} = 8\,\mathrm{MW}$.

- The **First Pre-Fusion Power Operation phase (PFPO-1)** is expected to start in December 2028. Apart from commissioning of the Heating and Current Drive (H&CD) system and the diagnostics, a major goal of PFPO-1 will be to demonstrate plasmas with a toroidal magnetic field of at least $B_t = 2.65\,\mathrm{T}$ and a plasma current of at least $I_p = 7.5\,\mathrm{MA}$. After the installation of an all-tungsten divertor in assembly phase II, plasma operation in divertor configuration will be possible in PFPO-1. The H&CD system will consist of at least $20\,\mathrm{MW}$ of ECRH power (plus possible upgrades).

- The **Second Pre-Fusion Power Operation phase (PFPO-2)** is expected to start in June 2032. In this phase, the full H&CD capability ($20\,\mathrm{MW}$ of ICRF heating, $33\,\mathrm{MW}$ of NBI heating and at least $20\,\mathrm{MW}$ of ECRH heating) of at least $73\,\mathrm{MW}$ of heating power will be available. Besides an extensive program of studies of H-mode plasmas, a major goal of PFPO-2 is to demonstrate in L-mode plasmas that operation at full fields (with $I_p = 15\,\mathrm{MA}$ and $B_t = 5.3\,\mathrm{T}$) can be realized. Furthermore, the first variant of the TBMs, namely Electro-Magnetic modules, will be tested in PFPO-2. These will allow the examination of the influence of toroidal field ripples on the plasma performance.

- The **Fusion Power Operation (FPO)** phase, which is expected to start in December 2035, is divided into several campaigns taking place in a 2-year cycle. The first FPO campaign will start with a short period of deuterium experiments that aims for commissioning the H&CD system and new measurement systems with deuterium and to develop H-mode scenarios in D. Then, a gradual transition to DT plasmas is planned in 2036. The aim of the first FPO cam-

paign is to demonstrate the production of a few hundred MW of fusion power. The second and third FPO campaigns will then focus first on achieving the $Q \geq 10$ mission goal in inductively driven plasmas and then on the long-pulse mission goal at around $Q \approx 5$ in hybrid or fully non-inductive scenarios.

3.1 Pre-Fusion Power Operation - 1

This master thesis focuses mainly (though not exclusively) on the first Pre-Fusion Power Operation phase of ITER. According to the risk register of the ITER Research Plan [43], a major risk in PFPO-1 is the high uncertainty over the H-mode power threshold, especially in hydrogen plasmas. However, to achieve H-mode plasmas already in PFPO-1 would be highly desirable since this would allow early studies of ELM control. Furthermore, it would allow the comparison of PFPO-1 H-mode plasmas with PFPO-2 H-mode plasmas. Since plasmas in PFPO-2 are affected by toroidal field ripples produced by the TBMs, this would allow assessment of the influence of 3-D fields on H-mode performance.
For a surface of $S = 683\,\mathrm{m}^2$, a magnetic field of $B_t = 2.65\,\mathrm{T}$ and a density of $\overline{n_e} = 0.4 \cdot n_{\mathrm{GW}}$, the Martin 2008 scaling [39] predicts a threshold heating power for the L-H transition of $37\,\mathrm{MW}$ for H plasmas. Therefore, with only $20\,\mathrm{MW}$ of ECRH power in PFPO-1, H-mode operation seems to be inaccessible in hydrogen plasmas at half field ($B_t = 2.65\,\mathrm{T}$ and $I_p = 7.5\,\mathrm{MA}$). A very important scenario in PFPO-1 will therefore be the operation at only one third field ($B_t = 1.8\,\mathrm{T}$ and $I_p = 5\,\mathrm{MA}$) since this allows access to H-mode at lower injected heating powers.
Furthermore, two possible upgrades of the H&CD system in PFPO-1 are currently under investigation. One possible upgrade would be the early installation of one IRCF antenna such that in PFPO-1, already $10\,\mathrm{MW}$ of ICRF heating power would be available [43]. Another possible upgrade would lead to additional $10\,\mathrm{MW}$ of ECRH heating power [76]. Both upgrades would result in a total heating power of $30\,\mathrm{MW}$ in PFPO-1.
According to the baseline strategy of the ITER Research Plan, the full ECRH power would be provided by 24 single-frequency gyrotrons running at a frequency of $170\,\mathrm{GHz}$. For operation at one third field ($B_t = 1.8\,\mathrm{T}$), this would correspond to third harmonic (X3) absorption of EC radiation for which the efficiency is highly dependent on the density and on the central electron temperature of the plasma as

one can see in figure 3.2. However, JINTRAC simulations could show that no X2 preheating is required [76]. Due to a positive feedback loop (higher central electron temperature leads to higher absorption and vice versa), absorption efficiencies of at least 90% could be reached in all simulations with $P_{ECRH} \geq 10\,\mathrm{MW}$.
Although being a very encouraging result, it is also a highly questionable result. Central electron temperatures do not only depend on the source of electron energy determined by the EC absorption, but also on (turbulent) transport in the core of the plasma. Results presented in [76] were obtained by applying the Bohm-gyroBohm transport model. In the framework of this thesis, the applicability of the quasi-linear transport models TGLF and QuaLiKiz to predict central electron temperatures has been tested. This will allow more detailed studies on the necessity of X2 preheating in the future.

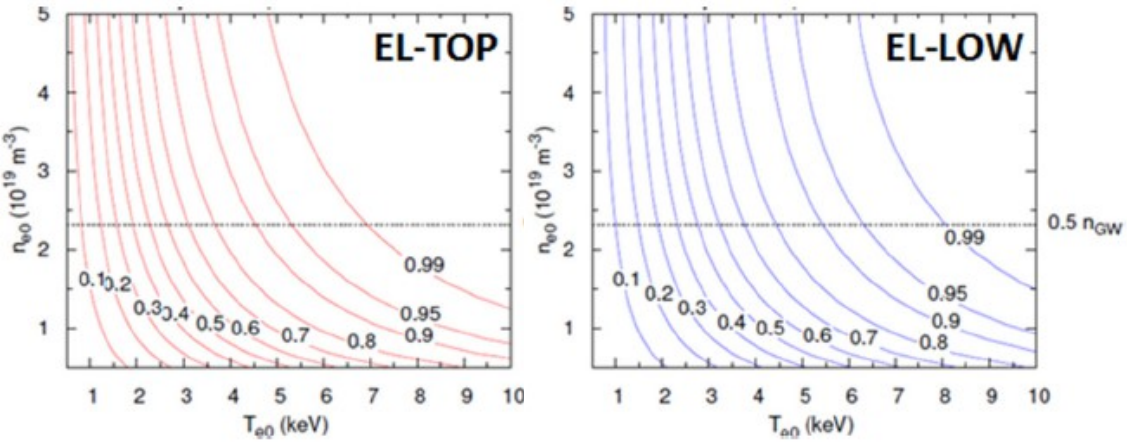

Figure 3.2: EC absorption efficiency for different mirrors of the Equatorial Launcher for $170\,\mathrm{GHz}$ gyrotrons. [76]

At one third field ($B_t = 1.8\,\mathrm{T}$), also the range of the prefill pressure that allows Ohmic plasma start-up is predicted to be very narrow [43]. If it turns out that Ohmic plasma initiation is not possible at $B_t = 1.8\,\mathrm{T}$, plasma start-up would require ECRH-assistance. However, due to the comparably low absorption efficiency especially at low densities and low central electron temperatures (see figure 3.2), ECRH-assisted start-up is not possible with 3^{rd} harmonic absorption. Therefore, the ITER Research Plan considers two further options for the ECRH system which are currently under investigation:

- At least 16 single-frequency gyrotrons at $170\,\mathrm{GHz}$ and up to 8 single-frequency gyrotrons at $110\,\mathrm{GHz}$
- At least 16 single-frequency gyrotrons at $170\,\mathrm{GHz}$ and up to 8 gyrotrons with dual-frequency operation ($104\,\mathrm{GHz}$ and $170\,\mathrm{GHz}$)

In both options, the fraction of the ECRH system which is operating at lower frequency would provide the necessary second harmonic (X2) heating.

4 ASTRA

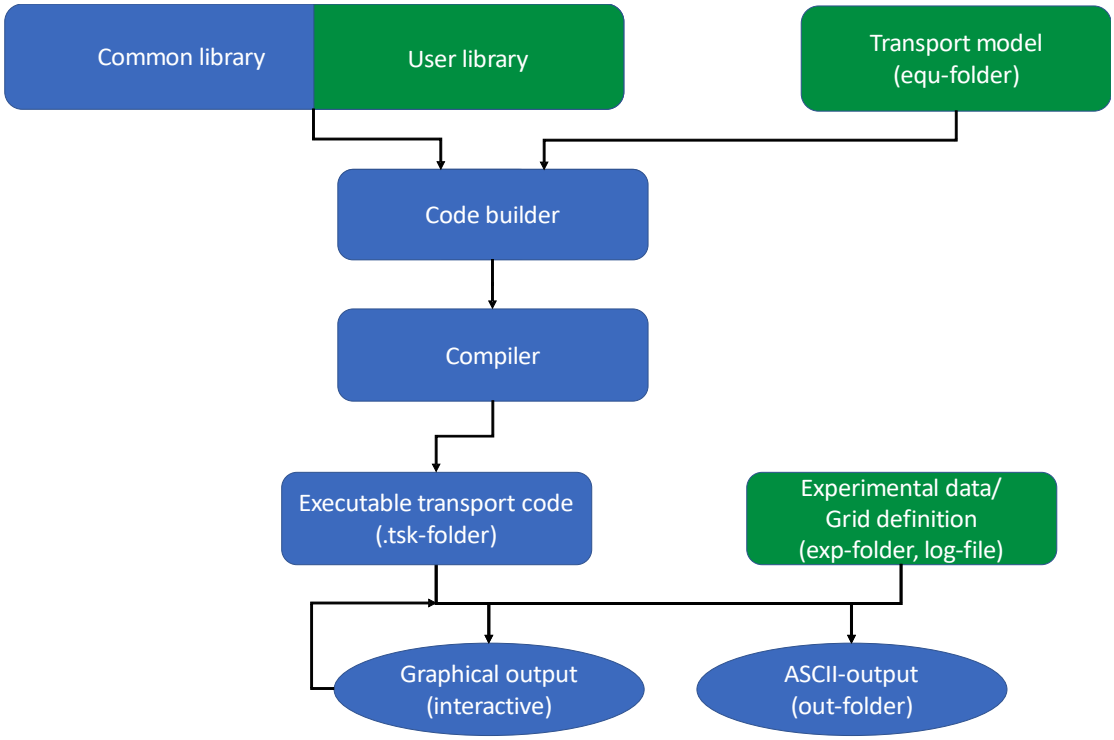

Figure 4.1: Workflow diagram for transport simulations with ASTRA. The green components require data or code provided by the user whereas the blue parts are performed by the ASTRA system itself. Graphical output is only provided in interactive mode.

ASTRA, the **A**utomated **S**ystem for **TR**ansport **A**nalysis, is an integrated modeling suite for transport simulations [49]. It is the successor of the TRANSITOR code [50]. The basic structure of ASTRA and its use during this master thesis is depicted in figure 4.1.

Performing transport simulations with ASTRA requires only two user activities (coloured in green in figure 4.1): First, the user has to set up a transport model and

provide the necessary plug-in modules and expressions to his user library if they are not part of the standard distribution of ASTRA. Secondly, for execution of the transport model on a specific case, the user has to provide the necessary data for machine and plasma parameters and to define the time evolution and the grid of the simulation.
The transport model has to be formulated in the ASTRA modeling language. This is a high-level language that allows one to take into account a physical process by simply calling the respective subroutine. Such plug-in modules could for example represent sawtooth instabilities or the heating and current drive system. Furthermore, the ASTRA language allows one to refer to a physical quantity by means of a single expression (a function in the folder `fnc` or a formula in the folder `fml`). An example for such an expression would be `POH` which describes the power density of Ohmic heating P_{Ohm}.
The standard distribution of ASTRA already provides a large set of standard expressions and plug-in modules which can be accessed via symbolic links. Apart from these modules and expressions in the common library, the user can also create his own expressions and subroutines.
After the transport model is specified and all additional modules are written by the user, the ASTRA interpreter will generate the corresponding source code (in Fortran and C) and compile this source code to create an executable. The user will then be able to run his transport model with different experimental data sets provided in the `exp`-folder and different grid sizes and time step definitions.
Throughout this master thesis, the most recent version of ASTRA, version 7 [17], has been applied. In this new version, the grid has been changed such that the grid is now based on the normalized toroidal flux radius being defined as

$$\rho := \frac{\widetilde{\rho}}{\widetilde{\rho}_B} = \sqrt{\frac{\Phi}{\Phi_B}}. \tag{4.1}$$

In this equation, $\widetilde{\rho}_B$ and Φ_B denote the effective minor radius and the toroidal magnetic flux at the boundary of the plasma, respectively. Further new features of version 7 are the inclusion of a toroidal momentum transport equation and the coupling to the free-boundary equilibrium solver SPIDER [29, 74] which has also been used in the framework of this master thesis.

4.1 Transport equations

The heart of ASTRA is a set of 1D transport equations that describe the evolution of different physical quantities in time. [49] The three most important transport equations give the time evolution of the electron density n_e, the electron temperature T_e and the ion temperature T_i (as usual in plasma physics, T_e and T_i are given in units of energy):

$$\begin{cases} \frac{1}{V'}\left(\frac{\partial}{\partial t} - \frac{\dot{B}_0}{2B_0}\frac{\partial}{\partial\widetilde{\rho}}\widetilde{\rho}\right)(V'n_e) + \frac{1}{V'}\frac{\partial\Gamma_e}{\partial\widetilde{\rho}} = S_e \\ \frac{3}{2}(V')^{-5/3}\left(\frac{\partial}{\partial t} - \frac{\dot{B}_0}{2B_0}\frac{\partial}{\partial\widetilde{\rho}}\widetilde{\rho}\right)\left((V')^{5/3}n_iT_i\right) + \frac{1}{V'}\frac{\partial}{\partial\widetilde{\rho}}\left(Q_i + \frac{5}{2}T_i\Gamma_i\right) = P_i \\ \frac{3}{2}(V')^{-5/3}\left(\frac{\partial}{\partial t} - \frac{\dot{B}_0}{2B_0}\frac{\partial}{\partial\widetilde{\rho}}\widetilde{\rho}\right)\left((V')^{5/3}n_eT_e\right) + \frac{1}{V'}\frac{\partial}{\partial\widetilde{\rho}}\left(Q_e + \frac{5}{2}T_e\Gamma_e\right) = P_e \end{cases} \tag{4.2}$$

In these equations, $V' := \partial V/\partial\widetilde{\rho}$ denotes the derivative of the volume with respect to the effective minor radius and n_i denotes the density of the main ions.
The structure of these three equations is similar and resembles that of a continuity equation. The term including the time derivative of the toroidal magnetic field $\dot{B}_0$ takes into account changes in n_e, T_i and T_e due to adiabatic compression of the plasma. The source terms S_e, P_i and P_e on the right-hand side denote the electron particle source, the source of ion energy and the source of electron energy, respectively. Finally, in every equation, there is a term representing the divergence of a flux. In the system of transport equations (equation (4.2)), one finds the particle flux for electrons Γ_e, the particle flux for the main ions Γ_i, the electron heat flux Q_e and the ion heat flux Q_i.
To obtain a fourth transport equation for the poloidal flux Ψ, we will consider the electric field $\vec{E}$ which is induced by the transformer coils. Integrating Ampère's law over a circular surface A centered around the major axis ($R = 0$) which is fixed in space

$$\oint_{\partial A}\vec{E}\cdot\mathrm{d}\vec{l} = -\frac{\partial}{\partial t}\int_A\vec{B}\cdot\mathrm{d}\vec{A} \tag{4.3}$$

leads to the following expression for the electric field:

$$\vec{E} = \frac{1}{2\pi} \left.\frac{\partial \Psi}{\partial t}\right|_{\vec{r}} \vec{\nabla}\zeta. \tag{4.4}$$

From this, one obtains the parallel electric field $E_\parallel$ as a projection of $\vec{E}$ on the $\vec{B}$-field. Analogously, one also defines the parallel current density $j_\parallel$, the bootstrap current density j_{BS} and the current density j_{CD} from external current drive:

$$E_\parallel := \frac{\langle \vec{E} \cdot \vec{B} \rangle}{B_0}, \quad j_\parallel := \frac{\langle \vec{j} \cdot \vec{B} \rangle}{B_0}, \qquad j_{\mathrm{BS}} := \frac{\langle \vec{j}_{\mathrm{BS}} \cdot \vec{B} \rangle}{B_0}, \quad j_{\mathrm{CD}} := \frac{\langle \vec{j}_{\mathrm{CD}} \cdot \vec{B} \rangle}{B_0}. \tag{4.5}$$

In these definitions, the flux surface average $\langle \cdot \rangle$ has been applied.
Re-writing the longitudinal Ohm law [49]

$$j_\parallel = \sigma_\parallel E_\parallel + j_{\mathrm{BS}} + j_{\mathrm{CD}} \tag{4.6}$$

in which $\sigma_\parallel$ denotes the conductivity parallel to the $\vec{B}$-field, by using the electric field of equation (4.4) and the definition of $E_\parallel$ in equation (4.5) leads to a transport equation for the evolution of the poloidal flux Ψ:

$$\sigma_\parallel \left(\frac{\partial}{\partial t} - \frac{\widetilde{\rho}\dot{B}_0}{2B_0} \frac{\partial}{\partial \widetilde{\rho}} \right) \Psi = \frac{V'}{2\pi\widetilde{\rho}} j_\parallel - \frac{V'}{2\pi\widetilde{\rho}} (j_{\mathrm{BS}} + j_{\mathrm{CD}}). \tag{4.7}$$

The current density of external current drive j_{CD} has to be supplied by separate modules or by experimental data. The bootstrap current j_{BS} is determined together with the particle flux Γ_e and the heat fluxes Q_e and Q_i within the ASTRA framework using the transport matrix:

$$\begin{pmatrix} \dfrac{\Gamma_e}{n_e} \\ \dfrac{Q_e}{n_e T_e} \\ \dfrac{Q_i}{n_i T_i} \\ V' G_1 \dfrac{\mu_0 j_{\mathrm{BS}}}{B_p} \end{pmatrix} = -V' G_1 \begin{pmatrix} D_n & D_e & D_i & C_n \\ \chi_n^e & \chi_e & \chi_i^e & C_e \\ \chi_n^i & \chi_e^i & \chi_i & C_i \\ H_n & H_e & H_i & 0 \end{pmatrix} \cdot \begin{pmatrix} \dfrac{1}{n_e} \dfrac{\partial n_e}{\partial \widetilde{\rho}} \\ \dfrac{1}{T_e} \dfrac{\partial T_e}{\partial \widetilde{\rho}} \\ \dfrac{1}{T_i} \dfrac{\partial T_i}{\partial \widetilde{\rho}} \\ -1 \end{pmatrix}. \tag{4.8}$$

The factor G_1 in this equation is defined by

$$G_1 := \langle(\vec{\nabla}\widetilde{\rho})^2\rangle. \tag{4.9}$$

The coefficients in the transport matrix have to be specified by the user in the model file. The three coefficients C_n, C_e and C_i in the right column have the dimension of $\mathrm{m/s}$, the three coefficients H_n, H_e and H_i are dimensionless. All other diffusivities have the dimension of $\mathrm{m^2/s}$. During this master thesis, most off-diagonal elements were set equal to zero ($D_e = D_i = \chi_n^e = \chi_i^e = \chi_n^i = \chi_e^i = 0$) and effective diagonal heat conductivities were used.
In addition to the four transport equations presented in equations (4.2) and (4.7), version 7 of ASTRA also includes one equation describing the time evolution of the toroidal angular momentum density M_ϕ. [17]
Sometimes, one is interested in the time evolution of further physical quantities such as impurity densities. For such cases, the ASTRA framework provides multiple additional transport equations for unspecified physical quantities f_j ($j \in \{1, ..., 6\}$) of the form

$$\frac{\partial}{\partial t}(V' f_j) = -\frac{\partial}{\partial \widetilde{\rho}}\left[V' G_1 \left(v_j f_j - D_j \frac{\partial f_j}{\partial \widetilde{\rho}}\right)\right] + V' S_j \qquad (j \in \{1, ..., 6\}). \tag{4.10}$$

Also these equations have the structure of a continuity equation with an additional source term S_j. The parameters v_j in these equations describe the convection of the quantity f_j whereas the parameters D_j are the coefficients of a diffusion-like process.

4.2 Ohmic heating

Ohmic heating (or Joule heating) is a contribution to the source of electron energy P_e that is present in every tokamak plasma. However, in a plasma, the resistivity (and therefore also the current density $\vec{j}$) is not uniform, but depends on the position $\vec{r}$ in the plasma. Therefore, a differential form of the Joule law has to be applied. The Ohmic heating power per volume element is given by

$$P_{\mathrm{Ohm}} = \vec{j} \cdot \vec{E}. \tag{4.11}$$

If we consider a hypothetical plasma in the absence of a magnetic field ($\vec{B} = 0$), the resistivity η is defined by the equation $\vec{E} = \eta\vec{j}$. [54] If we insert this into equation (4.11), we obtain

$$P_{\mathrm{Ohm}} = \eta\vec{j} \cdot \vec{j} = \eta \cdot j^2$$

which reminds of the well-known equation $P = R \cdot I^2$ that describes the Joule heating power in a wire with resistance R.
In general, one can re-write equation (4.11) for the Ohmic heating power density by inserting the electric field $\vec{E}$ from equation (4.4). This leads to

$$P_{\mathrm{Ohm}} = \frac{1}{2\pi}\vec{j} \cdot \left.\frac{\partial\Psi}{\partial t}\right|_{\vec{r}} \vec{\nabla}\zeta. \tag{4.12}$$

In the ASTRA standard distribution, the Ohmic heating power density P_{Ohm} is encoded in the two expressions `POH` and `PJOUL` (with two different approximations).

4.3 Electron-ion energy transfer

The collisional electron-ion heat exchange P_{ei} is another term contributing to the sources of electron energy P_e and ion energy P_i in every tokamak plasma. It contributes to P_e and P_i with the same magnitude, but with opposite sign. In a plasma with only one species of ions with mass m_i (or ion mass number A_i), the electron-ion energy transfer due to Coulomb collisions is given by [49]

$$P_{ei} = \frac{3m_e}{m_i} \cdot \frac{n_e}{\tau_{ei}}(T_e - T_i) \propto \frac{1}{A_i} \cdot \frac{n_e}{\tau_{ei}}(T_e - T_i). \tag{4.13}$$

Here, m_e is the electron mass. The characteristic time τ_{ei} of energy exchange through collisions [25] obeys the following dependencies:

$$\tau_{ei} \propto \frac{T_e^{3/2}}{n_i Z_i^2 \ln(\Lambda)}. \tag{4.14}$$

In this equation, Z_i denotes the charge number of the ions and $\lambda := \ln(\Lambda)$ is the Coulomb logarithm. Inserting τ_{ei} into equation (4.13) leads to the following expres-

sion for the electron-ion energy exchange:

$$P_{ei} \propto \frac{Z_i^2}{A_i} n_i n_e \lambda \frac{T_e - T_i}{T_e^{3/2}}. \tag{4.15}$$

This is implemented in the ASTRA expression `PEICL`.

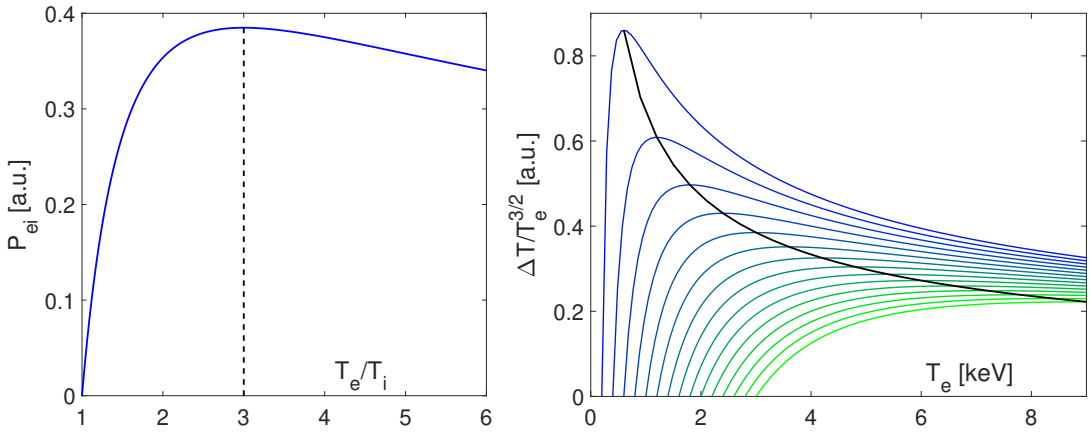

Figure 4.2: Left: The maximum of P_{ei} is found for $T_e = 3 \cdot T_i$. Note that P_{ei} is given in arbitrary units (a.u.). Right: The maximum P_{ei} decreases as $1/\sqrt{T_i}$.

A real tokamak plasma never consists of only one ion species since there are always some impurity ion species present in the plasma. Such plasmas require a more complete treatment in which the total electron-ion heat transfer P_{ei} is determined by the sum over all individual components j with ion density $n_{i,j}$. Under the assumption, that all components have the same ion temperature T_i, this leads to the following expression:

$$P_{ei} \propto \lambda \frac{T_e - T_i}{T_e^{3/2}} n_e \cdot \sum_j \frac{n_{i,j} Z_j^2}{A_j}. \tag{4.16}$$

This is implemented in the ASTRA expression `PEICL2`.

To understand the temperature dependence of P_{ei}, we will now consider the term $(T_e - T_i)/T_e^{3/2}$. One should note that also the Coulomb logarithm depends on the temperature ($\lambda = \lambda(T_e)$). However, to a good approximation, it is sufficient to consider only $(T_e - T_i)/T_e^{3/2}$ which is positive for $T_e > T_i$. As we can see in figure 4.2, this term has a non-monotonic dependence on the electron temperature. If we consider an arbitrary, but fixed ion temperature T_i, there is a maximum for P_{ei} at $T_e = 3 \cdot T_i$ (see figure 4.2, left). The height of this maximum depends on the considered T_i and decreases as $1/\sqrt{T_i}$ (see figure 4.2, right).

5 Turbulence

In tokamak plasmas, various processes contribute to transport, including classical collisional transport, neoclassical transport and transport via macro-instabilities and micro-instabilities. Since experimentally observed energy confinement times are much smaller than predicted by (neo-)classical theory (electron heat transport about 100 times larger in experiment), it is nowadays widely accepted that the dominant underlying process of transport is turbulence, i.e. transport via micro-instabilities. [34, 4]

5.1 Gyrokinetic model

Microinstabilities can be explained with kinetic theory which describes the time evolution of a distribution function $F = F(t, \vec{x}, \vec{v})$ in phase-space through the kinetic equation (or Boltzmann equation) [54, 4]

$$\frac{\mathrm{d}F}{\mathrm{d}t} = \frac{\partial F}{\partial t} + \frac{\mathrm{d}\vec{x}}{\mathrm{d}t} \cdot \frac{\partial F}{\partial \vec{x}} + \frac{\mathrm{d}\vec{v}}{\mathrm{d}t} \cdot \frac{\partial F}{\partial \vec{v}} = C(F). \tag{5.1}$$

The term $C(F)$ on the right is the collision operator which describes the change of the phase-space density F due to internal forces. A major property of the kinetic equation is that along a trajectory, changes of the phase-space density result exclusively from collisions since $\mathrm{d}F/\mathrm{d}t = C(F)$.
There are different possibilities to normalize F. [54] Here, we will normalize the distribution function such that the integral over velocity space gives the density n and the integral over full phase-space gives the total particle number N:

$$\int F \mathrm{d}^3x \, \mathrm{d}^3v = N. \tag{5.2}$$

Plasma turbulence appears on spatial scales being comparable to the ion Larmor radius ρ_i and the electron Larmor radius ρ_e, but on time scales being much slower than the cyclotron frequencies Ω. Therefore, in the description of microinstabilities, one can neglect the gyromotion and take the gyroaverage over the kinetic equation (5.1). Considering only the deviation $f := F - F_{\mathrm{M}}$ of the phase-space density F from an equilibrium (=Maxwell) background density F_{M}, [45] this leads then to the δf gyrokinetic equation describing the evolution of the distribution of gyro-centers:

$$\frac{\partial f}{\partial t} + \vec{v}_{gc} \cdot \vec{\nabla} f + \vec{v}_E \cdot \vec{\nabla} f - \frac{\mu}{m} \vec{\nabla}_{\parallel} B \cdot \frac{\partial f}{\partial \vec{v}_{\parallel}} = C(f) - \vec{v}_E \cdot \vec{\nabla} F_M - \frac{Ze}{T} F_M \vec{v}_{gc} \cdot \vec{\nabla} \Phi. \quad (5.3)$$

In this equation, μ denotes the magnetic moment, m the mass, Φ the (fluctuating) electric potential and $\vec{v}_E$ the $E \times B$ drift velocity arising from the fluctuating electric field $\vec{E} = -\vec{\nabla}\Phi$. The velocity $\vec{v}_{gc}$ contains all other contributions to the motion of the gyro-center, i.e. the motion parallel to the B-field (with unit vector $\vec{b}$), the grad-B drift and the curvature drift:

$$\vec{v}_{gc} := v_{\parallel} \vec{b} + \vec{v}_{\nabla B} + \vec{v}_{\mathrm{curv}}.$$

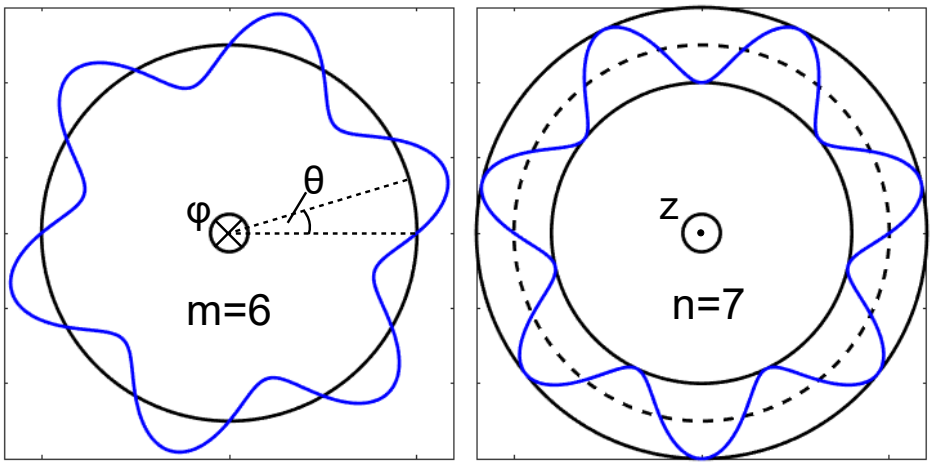

Figure 5.1: Definition of the poloidal mode number in a poloidal cross section (left) and the toroidal mode number in a toroidal cross section (right).

Considering a simplified magnetic geometry with a purely toroidal magnetic field $\vec{B} = B_0 \frac{R_0}{R} \vec{b}$ will make the mirror force term (fourth term in equation (5.3)) disap-

pear. [46] Since collisions have only small effect on the considered electrostatic instabilities, a further approximation can be made by considering only collisionless plasmas ($C(f) = 0$). Neglecting the term $\vec{v}_E \cdot \vec{\nabla} f$, which is a product of two perturbations, will remove any non-linearity from the gyrokinetic equation and decouple the toroidal modes. This results in the linearized gyrokinetic equation for collisionless plasmas:

$$\frac{\partial f}{\partial t} + \vec{v}_{gc} \cdot \vec{\nabla} f = -\vec{v}_E \cdot \vec{\nabla} F_M - \frac{Ze}{T} F_M \vec{v}_{gc} \cdot \vec{\nabla} \Phi. \tag{5.4}$$

The spectra of growth rates γ and real frequencies ω_r of microinstabilities in a plasma are determined in Fourier space. In Fourier space, the instabilities can be considered as a superposition of many harmonic fluctuations with different poloidal mode numbers m and toroidal mode numbers n. If we consider an arbitrary wave in a poloidal cross section with poloidal mode number m (see example in figure 5.1, left), the wave number k_θ perpendicular to the magnetic field lines is given by

$$k_\theta = \frac{m}{r} \tag{5.5}$$

when r is the radius of the considered flux surface. Analogously, one can define a wavenumber $k_\parallel$ parallel to the magnetic field lines.
Fourier-transforming the linear gyrokinetic equation (5.4) with respect to the time coordinate t and the space coordinate $\vec{x}$, one obtains

$$\begin{aligned} \hat{\omega} f + \frac{m}{ZT}\left(v_\parallel^2 + \frac{v_\perp^2}{2}\right) f - \frac{v_\parallel k_\parallel}{\omega_D} f = ... \\ \frac{e}{T}\left[\frac{R}{L_n} + \left(\frac{m v_\parallel^2 + m v_\perp^2}{2T} - \frac{3}{2}\right)\frac{R}{L_T} - \frac{m}{T}\left(v_\parallel^2 + \frac{v_\perp^2}{2}\right) + Z\frac{v_\parallel k_\parallel}{\omega_D}\right] F_M \Phi. \end{aligned} \tag{5.6}$$

In this equation, the frequency $\hat{\omega} = \omega/\omega_D$ was normalized with the drift frequency

$$\omega_D := -\frac{k_\theta T}{eBR}. \tag{5.7}$$

The quantities R/L_n and R/L_T are the normalized logarithmic gradients of density and temperature, respectively. These are defined by

$$\frac{R}{L_n} := -\frac{R}{n}\frac{\mathrm{d}n}{\mathrm{d}r}, \qquad \frac{R}{L_T} := -\frac{R}{T}\frac{\mathrm{d}T}{\mathrm{d}r}. \tag{5.8}$$

5.2 Ion Temperature Gradient (ITG) instability

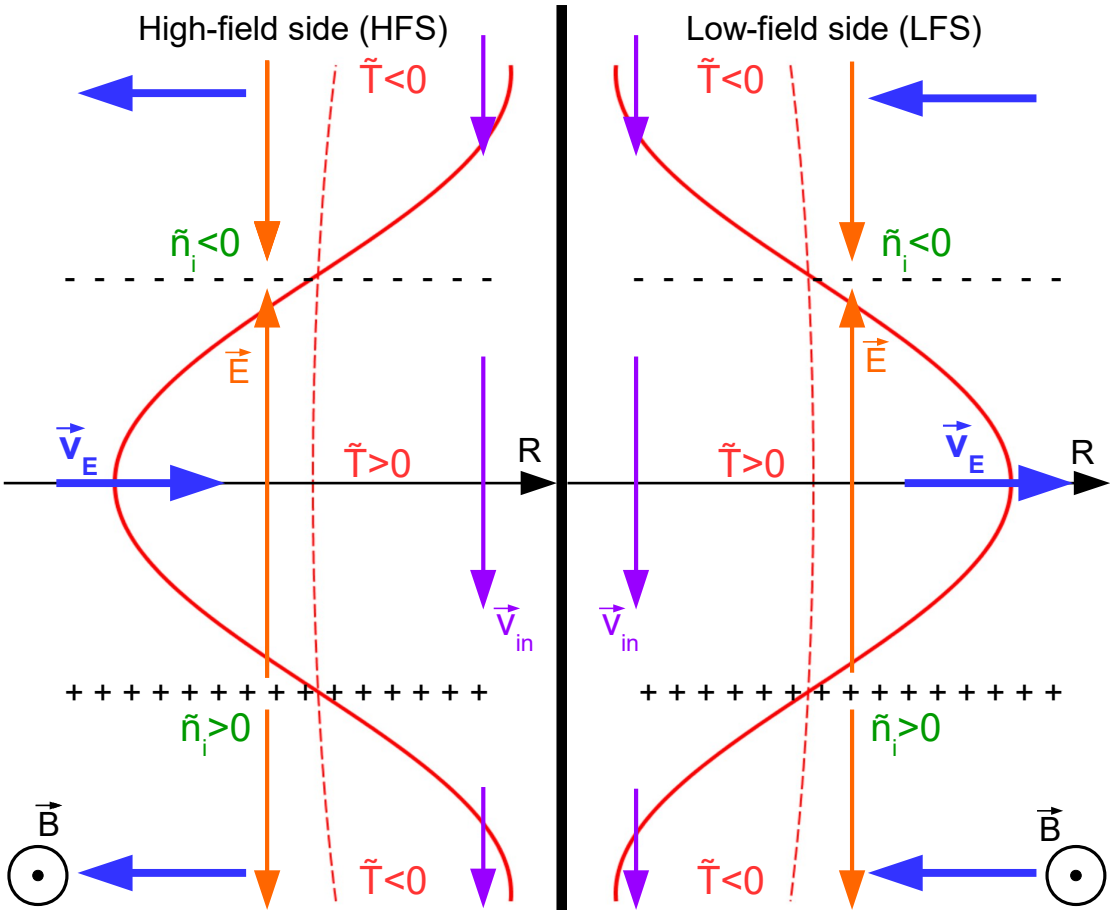

Figure 5.2: The dashed red line represents an equilibrium isothermal flux surface. The solid red line represents an actual isothermal line which is perturbed against the equilibrium. Left: On the HFS, the resulting $E \times B$-drift works against the perturbation and stabilizes the plasma. Right: On the LFS, the resulting $E \times B$-drift amplifies the perturbation which leads to an ITG instability.

During this master thesis, the focus was on electrostatic instabilities (caveat: in fact, the field is dynamic) which are characterized by a fluctuating electric field $\vec{E}$ which leads to an $E \times B$-drift resulting in radial transport. Two very similar electrostatic micro-instabilities are the Electron Temperature Gradient (ETG) mode and the Ion Temperature Gradient (ITG) mode. Since ETG modes follow the same principles as ITG modes, but with the roles of electrons and ions exchanged, we will only

consider the example of ITG modes here. The major differences between these two instabilities are that ETG modes appear on the electron Larmor radius scale whereas ITG modes appear on the ion Larmor radius scale and that the real frequencies ω_r have different signs.
For the description of the ITG instability, we will define a drift $\vec{v}_{\mathrm{in}}$ resulting from the inhomogeneity of the magnetic field in toroidal geometry:

$$\vec{v}_{\mathrm{in}} := \vec{v}_{\nabla B} + \vec{v}_{\mathrm{curv}}. \tag{5.9}$$

Since in a tokamak, both, the grad-B drift $\vec{v}_{\nabla B}$ and the curvature drift $\vec{v}_{\mathrm{curv}}$, always point in the same direction, this will simplify the description. [51]
An ITG instability occurs if on the LFS of the tokamak, there is an initial perturbation $\widetilde{T}$ of the ion temperature with respect to the equilibrium. Such a situation is depicted on the right-hand side of figure 5.2. Since the magnitude of both, the grad-B drift and the curvature drift are dependent on the particles' velocities,

$$|\vec{v}_{\nabla B}| \propto \frac{v_\perp^2}{2}, \qquad |\vec{v}_{\mathrm{curv}}| \propto v_\parallel^2,$$

ions at positions with $\widetilde{T} > 0$ will (on average) drift at higher speed v_{tor} than ions at positions with $\widetilde{T} < 0$. This leads to a periodic density perturbation $\widetilde{n}_i$ and, due to charge separation, a periodic perturbation in the electric potential $\widetilde{\Phi}$. Note that in this picture, the perturbation of the potential $\widetilde{\Phi}$ is in phase with the perturbation of the density $\widetilde{n}_i$, but out of phase with the perturbation of the temperature $\widetilde{T}$. [6]
Hence, the cross-phases are

$$\delta_{n,\Phi} = 0, \qquad \delta_{T,\Phi} = \frac{\pi}{2}. \tag{5.10}$$

The perturbed potential results in an electric field $\vec{E}$ that leads to an $E \times B$-drift $\vec{v}_E$. At positions with $\widetilde{T} < 0$, this drift $\vec{v}_E$ is directed towards the center of the plasma whereas at positions with $\widetilde{T} > 0$, it points outwards, thus propelling hotter plasma from central regions towards regions of lower temperature. Thereby, $\vec{v}_E$ amplifies the perturbation which finally leads to an instability. On the high-field side, the situation is opposite (see figure 5.2, left). Here, the $E \times B$-drift $\vec{v}_E$ works against the perturbation, thereby stabilizing the plasma.
The growth rate γ and the real frequency ω_r of the ITG instability can be computed

by taking moments of the linear gyrokinetic equation (5.6). [46] An easy way to compute the growth rate and the real frequency of an ITG mode is provided by a simple fluid model. [70] Assuming quasi-neutrality and neglecting parallel motion of ions due to their high inertia leads to a pure growing mode with growth rate [4]

$$\gamma = \omega_D \sqrt{2 \cdot \frac{R}{L_T}} = k_\theta \rho_s \frac{c_s}{R} \sqrt{2 \cdot \frac{R}{L_T}}. \tag{5.11}$$

In this equation, c_s denotes the ion sound speed and ρ_s denotes the ion sound gyroradius (or hybrid Larmor radius). These two quantities are defined by

$$c_s := \sqrt{\frac{T_e}{m_i}}, \qquad \rho_s := \frac{c_s}{\Omega_i}, \tag{5.12}$$

when Ω_i is the ion cyclotron frequency. Equation (5.11) shows that the growth rate increases monotonically with the logarithmic gradient of the temperature. A more complete treatment shows that an ITG mode only becomes unstable, if the normalized logarithmic gradient of the ion temperature exceeds a certain critical threshold value:

$$\frac{R}{L_{Ti}} > \frac{R}{L_{Ti,crit}} \tag{5.13}$$

In general, ITG modes are driven by R/L_{Ti} and stabilized by T_i/T_e and (in the adiabatic electron limit) R/L_n. [4, 37] Collisions were also found to reduce the growth rate γ at least slightly. [2] However, the collisionality dependence of ITG modes is much weaker than for trapped electron modes that will be introduced in section 5.3. ETG instabilities are driven by R/L_{Te}, unaffected by collisions and stabilized by T_e/T_i and R/L_n. [4]

5.3 Trapped Electron Mode (TEM)

Another important electrostatic micro-instability on the ion Larmor radius scale is the Trapped Electron Mode (TEM). In this section, we will first introduce an ideal drift wave which would be stable and then show why in a real tokamak, it is unstable.

In contrast to ETG or ITG instabilities (with $k_\parallel = 0$), such a drift wave requires a three-dimensional treatment. As shown in figure 5.3, a drift wave emerges from a

periodic pressure perturbation $\widetilde{p}$ with $k_{\parallel} \neq 0$, but $k_{\perp} \gg k_{\parallel}$. This means that the sinusoidal pressure perturbation is not aligned with the magnetic field lines, which results in a non-zero component of the pressure gradient parallel to $\vec{B}$. Due to their high mobility along the field lines, electrons respond immediately and move to regions of lower pressure. Therefore, positive charge accumulates in regions with $\widetilde{p} > 0$ and negative charge accumulates in regions with $\widetilde{p} < 0$, thereby creating potential perturbation $\widetilde{\Phi}$ that is in phase with the pressure perturbation. Hence, the cross-phase between pressure and potential is $\delta_{p,\Phi} = 0$.

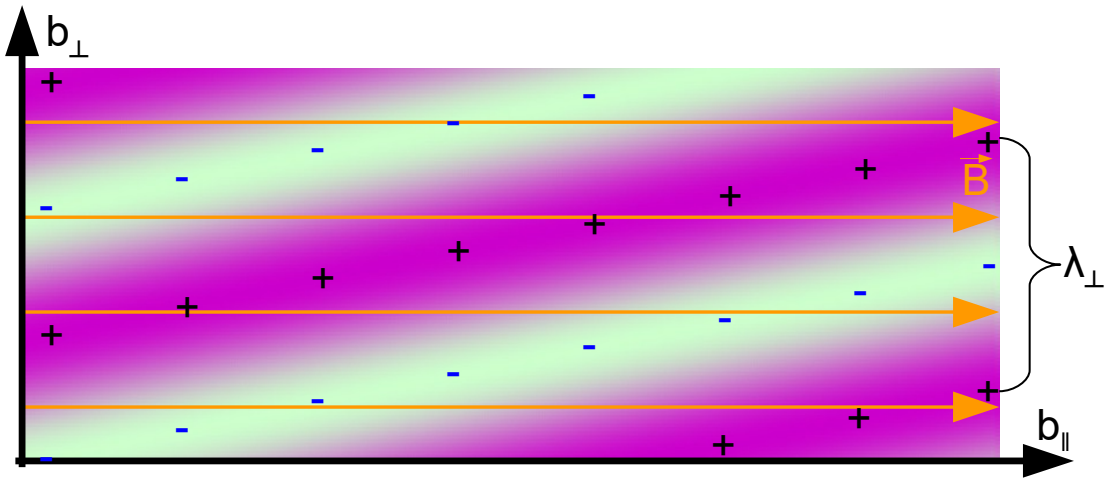

Figure 5.3: Regions with $\widetilde{p} > 0$ are coloured with magenta whereas regions with $\widetilde{p} < 0$ are bright. Such an initial sinusoidal pressure perturbation leads to a perturbation of the electric potential $\widetilde{\Phi}$. Under the assumption of adiabatic electrons, both perturbations are in phase.

Since the cross-phase is zero, the resulting electric field $\vec{E} = -\nabla\widetilde{\Phi}$ does not lead to any radial transport. The $E \times B$-drift only leads to a stable propagation of the periodic pressure perturbation in the direction of the electron diamagnetic drift $\vec{u}_{dia,e} \propto (\vec{\nabla}p \times \vec{B})$. [67]

This drift wave is only stable if electrons are able to respond adiabatically. If, like in a real tokamak, electrons are not perfectly adiabatic, the potential perturbation $\widetilde{\Phi}$ is not in phase with the pressure perturbation $\widetilde{p}$, but lags behind. This amplifies the amplitude of the perturbation and leads to a drift-wave instability.

There are several effects preventing electrons from an immediate response. The major reason for the (in average) slow motion along the $\vec{B}$-field is the trapping of

electrons in banana orbits. [6, 4] Since the bounce frequency ω_{be} of trapped electrons is much higher than the drift frequency ω_D at ion Larmor radius scales, the bounce-averaged drift leads to an instability at those ion scales. But also electromagnetic perturbations [61], electron-ion collisions and (especially at high frequencies) the electron inertia itself contribute to a retarded response. [67]
Experimental results and theoretical results show that in general, TEM instabilities are stabilized by collisions. [57] On the other hand, trapped electron modes are driven by R/L_{Te}, R/L_n and destabilized by the temperature ratio T_e/T_i. [4]

5.4 Turbulence suppression and L-H transitions

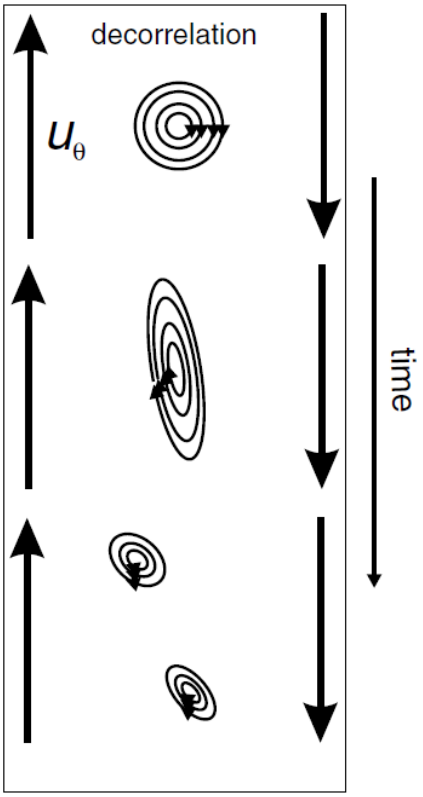

Figure 5.4: Sketch of the decorrelation mechanism. [66]

Sheared flows, such as $E \times B$ flows and zonal flows, can lead to a reduction of turbulent transport. [5, 12] There are two possible mechanisms that could explain this reduction of transport due to sheared flows. [38, 66]
An often considered process is the decorrelation mechanism which is schematically shown in figure 5.4 for a sheared flow in poloidal direction θ. In such a sheared flow, turbulent eddies are tilted and stretched which leads to an energy transfer from micro-turbulence to zonal flows. In strong shear flows, this elongation of eddies is followed by the breaking-up of eddies into smaller structures. This reduces the diffusive step size, thereby reducing turbulent transport. However, this breaking-up of eddies into pieces has not been observed in experiments yet. [66]
Another possible process is the straining-out mechanism which starts very similar to the decorrelation mechanism with a tilt and an elongation of the small turbulent eddies. However, in the straining-out process, this first step is not followed by a splitting-up of the eddies. Instead, the eddies

are further stretched and thinned out by the sheared flow until finally, they are taken over by the shear flow completely. This results in a complete transfer of the kinetic energy from the eddies to the zonal flow. Experimental evidence pointing towards the existence of such a mechanism was observed in low-temperature plasmas in the stellarator device TJ-K. [38] In general, it is also plausible that both, the decorrelation mechanism and the straining-out mechanism, play a role. [66]
Other mechanisms of turbulence reduction are the stabilization of electrostatic modes due to electromagnetic effects at high β_e [9] or due to the presence of impurities [41]. Also magnetic shear can lead to turbulence suppression due to radially varying pitch angles of the q-profile. [20]

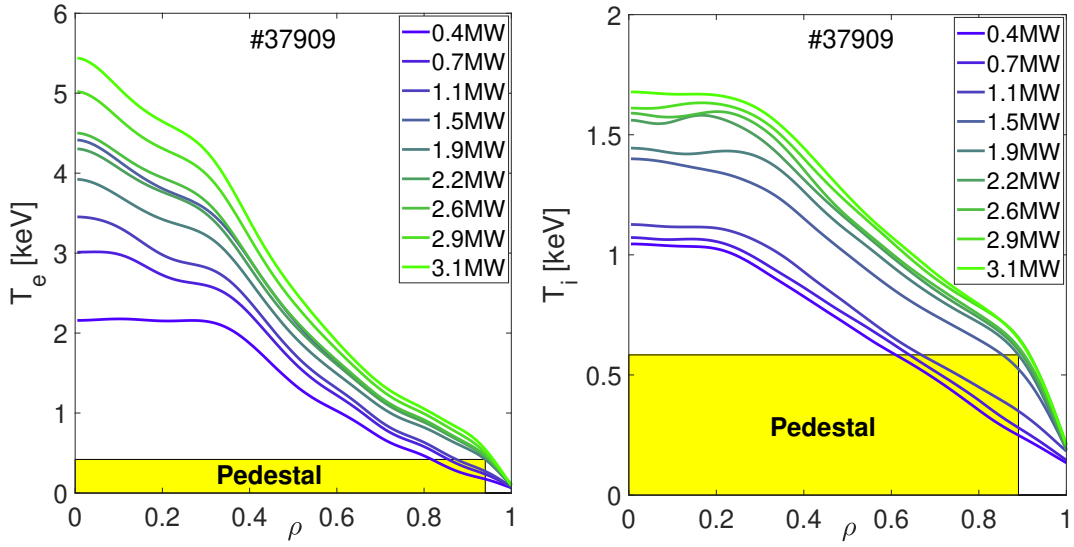

Figure 5.5: Electron (left) and ion (right) temperature profiles for a Deuterium shot (#37909). The different colours correspond to different ECRH heating powers. Around $P_{ECRH} \approx 1.9\ \mathrm{MW}$, an L-H transition occurs.

The most prominent example of turbulence suppression is the formation of a transport barrier close to the edge of the plasma if a certain threshold heating power is reached. This leads to a transition from a low-confinement state, called L-mode, to a high confinement state, called H-mode, in which energy and particle confinement are significantly improved. A typical characteristic of such an H-mode plasma is the occurrence of a pedestal in the electron and ion temperature profiles (see figure 5.5) and the density profiles which leads to elevated core profiles.
The threshold heating power P_{LH} at which the L-H transition occurs depends on

many different parameters. [59] In general, the required threshold heating power P_{LH} is lower if the grad-B drift points towards the X-point and higher if the grad-B drift points away from the X-point. Therefore, one calls the magnetic configuration "favourable" if $\vec{v}_{\nabla B}$ points in the direction of the X-point. Furthermore, the threshold heating power exhibits an inverse mass dependence. [56] The threshold heating powers of the three hydrogen isotopes are therefore linked in the following way:

$$P_{LH}(\mathrm{D}) = \frac{1}{2} \cdot P_{LH}(\mathrm{H}), \qquad P_{LH}(\mathrm{T}) = \frac{1}{3} \cdot P_{LH}(\mathrm{H}). \tag{5.14}$$

The material of the plasma-facing components has an effect on P_{LH}, too. A drop in P_{LH} by about 25% was observed in ASDEX Upgrade when the carbon wall was replaced by a tungsten wall. [59] On the other hand, magnetic field perturbations, for example due to an ELM mitigation system, were observed to increase the required heating power P_{LH} to achieve H-mode operation. In studies at the DIII-D tokamak, it was observed that the threshold heating power P_{LH} also increases with the toroidal rotation velocity close to the edge of the plasma. [21]
Two further dependencies are shown in figure 5.6. It is generally observed that the threshold heating power depends non-monotonically on the line-averaged density $\overline{n}_e$ of the plasma. This implies that there exists a density $\overline{n}_{e,min}$ at which the threshold heating power has a minimum and which separates the so-called low-density branch from the high-density branch. As one can see in figure 5.6 and as derived in [58], the position $\overline{n}_{e,min}$ of the minimum depends on the plasma current as $\overline{n}_{e,min} \propto I_p^{0.34}$. Moreover, one can see in figure 5.6 that the threshold P_{LH} is generally higher at higher plasma current. Last but not least, the threshold heating power P_{LH} depends also on the heating method. Lower values for P_{LH} are observed for heating methods in which fractions of the heating power are directly injected in the ion heat channel.
For Deuterium plasmas on the high-density branch in a tokamak with favourable magnetic configuration, a scaling law was developed for the threshold heating power by Y. R. Martin [39]:

$$P_{LH} = 0.0093 \cdot \overline{n}_e^{0.72} \cdot B_T^{0.80} \cdot S^{0.94}. \tag{5.15}$$

In this equation, $\overline{n}_e$ is the line-averaged density in $10^{19}\ \mathrm{m}^{-3}$, B_T the magnetic field strength in T, S the surface area of the plasma in m^2 and P_{LH} the threshold heating power in MW.

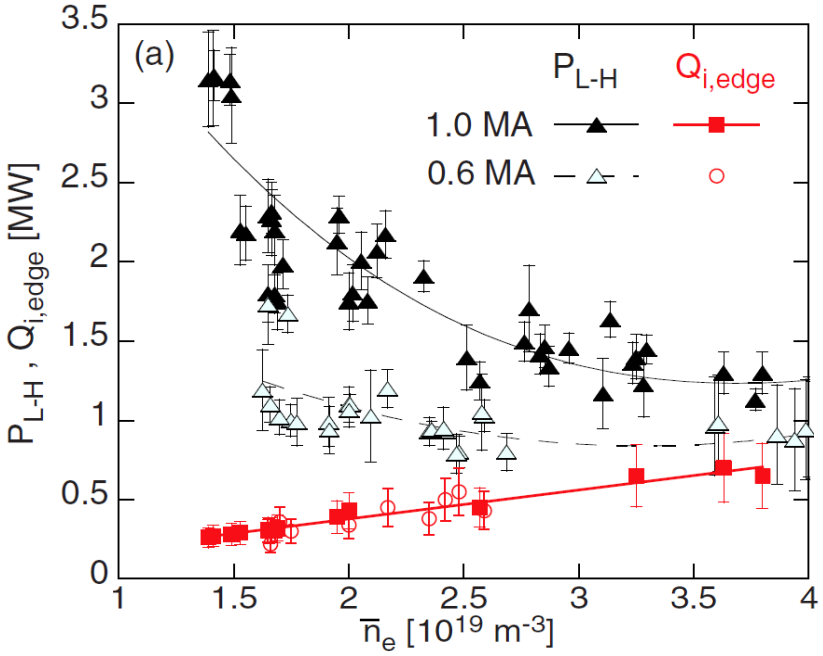

Figure 5.6: Threshold heating power P_{LH} and corresponding edge ion heat flux $Q_{i,edge}^{LH}$ at the L-H transition for different plasma currents I_p. Only the low-density branch is shown here. [58]

As shown in figure 5.6 for ASDEX Upgrade plasmas, data across different plasma currents can be unified by considering the ion heat flux $Q_{i,edge}^{LH}$ close to the edge of the plasma instead of the threshold heating power P_{LH}. Additionally, the edge ion heat flux does not show a non-monotonic dependence on $\overline{n}_e$, but a simple linear dependence on $\overline{n}_e$. For Deuterium plasmas in ASDEX Upgrade with favourable magnetic configuration and a magnetic field of $B_T = 2.35\ \mathrm{T}$, the scaling reads [58]

$$Q_{i,edge}^{LH} = 0.18 \cdot \overline{n}_e, \tag{5.16}$$

where $Q_{i,edge}^{LH}$ is in MW and $\overline{n}_e$ in $10^{19}\ \mathrm{m}^{-3}$. This scaling law is not only independent on the plasma current I_p, but also on the applied heating method.
This simple linear expression can be explained within a concept according to which an L-H transition is caused by a sheared equilibrium $E \times B$-flow. This $E \times B$-flow is induced by a negative radial electric field well $\vec{E}_r$ close to the edge of the plasma which can be determined from radial force balance, assuming that the poloidal ro-

tation is neoclassical and therefore negligibly small ($u_{\mathrm{pol}} \approx 0$): [66]

$$\vec{E}_r \approx \frac{\vec{\nabla} p_i}{e n_i} + u_{\parallel} B_p \vec{e}_r. \tag{5.17}$$

In this equation, p_i is the main ion pressure, n_i the main ion density, $u_{\parallel}$ the parallel flow velocity, B_p the poloidal magnetic field and $\vec{e}_r$ a unit vector in radial direction. During this master thesis, only ECRH-heated plasmas and ICRH-heated plasmas were examined. For these plasmas, the parallel flow velocity is negligibly small ($u_{\parallel} \approx 0$) such that equation (5.17) for the radial electric field simplifies to

$$\vec{E}_r = \frac{\vec{\nabla} p_i}{e n_i}. \tag{5.18}$$

Even in plasmas heated by other means than ECRH, the second term in equation (5.17) can often be neglected since the poloidal magnetic field is small at the edge. Decomposing the radial electric field of equation (5.18) into

$$E_r = \frac{1}{e}\left[\frac{\partial (k_B T_i)}{\partial r} + \frac{k_B T_i}{n_i}\frac{\partial n_i}{\partial r}\right]$$

and noting that the density n_i does not change considerably before the L-H transition when the heating power is increased, one can see that the gradient of the ion temperature $\partial T_i / \partial r$ is the main determinant of the radial electric field. On the other hand, the gradient of the ion temperature is also the drive of the ion heat flux $Q_i \propto n_i \cdot \partial T_i / \partial r$ which makes the edge ion heat flux a good indicator for the strength of the radial electric field well E_r close to the edge.
In a joint machine analysis including shots from ASDEX Upgrade and shots from Alcator C-Mod, a more general scaling for the edge ion heat flux was determined which also considers the dependence on the surface and the magnetic field [60]:

$$Q_{i,edge}^{LH} = 0.0029 \cdot \overline{n}_e^{1.05} \cdot B_T^{0.68} \cdot S^{0.93}. \tag{5.19}$$

The increase in $Q_{i,edge}^{LH}$ with increasing magnetic field is consistent with the Martin scaling (5.15) and can be explained by the inverse dependence of the $E \times B$ velocity on the magnetic field strength ($|\vec{v}_E| \approx E_r / B$). With increasing magnetic field B, also the magnitude of E_r increases that is required to achieve a critical $E \times B$-flow. Note that the exponent 1.05 ± 0.1 for the density dependence encompasses the

theoretically expected exponent of 1.00 in its error interval and that it is significantly larger than the exponent of 0.72 in the Martin scaling (5.15). For a typical ASDEX Upgrade plasma with $B_T = 2.5\ \mathrm{T}$ and $S = 43\ \mathrm{m}^2$, this would lead to an intersection of P_{LH} and $Q_{i,edge}^{LH}$ at $\overline{n}_e \approx 5 \cdot 10^{20}\ \mathrm{m}^{-3}$ with $Q_{i,edge}^{LH}$ exceeding P_{LH} at higher densities. This would lead to a contradiction between the Martin scaling (5.15) and the $Q_{i,edge}^{LH}$-threshold scaling (5.19) since $Q_{i,edge}^{LH}$ cannot be larger than P_{LH}. However, for reasonable operating densities, which are typically lower than $5 \cdot 10^{20}\ \mathrm{m}^{-3}$, it is $Q_{i,edge}^{LH} < P_{LH}$.

In purely ECRH-heated plasmas like in ITER-PFPO-1, edge ion heat fluxes $Q_{i,edge}$ are fully determined by the collisional electron-ion energy exchange (4.16) and thus, by the density profile $n_e(\rho)$ and the temperature profiles $T_i(\rho)$ and $T_e(\rho)$ of the core plasma. Precise predictions of the edge ion heat flux $Q_{i,edge}$ require precise predictions of core transport. This was the motivation of this master project to validate transport models for predominantly electron-heated plasmas.

6 Turbulent transport

6.1 Bohm and gyroBohm diffusion

The simplest model to describe transport locally is the Bohm diffusion. This model assumes displacements of the order of one hybrid Larmor radius ρ_s to happen in one ion gyroperiod $(\Omega_i/(2\pi))^{-1}$. [4] The Bohm diffusivity reads

$$\chi_B \propto \frac{\rho_s^2}{\Omega_i^{-1}} = \frac{T_e}{Z_i e B}, \tag{6.1}$$

where e denotes the elementary charge. Note that the Bohm diffusivity is independent of the main ion mass ($\chi_B \propto m_i^0$). The particle species only enters into the Bohm diffusivity with its charge number Z_i. Furthermore, there is no dependency on the geometry of the machine.
Analogously to Bohm diffusion, the gyroBohm diffusion considers a displacement of the order of one hybrid Larmor radius ρ_s happening on timescales of an inverse growth rate γ^{-1}, i. e. $\chi_{GB} \propto \rho_s^2 \gamma$. [4] Such a scaling for the diffusivity is obtained by multiplying the Bohm diffusivity χ_B with the relative gyroradius ρ_s/a_0. [68, 4] This yields the gyroBohm diffusivity:

$$\chi_{gB} := \frac{\sqrt{m_i} T_e^{3/2}}{Z_i^2 e^2 B^2 a_0} \propto \chi_B \cdot \frac{\rho_s}{a_0}. \tag{6.2}$$

Note that the gyroBohm diffusivity depends on the main ion mass as $\chi_{gB} \propto m_i^{1/2}$ while the Bohm diffusivity is independent of m_i.

6.2 Quasi-linear transport models

Electrostatic turbulent transport is the result of a fluctuating electric field $\vec{E}$ which leads to fluctuating $E \times B$ drifts in radial direction v_E (see chapter 5). For a known density perturbation $\widetilde{n}$, the flux-surface averaged particle flux $\widetilde{\Gamma}$ can be determined by the following equation [4, 3]:

$$\widetilde{\Gamma} = \langle \widetilde{n} \cdot v_E \rangle = \left\langle \int \mathrm{d}^3 v \, \widetilde{f} \, \frac{\vec{B} \times \vec{\nabla} \widetilde{\Phi}}{B^2} \cdot \hat{r} \right\rangle . \tag{6.3}$$

In this equation, $\hat{r}$ is a unit vector pointing in radial direction. Note that net transport is only created if the density perturbation $\widetilde{n}$ and the potential perturbation $\widetilde{\Phi}$ are out of phase ($\delta_{n,\Phi} \neq 0$). [67] Maximum particle transport is obtained for a cross-phase of $\delta_{n,\Phi} = \pi/2$.
Since non-linear gyrokinetic simulations require unaffordable amounts of CPU time, an important topic of research are quasi-linear transport models that rely on reduced physics models. [10] In these models, a large part of the calculations is performed in Fourier space and the flux-surface averaged particle flux is obtained by a Fourier series of the form [3]

$$\widetilde{\Gamma} = \left\langle \sum_{k,\omega} \mathrm{Re} \left[\frac{i k_y \widetilde{n}_{k\omega} \widetilde{\Phi}^*_{k\omega}}{B \cdot |\widetilde{\Phi}_{k\omega}|^2} \right] |\widetilde{\Phi}_{k\omega}|^2 \right\rangle . \tag{6.4}$$

Since the energy of a particle is determined by $E = 3p/(2n)$, the (electron and ion) heat flux densities q can be computed analogously:

$$q = \left\langle \sum_{k,\omega} \mathrm{Re} \left[\frac{3}{2} \cdot \frac{i k_y \widetilde{p}_{k\omega} \widetilde{\Phi}^*_{k\omega}}{B \cdot |\widetilde{\Phi}_{k\omega}|^2} \right] |\widetilde{\Phi}_{k\omega}|^2 \right\rangle . \tag{6.5}$$

The exact form of these equations for $\widetilde{\Gamma}$ and q varies from model to model, but they exhibit a common structure in all quasi-linear transport models. The terms in square brackets are called quasi-linear weights (QL weights) and give the phase relations between the fluctuating quantities. These QL weights are computed together with the spectra of growth rates γ and real frequencies ω_r in a first step from a linearized set of equations determining the properties of the micro-instabilities. It has been shown that, at least for core turbulence, the QL weights from linear simulations do

not deviate too much from the non-linear weights obtained by non-linear simulations which justifies the quasi-linear ansatz. [11, 8] In a second step, a quasi-linear saturation rule is used to calculate the saturation amplitudes $|\widetilde{\Phi}_{k\omega}|^2$ from the (ω and k) spectra of growth rates and real frequencies. Finally, the QL fluxes of particles and heat can be determined.

6.2.1 Trapped gyro-Landau fluid (TGLF) model

The trapped gyro-Landau fluid (TGLF) model is the successor of GLF23 in which the set of linearized equations used to determine γ and ω_r is based on a gyrofluid description. [3] In the framework of this thesis, three different versions of TGLF with saturation rule SAT1 [65, 63] have been applied: the version of August 2019 which is calibrated on GYRO and the versions of December 2019 (a beta-version of February 2020) and February 2020 which are calibrated on CGYRO [64]. The focus of this thesis was put on the most recent version, i.e. the one of February 2020.

Saturation rule SAT1 is based on the observation in multi-scale simulations [28] (simulations that cover electron scales as well as ion scales) that zonal flow mixing (ZFM) is the dominant mechanism acting against linear growth of gyrokinetic turbulence. [65] The rate of zonal flow mixing γ_{ZFM} competing against the linear growth rate γ_{lin} can be determined by

$$\gamma_{ZFM} = k_\theta \cdot V_{ZF}, \tag{6.6}$$

where k_θ is the poloidal wavenumber of the mode on which ZFM acts and V_{ZF} is the root mean squared $E \times B$ drift velocity of the fluctuating zonal flows. Note that $\gamma_{ZFM} \propto k_\theta$ which makes zonal flow mixing being a strong mechanism also on electron (high-k_θ) scales. The velocity V_{ZF} is independent of k_θ. A fundamental assumption of SAT1 is that V_{ZF} grows until it reaches an equilibrium flow velocity determined by

$$V_{ZF} = \max_{k_\theta \rho_s < 0.8} \left\{ \frac{\gamma_{\mathrm{lin}}}{k_\theta} \right\}. \tag{6.7}$$

Note that the non-linear zonal flow drive is assumed to be the strongest on ion scales ($k_\theta \rho_s < 0.8$).

Furthermore, saturation rule SAT1 takes into account coupling betwen electron

scale transport and ion scale transport since it has been observed in multi-scale simulations that high-k_θ electron energy transport depends on ion-scale transport. According to a rule of thumb that has emerged from multi-scale simulations, the electron energy transport is dominated by the ion-scale contribution if

$$\max_{\text{ion-scale}} \left\{ \frac{\gamma_{\text{lin}}}{k_\theta} \right\} > \max_{\text{electron-scale}} \left\{ \frac{\gamma_{\text{lin}}}{k_\theta} \right\}.$$

Otherwise, the electron heat transport is dominated by the high-k_θ contribution which is known as the streamer regime.
Based on these assumptions, an effective growth rate γ_{model} and the root mean squared (RMS) width of the potential spectrum k_x^{RMS} are computed. Finally, the amplitude of the saturated potential can be computed according to

$$\widetilde{\Phi} = C_{\text{norm}} \cdot \frac{\gamma_{\text{model}}}{k_x^{\text{RMS}} k_\theta}. \tag{6.8}$$

In the version of August 2019, the prefactor C_{norm} has been determined by fitting against 70 ion-scale GYRO simulations. [63, 65]

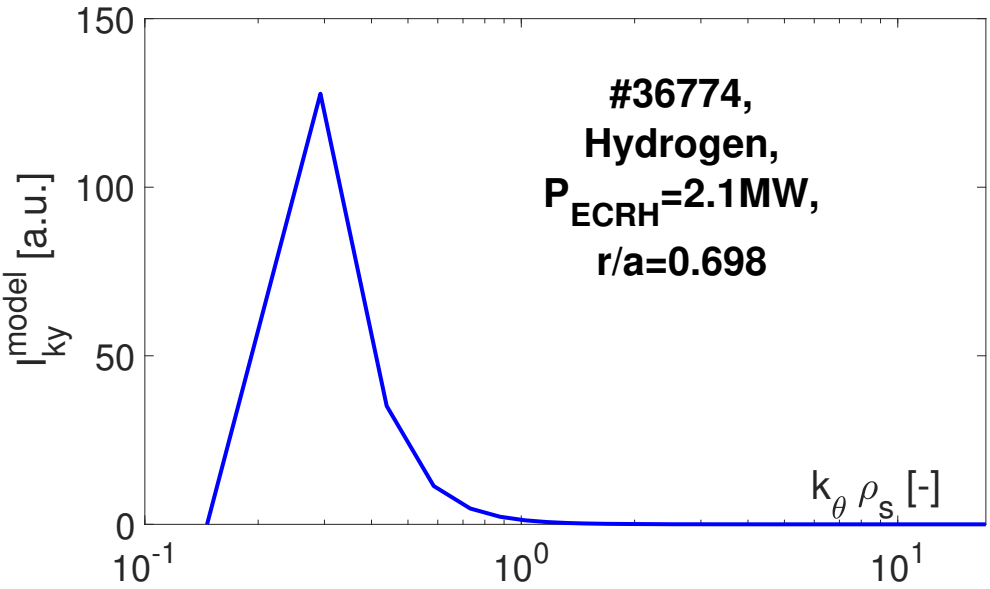

Figure 6.1: Poloidal wavenumber spectrum of the saturated potential intensity, as calculated with TGLF (Version February 2020).

In a real tokamak, the total magnetic field $B = B(\theta)$ and the gradient of the minor radius $|\vec{\nabla} r|$ are not constant across a flux surface, but depend on the poloidal angle θ. This geometric dependence has been neglected in the version of August 2019. The version of February 2020 generalizes the saturated potential amplitude $\widetilde{\Phi}_{k\theta} = \widetilde{\Phi}_{k\theta}(\theta)$ to be dependent on θ and determines the quasi-linear potential intensity $|\widetilde{\Phi}_{k\theta}|^2$ as the following flux surface average

$$|\widetilde{\Phi}_{k\theta}|^2 = \left\langle \left(\widetilde{\Phi}_{k\theta}(\theta) \right)^2 \right\rangle_\theta = \left\langle G^2(\theta) \right\rangle_\theta \cdot \left(\frac{\gamma_{\mathrm{model}}}{k_x^{\mathrm{RMS}} k_\theta} \right)^2 . \tag{6.9}$$

In the second equality, all dependencies on the geometric shape were absorbed in the function $G(\theta)$. Figure 6.1 shows a typical spectrum of the potential intensity $|\widetilde{\Phi}_{k\theta}|^2$ determined with the version of February 2020.
In TGLF-Feb20, the fitting coefficients were determined by fitting the model against 10 CGYRO simulations for pure deuterium plasmas with different elongations κ and different Shafranov shifts. [64] The beta version of TGLF of December 2019 is calibrated on CGYRO, too. However, the implemented geometrical factor is less sophisticated than in the official version of February 2020.

6.2.2 QuaLiKiz

QuaLiKiz is a quasi-linear transport model which is based on the gyrokinetic code KineZero and which solves a simplified linearized gyrokinetic dispersion relation in order to obtain its eigenvalues (the growth rate γ and the real frequency ω_r). [7, 3] The corresponding eigenfunctions are determined in the fluid limit of this linear dispersion relation and not together with γ and ω_r.
Fundamental assumptions of QuaLiKiz are circular flux surfaces and a large aspect ratio of the tokamak which makes this model inappropriate for the description of spherical tokamak plasmas or strongly shaped plasmas. [10] Collisions of trapped electrons are modeled with a Krook collision operator. Collisions of passing electrons and (trapped or passing) ions are neglected. [7] Furthermore, QuaLiKiz considers only electric potential fluctuations and does not solve Ampère's law. [10] This assumption can be rephrased to assuming $\beta_e := 2\mu_0 p_e / B^2 = 0$ (μ_0 the vacuum permeability and p_e the electron plasma pressure). [24] As a result of this assumption, electromagnetic modes such as kinetic ballooning modes and micro-tearing modes

cannot be described within the QuaLiKiz model.
The saturated potential intensity $|\widetilde{\Phi}_{k\omega}|^2$ is determined in a two-step process in QuaLiKiz. First, the position k_{max} of the maximum of the saturated potential intensity $|\widetilde{\Phi}_{k\omega}|^2$ is determined according to [7]

$$k_{max} = \arg\left\{\max\left\{\frac{\gamma}{\langle k_\perp^2\rangle}\right\}\right\}. \tag{6.10}$$

In this equation $\langle k_\perp^2\rangle := k_\theta^2 + k_r^2$ where $k_r = k_r(k_\theta, q, s)$ is a function of the poloidal wavenumber k_θ, the safety factor q and the magnetic shear s.

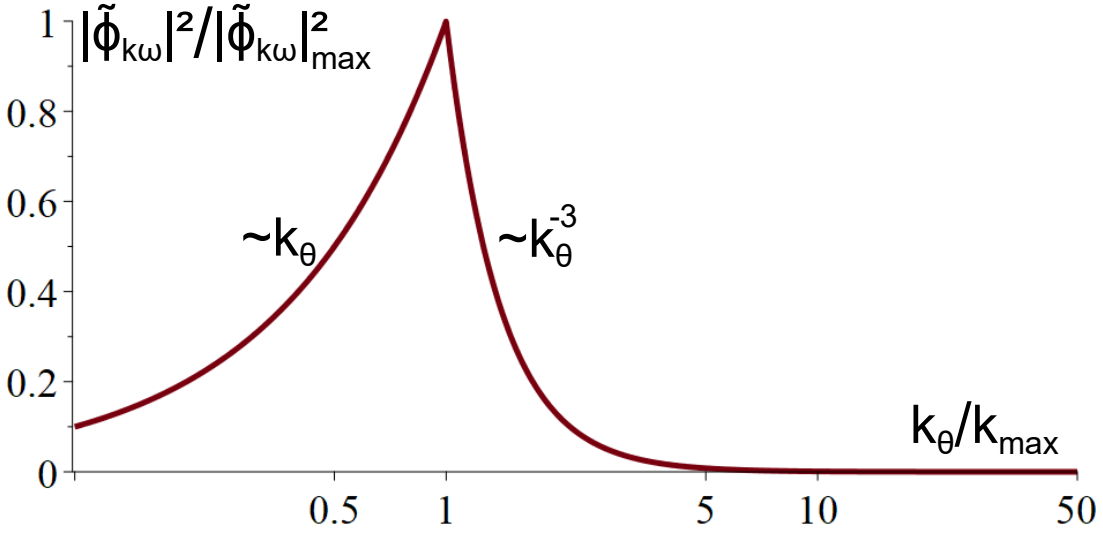

Figure 6.2: Poloidal wavenumber spectrum of the saturated potential intensity as computed in QuaLiKiz.

In a second step, the wavenumber spectrum of $|\widetilde{\Phi}_{k\omega}|^2$ is constructed assuming a linear increase of the saturation amplitude until k_{max} and a decay as k_θ^{-3} beyond the maximum:

$$|\widetilde{\Phi}_{k\omega}|^2 = |\widetilde{\Phi}_{k\omega}|^2_{max} \cdot \begin{cases} \frac{k_\theta}{k_{max}} & \text{if } k_\theta < k_{max} \\ \left(\frac{k_\theta}{k_{max}}\right)^{-3} & \text{if } k_\theta \geq k_{max}. \end{cases} \tag{6.11}$$

The k_θ^{-3}-dependence for large wavenumbers is motivated by experimentally observed decays of the density fluctuation spectrum. Figure 6.2 shows the shape of the saturation amplitude in k_θ-space, as it is implemented in QuaLiKiz. The mag-

nitude of the saturation amplitude is determined by multiplying its profile with a constant that is determined by fitting the model against a non-linear simulation.
The most recent version of QuaLiKiz [10] which has been used in the framework of this thesis has been improved by a numerically optimized dispersion relation solver that allows for computational times that are comparable to TGLF. Furthermore, the newest version of QuaLiKiz contains a recalibrated ETG model.

7 Experimental database

The database contains a total number of 16 shots, corresponding to 70 data points. 12 of these shots (corresponding to 66 data points) were performed at ASDEX Upgrade whereas 4 shots (corresponding to 4 data points) were performed at JET. In the following two sections, the experimental setups during these shots will be introduced.

7.1 Shots from ASDEX Upgrade

The 66 data points from ASDEX Upgrade can be further divided into three groups:

- 13 hydrogen (H) data points for which the magnetic field was $B_t \approx 2.5\ \mathrm{T}$ and the plasma current was $I_p \approx 0.83\ \mathrm{MA}$, leading to an edge safety factor of about $q_{95} \approx 5$
- 34 deuterium (D) data points at a magnetic field of $B_t = 2.4 - 2.5\ \mathrm{T}$ and a plasma current of $I_p \approx 0.83\ \mathrm{MA}$, leading to an edge safety factor of about $q_{95} \approx 5$
- 19 deuterium data points with the same magnetic field magnetic field of $B_t \approx 2.5\ \mathrm{T}$, but a larger plasma current of $I_p \approx 1.2\ \mathrm{MA}$, resulting in more twisted magnetic field lines with $q_{95} \approx 3.7$

All these shots were performed in favourable magnetic configuration such that the drift $\vec{v}_{\mathrm{in}}$ resulting from toroidal geometry points towards the X-point. The elongation was in the range of $\kappa = 1.5 - 1.6$.
Since in PFPO-1, ITER will operate with hydrogen (and helium) plasmas at an edge safety factor of $q_{95} = 3.0$, we also proposed some hydrogen shots at higher current/ lower q_{95}. Unfortunately, the experimental data for these shots became available

too late to still be analyzed during this master project.
Figure 7.1 shows the time traces of a very typical shot in the database. As one can see in the top panel, the ECRH power was increased (in some shots decreased) in step-like functions. Such ECRH power ramps allow us to obtain several data points out of a single shot. The time interval of each step was chosen long enough such the plasma could reach a steady state ($P_{\mathrm{loss}} = P_{\mathrm{heat}}$).

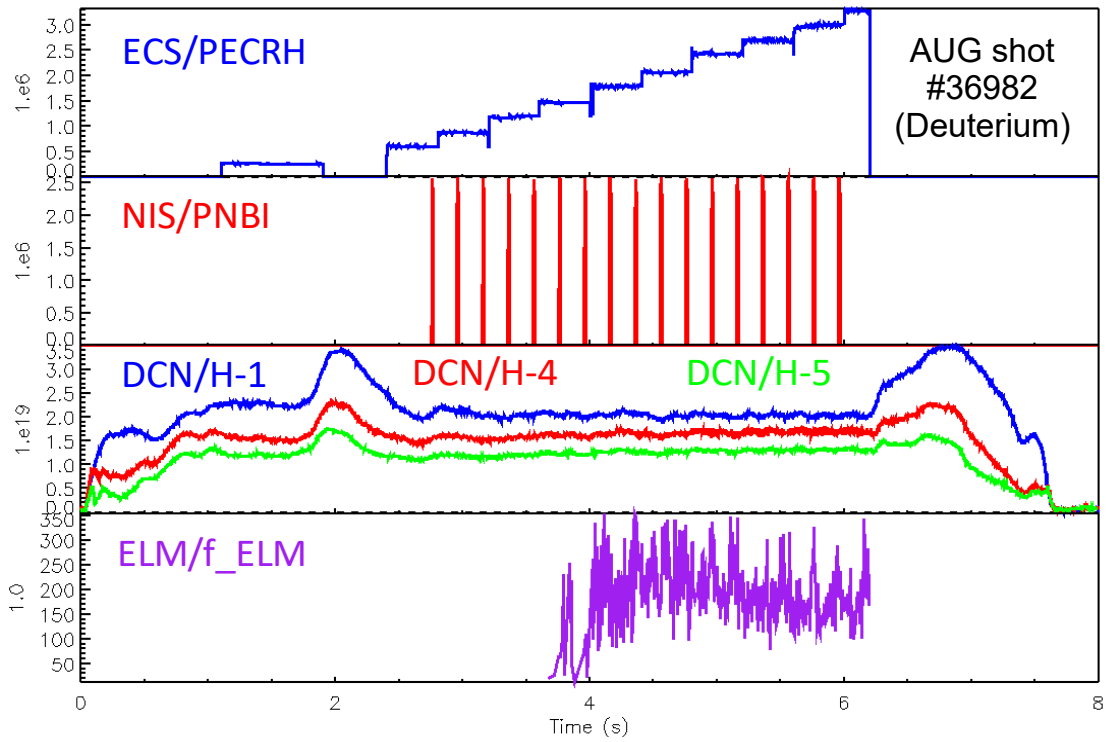

Figure 7.1: Time traces of different quantities for shot #36982. The top panel shows the ECRH power deposited to the plasma in W. Below, the deposited NBI power is shown in W. The third panel gives the line-integrated density in m^{-2} along three different lines of sight. The bottom panel shows the ELM frequency in Hz.

NBI blips were used to obtain measurements of the toroidal rotation and the ion temperature T_i via charge exchange recombination spectroscopy (CXRS). The CXRS diagnostic works by recording the emission spectra of impurities undergoing charge exchange reactions. The mean Doppler shift of the spectral lines yields the toroidal rotation velocity whereas the Doppler broadening of the spectral lines yields the temperatures of the respective impurity ions. Assuming that all ions, i.e. impurity

ions and main ions, are in thermal equilibrium and all ions rotate together with the same velocity, this yields the overall plasma rotation and the ion temperature T_i of the main ions. [6] It has been shown in [40] that short beam blips do not change the shape of the toroidal rotation profiles and that average toroidal rotations during a beam blip are only about $5\ \mathrm{km/s}$ higher than the intrinsic rotation of the plasma. As the three DCN interferometry signals in figure 7.1 show, the density during the discharges was kept constant if this was possible. Figure 7.2 gives the distribution of the data points over the different density levels and ECRH power levels. All considered discharges are on the low-density branch with line-averaged densities ranging from $\overline{n}_e \approx 1.8 \cdot 10^{10}\mathrm{m}^{-3}$ to $\overline{n}_e \approx 4.5 \cdot 10^{10}\mathrm{m}^{-3}$. Such low densities are necessary in our analysis since for high densities, the electron and ion heat fluxes cannot be separated any more because of $P_{ei} \propto n_e^2$. Furthermore, one-third field operation in ITER-PFPO-1 is planned at very low densities of $\overline{n}_e \leq 2 \cdot 10^{10}\mathrm{m}^{-3}$ [76] since the threshold heating power for L-H transitions is expected to exhibit its minimum at $\overline{n}_{e,min} \approx 1.4 \cdot 10^{10}\mathrm{m}^{-3}$.

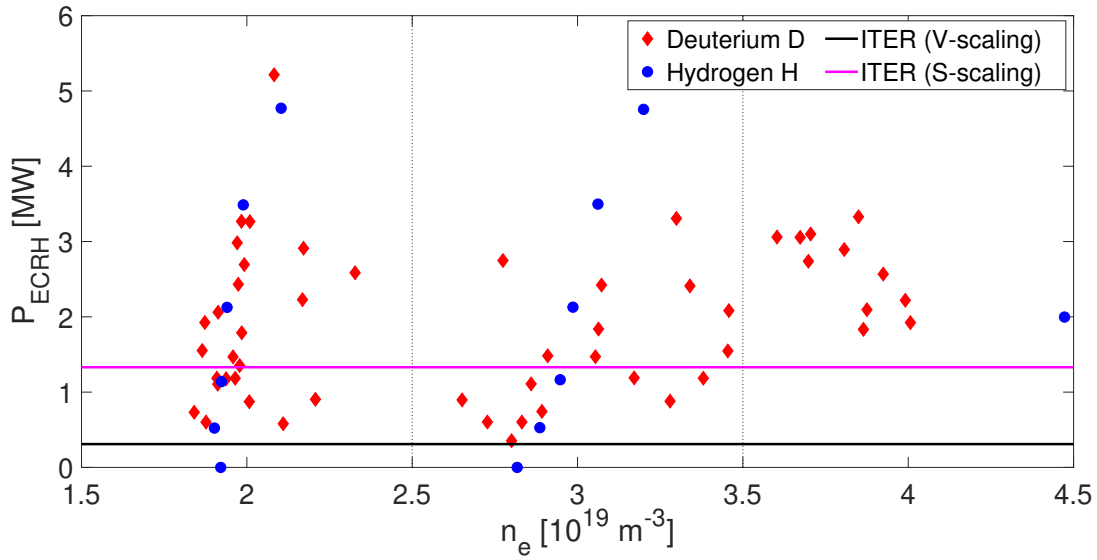

Figure 7.2: Distribution of the data points over different line-averaged densities and different ECRH powers.

The different ECRH power levels covered by the database range from $P_{ECRH} = 0\ \mathrm{MW}$ (Ohmic operation) up until $P_{ECRH} = 5.2\ \mathrm{MW}$. The horizontal lines in figure 7.2 give an attempt to scale down ITER's $20\ \mathrm{MW}$ in PFPO-1 to the correspond-

ing ECRH power in ASDEX Upgrade. The V-scaling assumes the same heating power per volume element which leads to $P_V = 0.3\ \mathrm{MW}$ in ASDEX Upgrade. The S-scaling assumes the same heating power per surface element, resulting in $P_S = 1.3\ \mathrm{MW}$ for ASDEX Upgrade. Note that the threshold heating power P_{LH} (equation (5.15)) as well as the threshold edge ion heat flux $Q^{LH}_{i,edge}$ (equation (5.19)) are approximately proportional to the surface which makes the S-scaling the more reasonable one.
Since a wide range of ECRH power levels was covered, the database contains L-mode plasmas as well as H-mode plasmas. Furthermore, the database also contains plasmas in I-phase (which are considered as L-mode plasmas throughout this thesis, consistent with [59]), as it can be seen in figure 7.1. In this example shot, the plasma starts in pure L-mode before it transitions to I-phase at $P_{ECRH} \approx 1.5\ \mathrm{MW}$, resulting in the fluctuations observed in the signal for the instantaneous ELM frequency, though no true ELMs are visible yet.

7.2 Shots from JET

In contrast to ASDEX Upgrade, JET is not equipped with an ECRH heating system, though with Neutral Beam Injection (NBI), lower hybrid heating and an ICRH system. The latter consists of four so-called A2 antennas operating in the frequency range from $23\ \mathrm{MHz}$ to $57\ \mathrm{MHz}$ and one ITER-like antenna operating in the frequency range of $29\ \mathrm{MW}$ to $51\ \mathrm{MW}$. [30]
All four shots in the database, #95465, #95846, #95848 and #95850, were predominantly heated by ICRH. Shots #95846, #95848 and #95850 also contain small amounts of NBI heating. The total auxiliary heating power $P_{\mathrm{aux}} = P_{\mathrm{ICRH}} + P_{\mathrm{NBI}}$ coupled to the plasma ranges from $P_{\mathrm{aux}} = 4.7\ \mathrm{MW}$ up until $P_{\mathrm{aux}} = 8.0\ \mathrm{MW}$. To obtain plasmas similar to those in ITER-PFPO-1 with high levels of electron heating, the four Deuterium plasmas were heated by H minority heating (H concentration of $3 - 6\%$). The resulting fraction of heating power deposited to the electron heat channel is $\geq 49\%$. Multiple resonances were used to allocate the heating power at different radial positions.
All four shots have been performed in favourable magnetic configuration ($\vec{v}_{\mathrm{in}}$ directed towards the X-point) with an elongation of $\kappa = 1.6 - 1.7$. The magnetic field was $B_t = 3.26\ \mathrm{T}$, the plasma current $I_p = 1.98\ \mathrm{MA}$, resulting in an edge safety

factor of $q_{95} \approx 5$. Like the shots at ASDEX Upgrade, also the JET plasmas were on the low-density branch with line-averaged densities of $\overline{n}_e = (2.6 - 2.9) \cdot 10^{19}\mathrm{m}^{-3}$. Figure 7.3 shows the example of a JET shot from the database which was heated by ICRH only. NBI blips were used to obtain information about ion temperatures and plasma rotation via charge exchange. As the interferometry signals in the bottom panel show, the density was kept constant over a period of several seconds.

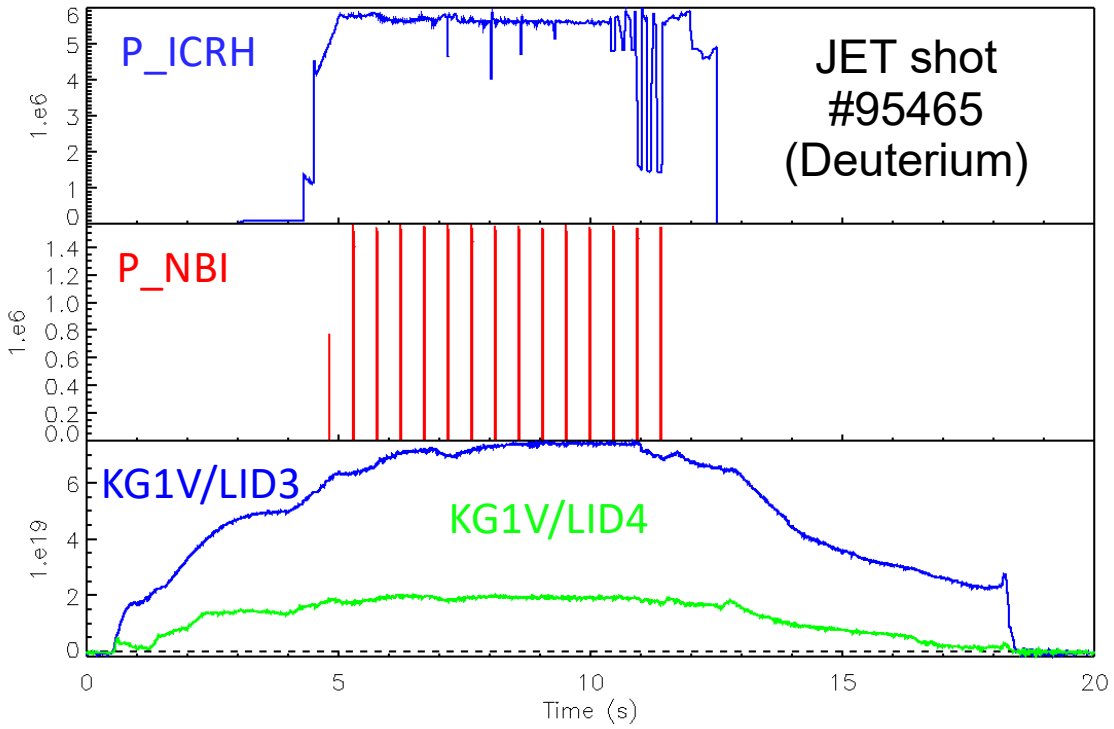

Figure 7.3: Time traces of different quantities for shot #95465 at JET. The top panel shows the ICRH power deposited to the plasma in W. Below, the deposited NBI power is shown in W. The bottom panel gives the core line-integrated density (KG1V/LID3) and the edge line-integrated density (KG1V/LID4) in m^{-2}.

8 Power balance analysis

Since it has been demonstrated in several studies that the edge ion heat flux is a crucial quantity for H-mode access (see section 5.4), a power balance simulation was performed for each plasma in the database. As explained in the previous chapter, all plasmas in the database were in a steady state. Periodic fluctuations due to sawtooth instabilities were eliminated in the input profiles of our simulations by averaging the profiles over at least one sawtooth period. Under such steady-state conditions, the transport equations (4.2) simplify to

$$\begin{aligned} \frac{\partial \Gamma_e}{\partial V} &= S_e \\ \frac{\partial}{\partial V}\left(Q_i + \frac{5}{2} T_i \Gamma_i\right) &= P_i \\ \frac{\partial}{\partial V}\left(Q_e + \frac{5}{2} T_e \Gamma_e\right) &= P_e \end{aligned} \tag{8.1}$$

Taking the volume integral of these equations allows to determine the particle flux Γ_e and the heat fluxes Q_e and Q_i if the sources $P_e(\rho)$, $P_i(\rho)$ and $S_e(\rho)$ are known. This can be done in ASTRA by assigning $T_e(\rho)$, $T_i(\rho)$ and $n_e(\rho)$ to their experimental profiles.

8.1 AUG plasmas with ECRH

In ASDEX Upgrade plasmas, the ion temperature profiles $T_i(\rho)$ were determined by charge exchange recombination spectroscopy (CXRS), as already mentioned in section 7.1. For measuring electron temperatures, ASDEX Upgrade is equipped with a Thomson scattering diagnostic and an electron cyclotron emission (ECE) diagnostic. Information about the density profile can be obtained from DCN interfer-

ometry, the Lithium beam diagnostic and also Thomson scattering. The final profiles $T_e(\rho)$ and $n_e(\rho)$ were determined by combining the information of the different diagnostics via integrated data analysis (IDA). [19] Only for plasmas at high P_{ECRH}, raw ECE data was used for central electron temperatures.
The model file used for power balance simulations of ECRH-heated ASDEX Upgrade plasmas can be found in appendix A. In these simulations, the power deposited to electrons and ions was determined by

$$P_e = P_{\mathrm{Ohm}} + P_{\mathrm{EBM}} + P_{ECRH} - P_{\mathrm{rad}} - P_{ei}, \tag{8.2}$$

$$P_i = P_{\mathrm{IBM}} + P_{ei}. \tag{8.3}$$

In these equations, P_{Ohm} denotes the Ohmic heating power, determined according to equation (4.12), P_{ECRH} is the ECRH power, determined by the beam tracing code TORBEAM [53], and P_{EBM} and P_{IBM} denote the NBI heating of electrons and ions, respectively, which were determined by RABBIT [71]. The radiation power P_{rad} was reconstructed from the tungsten (W) content in the plasma. If data from the GIW diagnostic was available, these W concentrations were used. Otherwise, a tungsten concentration of $5 \cdot 10^{-5}$ was assumed.
The collisional electron-ion energy transfer P_{ei} was determined according to equation (4.16). Note that P_{ei} depends on the mass number A_i of the main ions which is $A_i = 1$ for pure H plasmas and $A_i = 2$ for pure D plasmas. For one H datapoint with a small ($\approx 5\%$) D concentration, an effective mass $A_i = 1 + n_D/(n_H + n_D)$ was determined. This datapoint will be treated as regular H plasma in the following since it was shown in [52] that the thresholds P_{LH} and $Q^{LH}_{i,edge}$ depend non-linearly on $n_D/(n_H + n_D)$ and that small concentrations of D up to 20% have no effect on the values of the thresholds P_{LH} and $Q^{LH}_{i,edge}$.
The effective charge of the plasma

$$Z_{eff} := \sum_j \frac{n_{i,j}}{n_e} Z_j^2 \tag{8.4}$$

was adjusted such that the loop voltages of experiment and simulation coincide. This approach is based on the Z_{eff}-dependence of the conductivity $\sigma_{\|}$. From this effective charge Z_{eff} and the quasi-neutrality condition, an effective impurity with density $n_{imp} \propto n_e$ was calculated and given the charge $Z_{imp} = 5$ and mass $A_{imp} = 10$ of the main impurity boron.

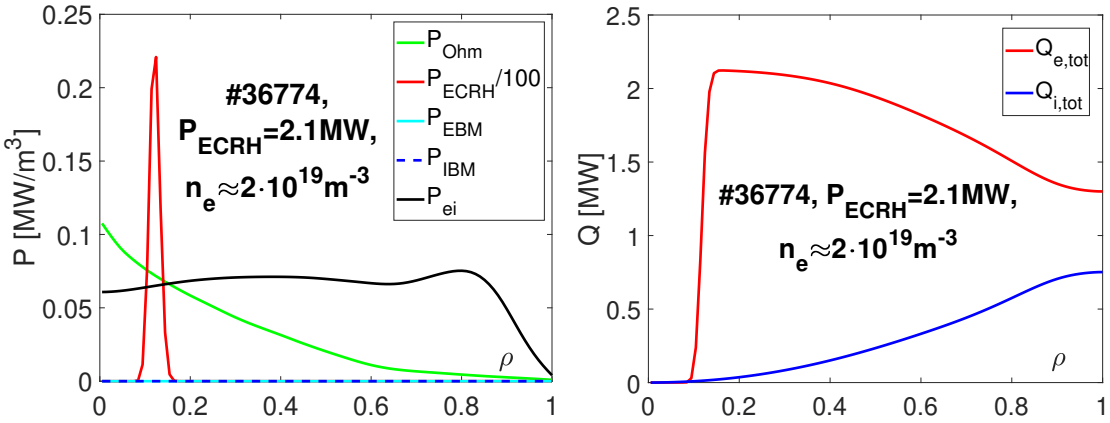

Figure 8.1: Left: Radial distribution of the different contributions to the heating power. Note that the ECRH power has been divided by 100. Right: Radial profiles of the electron heat flux $Q_{e,tot}$ and the ion heat flux $Q_{i,tot}$.

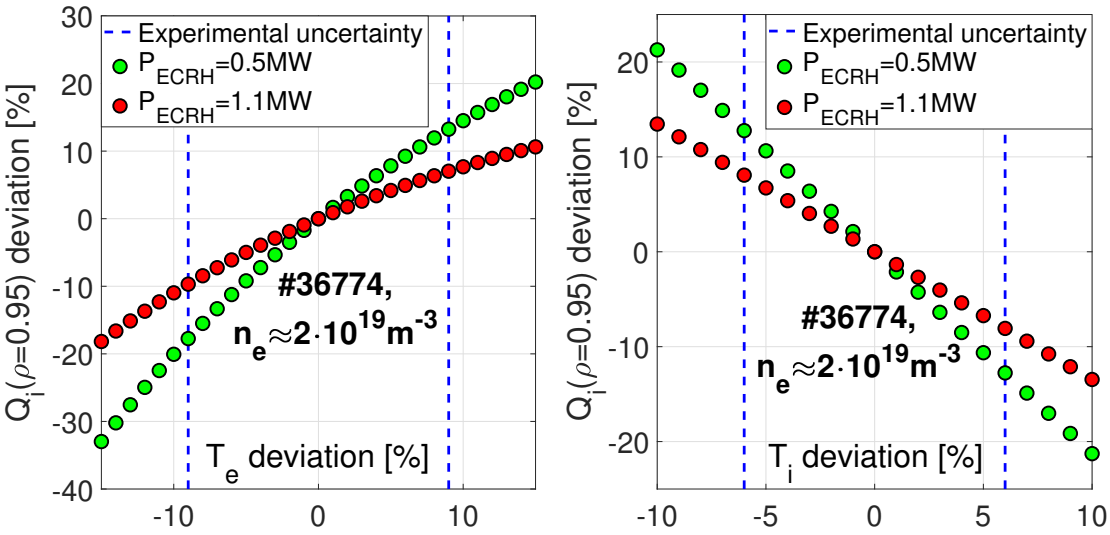

Figure 8.2: Sensitivity analysis for the edge ion heat flux. The effect of electron temperature deviations at fixed T_i (left) and ion temperature deviations at fixed T_e (right) is examined for two hydrogen plasmas.

Figure 8.1 shows an example of the power distribution in the plasma and the resulting heat flux profiles. The major sources of electron heating were Ohmic heating and especially ECRH heating, whereas NBI heating due to beam blips was negligibly small. ECRH power was mostly deposited between $\rho = 0.1$ and $\rho = 0.2$ in all shots which leads to a strong increase of $Q_{e,tot}$ at this position. P_{Ohm} is large

in the centre of the plasma and vanishes with increasing ρ since the current density decreases towards the edge. Ions were predominantly heated by collisional electron-ion heat transfer P_{ei} which leads to an increase in $Q_{i,tot}$ and an associated decrease of $Q_{e,tot}$ towards the edge.

The value of the edge ion heat flux $Q_{i,edge}$, which is evaluated at $\rho = 0.95$ in the framework of this thesis, depends on the n_e-, T_e- and T_i-profiles. Therefore, errors in these three profiles can lead to errors in $Q_{i,edge}$. Figure 8.2 shows a sensitivity analysis with respect to the temperature profiles. The left plot shows results from simulations in which the entire electron temperature profile was decreased or increased up to 15%. The experimental uncertainty for T_e measurements is $\pm 9\%$, leading to a maximum error for the edge ion heat flux of 10% at $P_{ECRH} = 1.1$ MW and 18% at $P_{ECRH} = 0.5$ MW. In both cases, $Q_{i,edge}$ increases with increasing T_e but the effect of uncertainties is weaker at $P_{ECRH} = 1.1$ MW than at $P_{ECRH} = 0.5$ MW. This is a result of the non-monotonicity of $P_{ei}(T_e)$ at fixed T_i (see figure 4.2) and the fact that T_e/T_i is higher at higher ECRH power.

The right plot of figure 8.2 shows the effect of ion temperature deviations on the edge ion heat flux. Experimental uncertainties for T_i measurements are $\pm 6\%$, leading to errors of up to 9% at $P_{ECRH} = 1.1$ MW and 13% at $P_{ECRH} = 0.5$ MW. In general, $Q_{i,edge}$ decreases with increasing T_i because the difference $(T_e - T_i)$ decreases with increasing ion temperature. Note that (neglecting small effects from the Coulomb logarithm) the error in $Q_{i,edge}$ is a linear function of the error in the ion temperature. If the measured ion temperature is $(1 + c) \cdot T_i$ with the true ion temperature T_i and error c, then the absolute error of the collisional electron-ion energy exchange (and thus, also the error of $Q_{i,edge}$) is a linear function of the error in the ion temperature profile: $\Delta P_{ei} \propto -c \cdot T_i/(T_e)^{3/2}$. Since higher ECRH power results in higher T_e, this proportionality also explains the different slopes observed in the right plot of figure 8.2.

Figure 8.3 shows the edge ion heat fluxes $Q_{i,edge}$, evaluated at $\rho = 0.95$, for all 13 hydrogen data points. The error bars were calculated as demonstrated in figure 8.2, assuming that experimental errors in T_e and T_i are completely uncorrelated. For one data point, for which the electron heat flux was initially negative ($Q_{e,edge} < 0$), the heat fluxes were adjusted such that $Q_{e,edge} = 0$. The different density levels are marked in different colours. One observes that for fixed ECRH power $P_{ECRH} > 0$, higher edge ion heat fluxes are obtained for higher densities. This can be explained by the fact that coupling between electrons and ions increases with increasing den-

sity according to $P_{ei} \propto n_e^2$. For a fixed density level, one observes a concave curve for $Q_{i,edge}(P_{ECRH})$ that goes into saturation for high ECRH power. This can be explained by the temperature dependence $P_{ei} \propto (T_e - T_i)/T_e^{3/2}$ of the electron-ion heat transfer. With increasing P_{ECRH}, not only the electron temperature T_e itself (and T_i), but also the ratio T_e/T_i increases. However, as seen in figure 4.2, the electron-ion heat exchange P_{ei} exhibits a maximum for $T_e/T_i = 3$ which leads to the concave curve for $Q_{i,edge}(P_{ECRH})$. Deuterium shots at $q_{95} \approx 5$ show similar characteristics to the ones observed for hydrogen in figure 8.3.

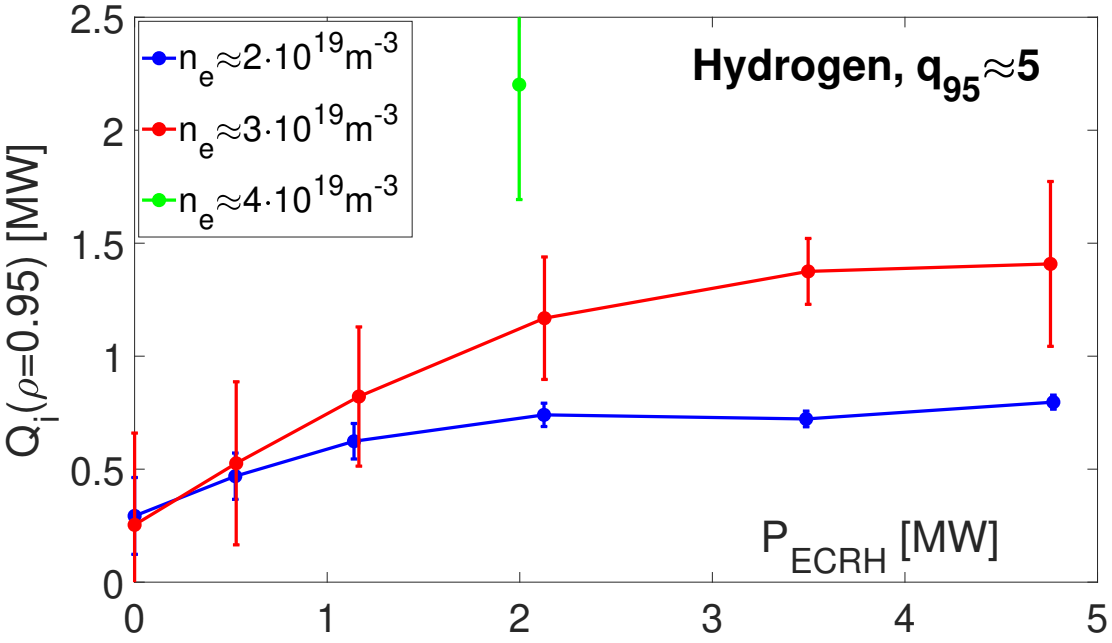

Figure 8.3: Edge ion heat fluxes as obtained from power balance simulations for all 13 hydrogen data points.

Piecewise concave curves $Q_{i,edge}(P_{ECRH})$ for fixed density level and increasing $Q_{i,edge}$ with increasing line-averaged density $\overline{n}_e$ can also be observed for Deuterium plasmas at a lower (and more ITER-like) edge safety factor of $q_{95} \approx 3.7$, as one can see in figure 8.4. Furthermore, two out of three shots in this figure show a transition from L-mode to H-mode, which can be clearly identified by a sudden increase in $Q_{i,edge}$. This jump in $Q_{i,edge}$ can be explained mainly by the sudden increase in density at an L-H transition and the resulting increase in $P_{ei} \propto n_e^2$. Especially shot #37909 shows this feature very clearly since the data points change colour from red to green after the transition.

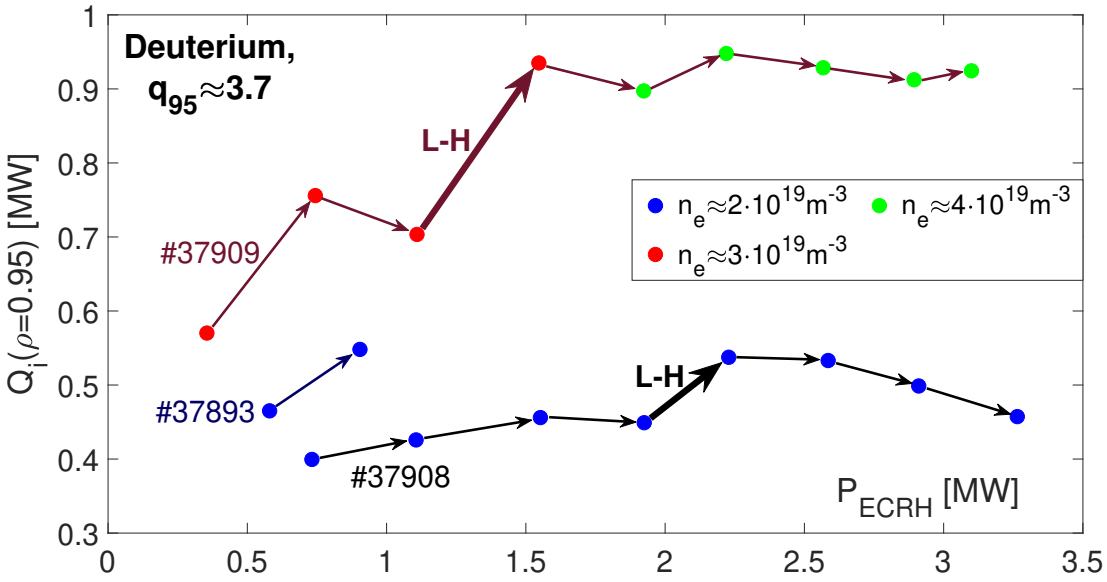

Figure 8.4: Edge ion heat fluxes for three deuterium shots at low q_{95}. L-H transitions are marked with fat arrows.

For a typical ASDEX Upgrade deuterium plasma in our database ($S \approx 44\ \mathrm{m}^2$, $B_T \approx 2.48\ \mathrm{T}$), the threshold edge ion heat flux for an L-H transition can be determined according to equation (5.19) to be

$$Q_{i,edge}^{LH} = 0.182 \cdot \overline{n}_e, \tag{8.5}$$

where $\overline{n}_e$ is the line-averaged density in $10^{19}\mathrm{m}^{-3}$. In this equation, the theoretically expected exponent of 1.00 was taken for the $\overline{n}_e$-dependence since this exponent could not be disproven in experiments. For hydrogen plasmas, the threshold edge ion heat flux is twice as high as for deuterium ($Q_{i,edge}^{LH}(H) = 2 \cdot Q_{i,edge}^{LH}(D)$), as it was shown experimentally in [52].

Figure 8.5 shows the results for all points with $\overline{n}_e \approx 2 \cdot 10^{19}\ \mathrm{m}^{-3}$ in the database and compares them with the thresholds $Q_{i,edge}^{LH}$. There are two hydrogen data points with $Q_{i,edge} > Q_{i,edge}^{LH}$ although none of them is in H-mode. For deuterium, most data points lie above the threshold $Q_{i,edge}^{LH}$. Accordingly, a large fraction of the data points is either in I-phase or in H-mode. Despite the higher confinement expected in deuterium plasmas at $q_{95} \approx 3.7$, the values for $Q_{i,edge}/\overline{n}_e$ do not differ significantly from the values at $q_{95} \approx 5$ in figure 8.5. Similar results were obtained also at $\overline{n}_e \approx 3 \cdot 10^{19}\ \mathrm{m}^{-3}$ and $\overline{n}_e \approx 4 \cdot 10^{19}\ \mathrm{m}^{-3}$. According to [59, 58], higher plasma

current/ lower q_{95} should result in a higher threshold heating power P_{LH} at the low-density branch.

Comparing the results for different main ion species in figure 8.5, one observes significantly larger values of $Q_{i,edge}/\overline{n}_e$ for hydrogen plasmas than for deuterium plasmas. This can be explained by the inverse dependence of the electron-ion energy exchange on the ion mass ($P_{ei} \propto m_i^{-1}$). Ceteris paribus, the ion heat flux would be twice as large for H than for D. Furthermore, we note that according to [56], H-mode access requires about twice the auxiliary heating power in hydrogen plasmas as in D plasmas ($P_{LH}(H) \approx 2 \cdot P_{LH}(D)$). This is consistent with the observation in figure 8.5 that the intersection of the edge ion heat flux $Q_{i,edge}$ with its critical value occurs at about twice the ECRH power in H plasmas than in D plasmas. The same observation is also made for $\overline{n}_e \approx 3 \cdot 10^{19}\ \mathrm{m}^{-3}$.

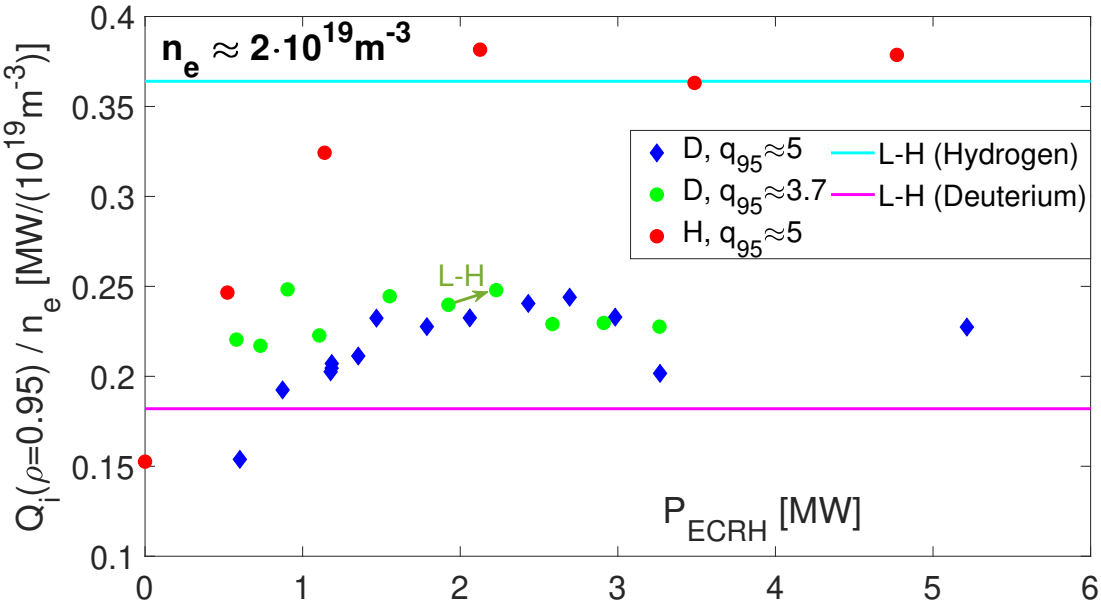

Figure 8.5: Comparison of deuterium shots at $q_{95} \approx 5$ with other deuterium shots at lower $q_{95} \approx 3.7$ and hydrogen shots (lower main ion mass) at the same $q_{95} \approx 5$. An L-H transition is marked by an arrow. The cyan and magenta lines are based on $Q_{i,edge}^{LH}/\overline{n}_e$ from equation (8.5).

8.2 JET plasmas with ICRH

In contrast to ASDEX Upgrade, JET is equipped with a high resolution Thomson scattering (HRTS) diagnostic which has been used to determine the electron density profiles $n_e(\rho)$ by averaging the HRTS-values over at least 0.4 s. Electron temperature profiles $T_e(\rho)$ were obtained by averaging values of the HRTS diagnostic and the ECE diagnostic over at least 0.4 s. Ion temperature profiles $T_i(\rho)$ and the toroidal rotation profiles were obtained via charge exchange from neon and deuterium (D-α charge exchange). Impurity density profiles were assumed to be proportional to the electron density profile ($n_{imp} \propto n_e$) with 3% of beryllium and 0.2% of nickel in the plasma. The effective charge Z_{eff} of the plasma was calculated according to the definition (8.4), taking into account all ion species considered in the simulation (thermal ions and fast ions).

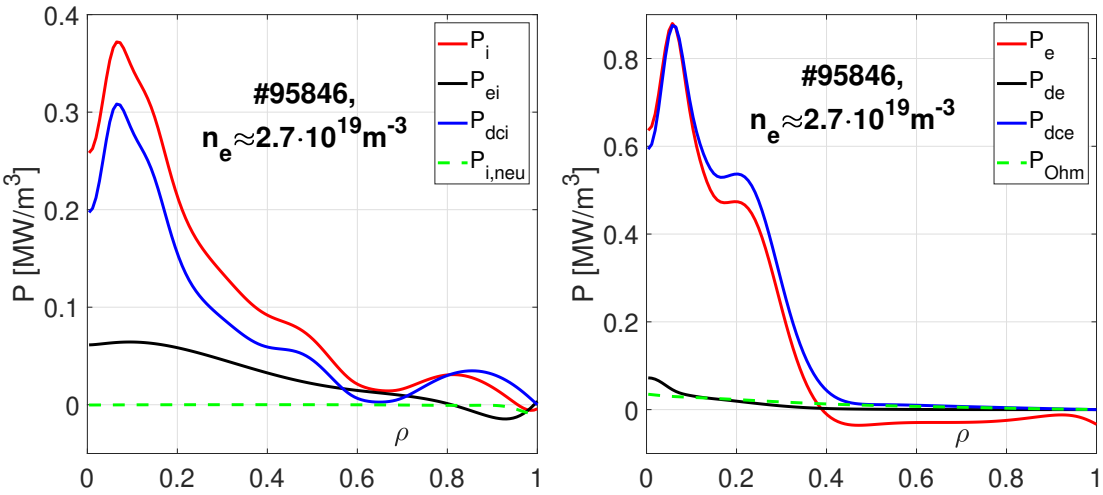

Figure 8.6: Left: Profile for total ion heating power P_i together with its contributions. Right: Profile for the total electron heating P_e together with the three most important contributions.

The model file used for power balance simulations of ICRH-heated JET plasmas can be found in appendix B. In contrast to ECRH heating, ICRH heating does not exclusively heat the electrons. Instead, the injected ICRH power P_{ICRH} can be divided into three components: direct electron heating P_{de}, collisional energy transfer from the fast ion population to electrons P_{dce} and collisional energy transfer from the fast ion population to all (thermal) ions P_{dci}. The power deposition profiles and the

density profile of fast ions $n_{\mathrm{fast}}(\rho)$ were determined with PION, a code that allows to determine power deposition and non-Maxwellian velocity distribution of ICRH-heated plasmas self-consistently. [14] In total, the power deposited to electrons and ions was determined by

$$P_e = P_{\mathrm{Ohm}} + P_{de} + P_{dce} - P_{\mathrm{rad}} - P_{e,neu} - P_{ei}, \tag{8.6}$$

$$P_i = P_{dci} + P_{i,neu} + P_{ei}. \tag{8.7}$$

Further contributions to P_e and P_i, taken into account in these equations are the collisional electron-ion heat transfer P_{ei}, the radiated power P_{rad} determined from bolometry measurements, Ohmic heating power P_{Ohm} and rather small heat sources and sinks $P_{i,neu}$ and $P_{e,neu}$ from cold neutrals ionization and charge exchange, implemented in the ASTRA expressions `PINEU` and `PENEU`.

The database contains two JET plasmas that are heated rather close to the magnetic axis and two plasmas that are heated rather off-axis. Figure 8.6 shows the electron and ion heating profiles of a plasma that is heated rather on-axis. This results from the fast ion population of this plasma being concentrated strongly in the centre of the plasma which leads to strong collisional energy transfers P_{dce} and P_{dci} close to the magnetic axis. The direct electron heating P_{de} is focused directly at the magnetic axis for all shots in the database, even when P_{dci} and P_{dce} are strongest around mid-radius.

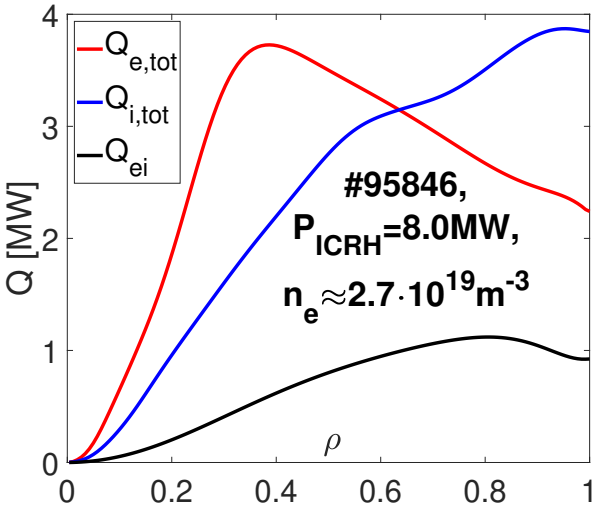

Figure 8.7: Radial profiles of electron heat flux $Q_{e,tot}$, ion heat flux $Q_{i,tot}$ and electron-ion heat transfer Q_{ei}.

Figure 8.7 shows the heat flux profiles $Q_{i,tot}$ and $Q_{e,tot}$ corresponding to the power deposition profiles in figure 8.6 together with Q_{ei}, being defined as the volume integral over the electron-ion energy transfer

$$Q_{ei} := \int_V P_{ei}\,\mathrm{d}V. \tag{8.8}$$

As one can see in figure 8.7, Q_{ei} is less than half as large as $Q_{i,tot}$ over the full radius of the plasma and the major contribution to the ion heat flux comes from P_{dci}. This makes the JET plasmas considered here less ITER-PFPO-1-specific than the purely ECRH-heated ASDEX Upgrade plasmas in the database (except if there is an upgrade making $10\ \mathrm{MW}$ of ICRH power available already in PFPO-1).
Since all JET plasmas in the database were performed at the same magnetic field of $B_T = 3.26\ \mathrm{T}$ and almost the same density of $\overline{n}_e \approx 2.7 \cdot 10^{10}\mathrm{m}^{-3}$, a common threshold edge ion heat flux of $Q^{LH}_{i,edge} \approx 1.8\ \mathrm{MW}$ can be determined for these shots. In figure 8.8, the experimental edge ion heat fluxes $Q_{i,tot}(\rho = 0.95)$ are compared with this threshold $Q^{LH}_{i,edge}$. One observes that the electron-ion heat exchange Q_{ei} contributes significantly less to $Q_{i,edge}$ than Q_{dci}. According to the threshold scaling $Q^{LH}_{i,edge}$, the collisional ion heating from fast particles Q_{dci} alone would be sufficient to reach H-mode.

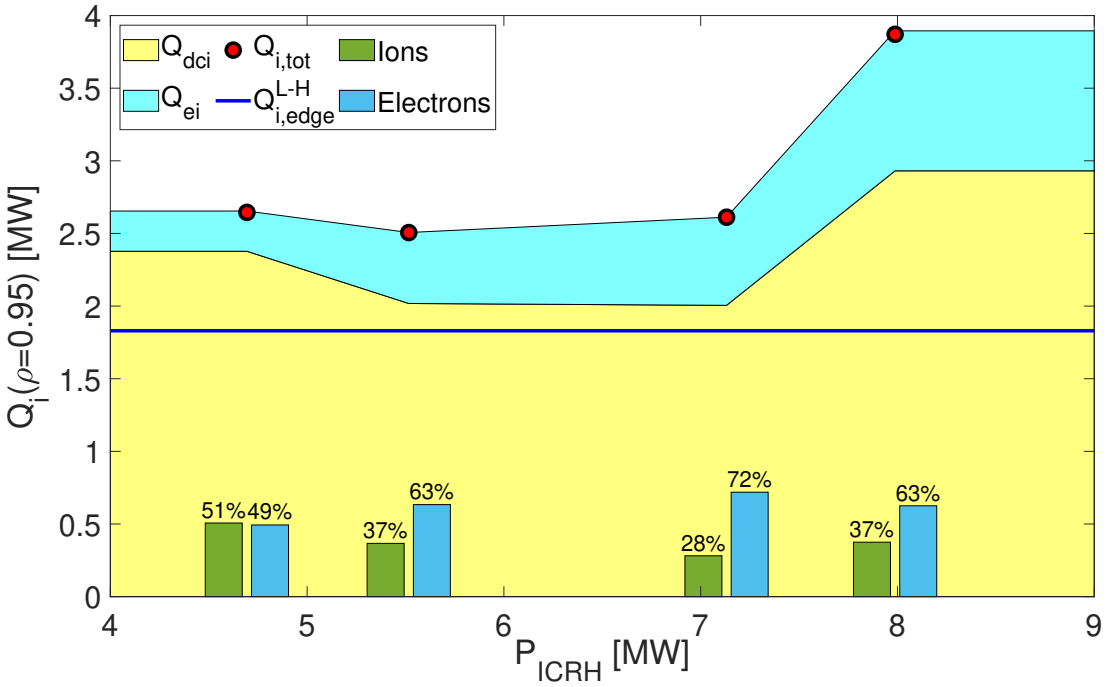

Figure 8.8: Comparison of the experimental edge ion heat fluxes with the threshold value $Q^{LH}_{i,edge}$. The coloured areas show the contributions to the edge ion heat flux from electron-ion heat exchange Q_{ei} and from direct ICRH-heating of ions Q_{dci}. The bars at the bottom of the graph show the fractions of the total ICRH power deposited to the electron heat channel $(Q_{dce} + Q_{de})/P_{ICRH}$ and to the ion heat channel Q_{dci}/P_{ICRH}.

Furthermore, one observes that $Q_{i,edge}$ is not a monotonically increasing function of P_{ICRH}. This is a result of the fact that the ICRH heating power is split up into a contribution heating the electrons ($P_{de} + P_{dce}$) and a contribution heating the ions (P_{dci}). It is not only the sum of these contributions, but also their ratio that affects $Q_{i,edge}$. Larger fractions Q_{dci}/P_{ICRH} deposited to the ion heat channel lead to higher $Q_{i,edge}$, as can be understood from the bar plots at the bottom of figure 8.8. Moreover, the radial position of ICRH power deposition, i.e. on-axis or off-axis resonances, might have an effect on $Q_{i,edge}$, too, since it affects the temperature profiles $T_e(\rho)$ and $T_i(\rho)$ and hence Q_{ei}.

9 TGLF simulations

9.1 ECRH-heated ASDEX Upgrade plasmas

9.1.1 Modelling setup

All simulations with TGLF were performed as close as possible to the conditions present in the power balance (PB) simulations (see section 8.1). Initial conditions and boundary conditions for T_e, T_i and n_e made use of the same experimental profiles that have been used in the PB simulations. The same holds for the profiles of toroidal rotation and effective charge Z_{eff}.

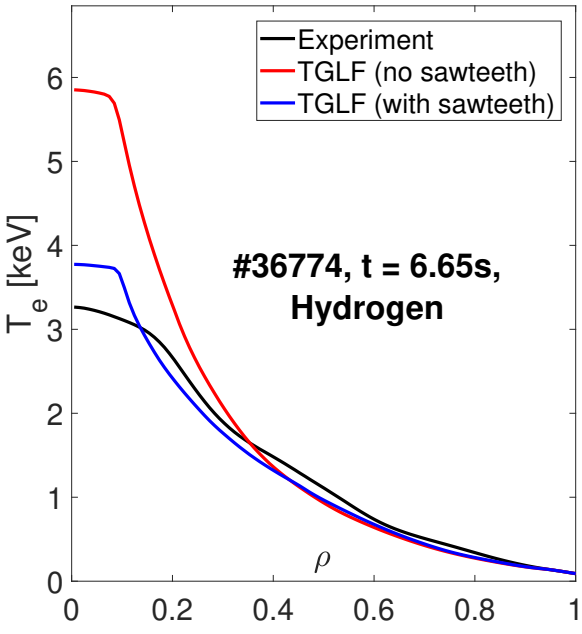

Figure 9.1: TGLF simulations with sawteeth acting on the current profile versus TGLF simulations without sawteeth acting on the q-profile.

In contrast to the PB simulations, the profiles for T_e, T_i and n_e were not prescribed, but evolving according to the transport equations (4.2) with a time step of $\tau = 0.025$ s. A set of reference simulations was performed with fixed n_e-profile.

The electron and ion energy sources P_e and P_i were calculated as in the PB simulations according to equations (8.2) and (8.3). Particle sources S_e that have been taken into account are cold gas puff neutrals and neutrals from NBI blips. The profiles of

cold neutrals were determined with the ASTRA-internal subroutine `NEUT` whereas the profiles of neutral particles from NBI were determined with RABBIT. [71]
Sawtooth instabilities, periodic bursts of particles heat and current out of the centre of the plasma, can occur when the safety factor q drops below 1. [55] The current redistribution by sawteeth was modeled by including the ASTRA-internal subroutine `MIXINT` [44] (modified to act only on the current profile) which is based on the Kadomtsev relaxation model [31]. A sawtooth period of $\tau_{\mathrm{saw}} = 0.05\ \mathrm{s}$ was assumed which is of the order of the experimentally observed sawtooth periods for the considered shots. Additionally, central (electron and ion) heat and particle conductivities were increased to model the average effect of energy and particle redistribution. Due to the temperature dependence of the Spitzer conductivity, $\sigma \propto T_e^{3/2}$, even just neglecting the redistribution of current would lead to significant errors in the predicted T_e-profiles as it is shown in figure 9.1.
Conductivities for heat were determined as the sum of a neo-classical part χ_{neo} determined with NCLASS [27], an effective turbulent conductivity χ_{turb} determined with TGLF and an artificial increase χ_{saw} in the centre to model an average sawtooth effect:

$$\chi = \chi_{\mathrm{neo}} + \chi_{\mathrm{turb}} + \chi_{\mathrm{saw}}. \tag{9.1}$$

The particle convection C_n was determined as the sum of a neo-classical contribution from the Ware pinch [69, 1] and the turbulent particle convection as determined with TGLF. In total, 16 processors were dedicated to TGLF calculations. Unless stated otherwise, all simulations in this section were performed with TGLF-Feb20.

9.1.2 Simulations with boundary $\rho_B = 0.82$

TGLF does not reproduce the edge transport barrier (ETB) that is present in H-modes. [32] To avoid systematic underprediction of temperature profiles in H-mode plasmas, especially close to the edge of the plasma, the boundary condition can be put at the pedestal top. Furthermore, previous versions of TGLF (SAT0 and SAT1-Aug19) are known to suffer from a shortfall in predicted energy transport for $\rho \gtrsim 0.8$ in L-mode plasmas. [63] A first set of simulations was therefore performed with a boundary condition at $\rho_B = 0.82$.

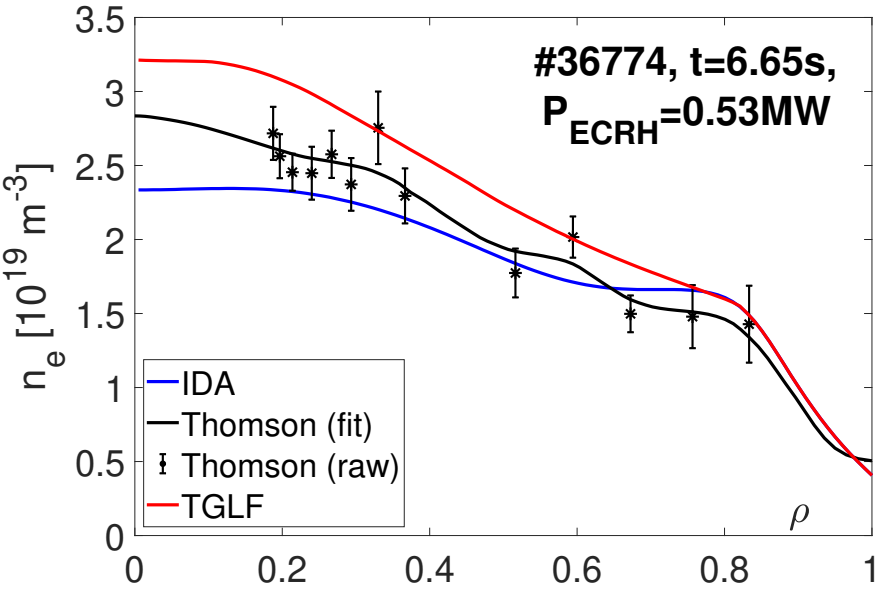

Figure 9.2: Density profile obtained from TGLF-Feb20 simulations versus experimental profiles from IDA and Thomson scattering for a hydrogen L-mode plasma.

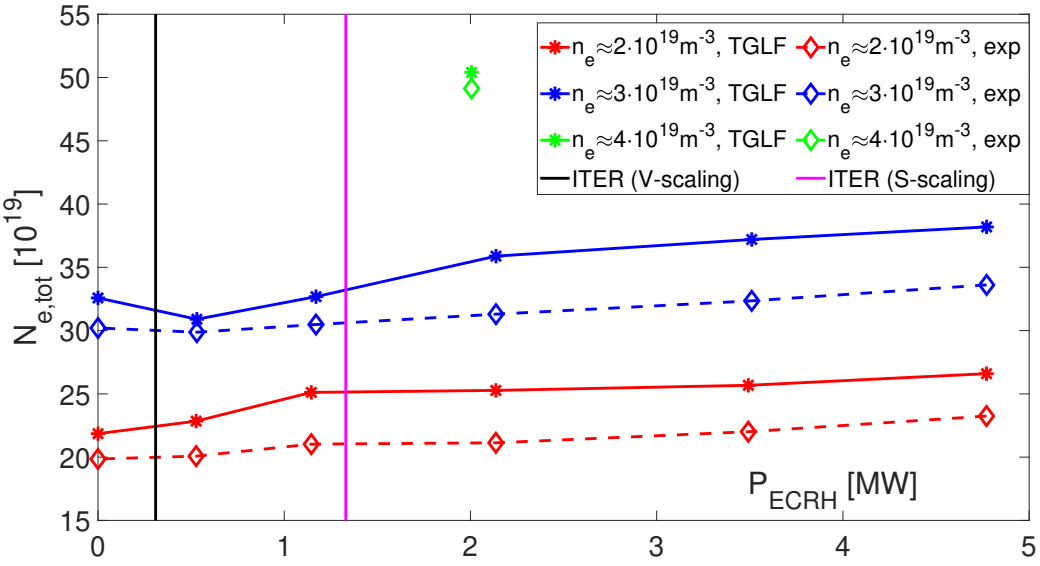

Figure 9.3: Comparison between experiment and TGLF-Feb20 simulations with respect to the total number of electrons in the plasma. The results for hydrogen plasmas at three different density levels are shown.

Figure 9.2 compares the n_e-profile of a hydrogen plasma as obtained with ASTRA-TGLF with the IDA profile, that was taken as initial and boundary condition, and with raw and fitted Thomson scattering data (adjusted to match the total particle number of the plasma). One observes that the simulated profile is significantly more peaked than the IDA profile. This significantly steeper slope was observed for all H datapoints and leads to a systematic overprediction of the total number of particles in the plasma (see figure 9.3). Similar observations were made for all deuterium datapoints at $q_{95} = 3.7$ and most (82%) of the D datapoints with $q_{95} \approx 5$. The deviation in the n_e-profile between ASTRA-TGLF and IDA is probably not exclusively a mistake of TGLF, but also a result of too flat IDA profiles. For low-density plasmas, the signal recorded by the DCN-H5 interferometry diagnostic is very low such that already small error signals from the scrape-off layer (SOL) can lead to significant overestimations of n_e close to the edge. [18] However, it should be pointed out that the slope of the predicted density profile coincides very well with the slope of the n_e-profile obtained from Thomson scattering (see figure 9.2).
As pointed out in section 5.4, the physical quantity which is considered to play a critical role for transitions from L-mode to H-mode is the edge ion heat flux $Q_{i,edge}$. Due to the heavy overestimation of the total particle number and the strong dependence of the electron-ion heat exchange on the density ($P_{ei} \propto n_e^2$), edge ion heat fluxes are systematically overestimated in simulations with $\rho_B = 0.82$ with an absolute relative deviation of $|Q_{i,edge}(\mathrm{TGLF}) - Q_{i,edge}(\mathrm{PB})|/Q_{i,edge}(\mathrm{PB}) = (+19 \pm 15)\%$. Improving the prediction quality of $Q_{i,edge}$ requires improving the density profile predictions which is subject of the next section.

9.1.3 Simulations with boundary $\rho_B = 0.95$

There is a large interest among the scientific community to push the boundary as close as possible to the separatrix. [32, 63] A second set of simulations was therefore performed with the boundary condition at $\rho_B = 0.95$, the position at which the edge ion heat flux is evaluated. [58] In these simulations, the source of cold gas puff neutrals was adjusted for $\rho \geq 0.61$ such that the total number of particles in experiment and simulation coincide within deviations of less than $< 4\%$ (see figure 9.4). This approach represents the ability of a real tokamak to control the density by adjusting the gas fuelling. The source of NBI neutrals was determined with RABBIT as in simulations with $\rho_B = 0.82$.

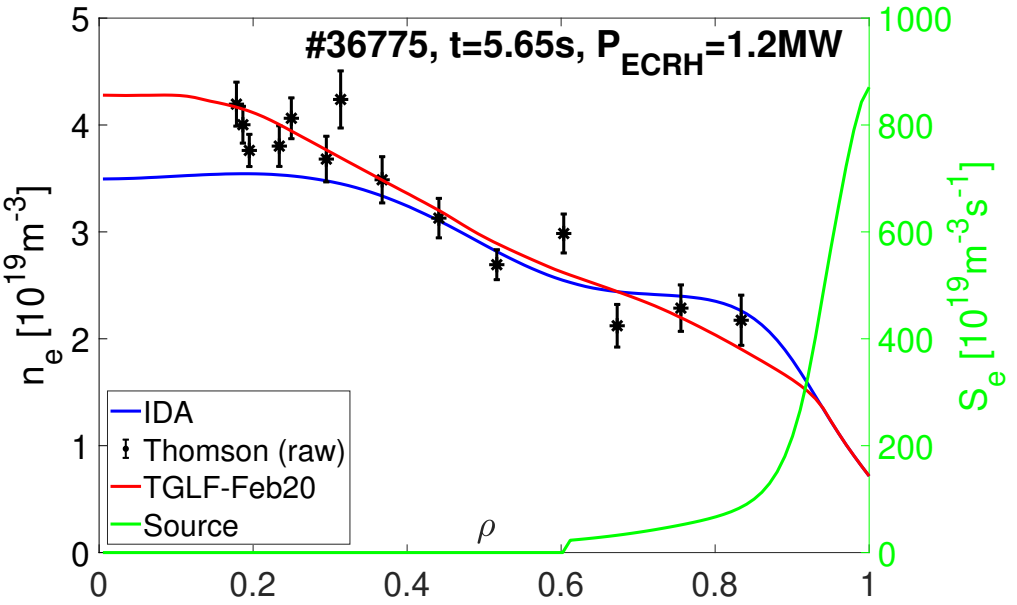

Figure 9.4: Predicted density profile for a very ITER-like hydrogen plasma ($P_{ECRH} = 1.2$ MW) together with the adjusted particle source S_e.

A test has been performed to move the boundary even closer to the separatrix than $\rho_B = 0.95$ for a hydrogen plasma with an ITER-like heating power of $P_{ECRH} = 1.1$ MW (see figure 9.5). For the central density $n_e(\rho = 0)$, only minor ($\leq 0.9\%$) deviations from simulations with $\rho_B = 0.95$ were found. As mentioned in section 3.1, the correct prediction of third harmonic ECRH absorption requires good predictions of central electron temperatures. The deviations for $T_e(\rho = 0)$ from simulations with $\rho_B = 0.95$ were below 3.5%.

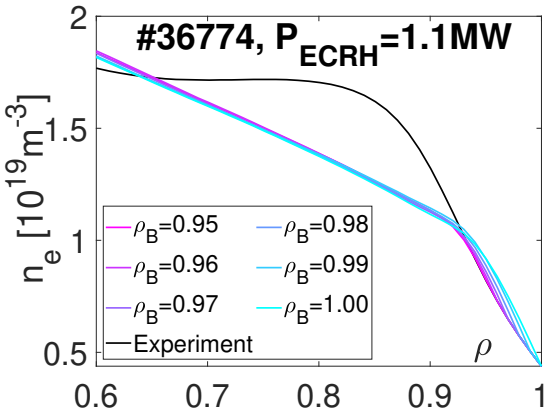

Figure 9.5: Predicted density profile for different positions of the boundary condition ρ_B.

In hydrogen simulations with $\rho_B = 0.95$, the predicted density profile coincides quite well with Thomson scattering measurements as the example in figure 9.4 shows. As a result of that, the predicted normalized logarithmic gradient (NLG) of the density R/L_{ne} was generally close to its experimental value (see figure 9.6). The negative slope of R/L_{ne} as a function of P_{ECRH} is correctly reproduced by TGLF-Feb20. Also for deuterium L-mode plasmas, the predicted R/L_{ne} coincides approximately with the experimental values within the uncertainties of Thomson scattering. For D, no significant difference in R/L_{ne} between $q_{95} \approx 5$-plasmas and $q_{95} = 3.7$-plasmas could be detected either in experiment or simulation.

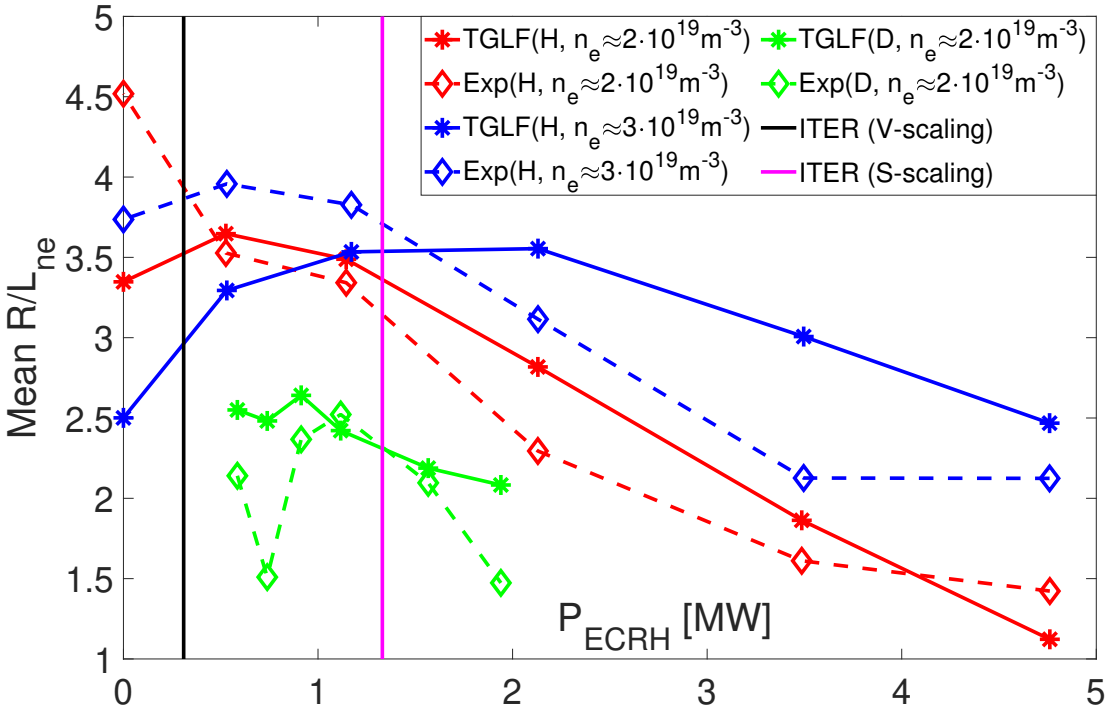

Figure 9.6: Normalized logarithmic gradients obtained from TGLF and Thomson scattering for hydrogen plasmas at two different density levels and deuterium plasmas at $\overline{n}_e \approx 2 \cdot 10^{19}\mathrm{m}^{-3}$ and $q_{95} = 3.7$. Only L-mode plasmas are shown in this plot. The NLGs were averaged over the ρ-interval of $[0.37; 0.63]$.

However, in spite of strong fluctuations of Thomson scattering data, one observes clearly that the experimental R/L_{ne} for a H plasma is significantly higher than for a D plasma at the same density. This coincides with analytical results and numerical results from gyrokinetic simulations presented in [2]. It can be explained by the

increase in the collisional contribution to outward convective particle transport by trapped electrons with increasing ion mass m_i. Additionally, the collisionless inward convection by the curvature pinch is reduced with increasing ion mass m_i. Both leads to reduced net inward turbulent convection of particles, and thus reduced R/L_{ne}, with increasing ion mass m_i. As figure 9.6 shows for the example of plasmas at $\overline{n}_e \approx 2 \cdot 10^{19}\mathrm{m}^{-3}$, this mass effect is correctly captured by TGLF within the experimental uncertainties.

9.1.4 H-mode versus L-mode

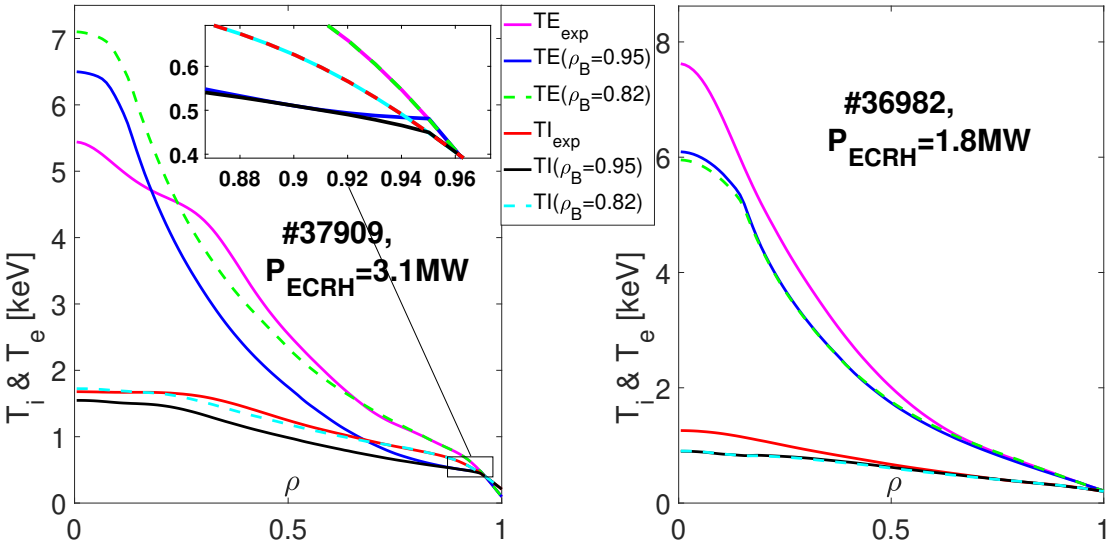

Figure 9.7: Experimental and predicted temperature profiles for a deuterium H-mode plasma with (left) and for a deuterium L-mode plasma (right). Simulations with boundary $\rho_B = 0.82$ and boundary $\rho_B = 0.95$ are shown.

As its predecessor GLF23, the trapped gyro-Landau fluid model (TGLF) does not take into account the edge transport barrier (ETB). [32] It was shown in [32] and can be seen in figure 9.7 (left), that the steep T_e-profile close to the edge of an H-mode plasma is not reproduced correctly. As we can see in figure 9.7 (left), ASTRA-TGLF fails to predict the ETB for the ion temperature, too. This motivates to take the pedestal top as boundary condition in H-mode simulations as it was done in simulations with $\rho_B = 0.82$.

Simulations with the boundary condition in the ETB region at $\rho_B = 0.95$ result in significantly lower predicted temperature profiles than with $\rho_B = 0.82$ not only close to the edge, but over the full radius $\rho \leq \rho_B$. This can be explained by the stiffness of turbulent transport that is reproduced by gyro-Landau fluid models such as TGLF [33], i.e. a shift of the T-profiles at the boundary translates into a comparable shift at all positions $\rho < \rho_B$, especially at the magnetic axis ($\rho = 0$). In [33], stiffness was found for ion temperature as well as for electron temperature profiles.
The missing ETB together with the stiffness explains why in simulations with $\rho_B = 0.82$ and $\rho_B = 0.95$, the shape of the temperature profiles is almost the same, but they are shifted with respect to each other. For studies in the framework of this master thesis, this is not a major problem since the focus is on the prediction of $Q_{i,edge}$ in L-mode plasmas.
It is worth noting that in L-mode plasmas, only minor differences were observed in the temperature profiles between simulations with $\rho_B = 0.82$ and $\rho_B = 0.95$ (see figure 9.7, right) despite the significantly different n_e-profiles. Average relative deviations were only about 2.5% for $T_e(\rho = 0)$ and about 6% for $T_i(\rho = 0)$. This is a useful observation since it allows statistical analysis to be done with simulations with $\rho_B = 0.82$ were large amount of data points, i.e. also H-mode plasmas, are needed.

9.1.5 Different versions of TGLF

The focus of this thesis was to validate the newest official version of TGLF-SAT1 (February 2020) which takes into account poloidal dependencies of the potential saturation amplitude and which was calibrated on CGYRO. In this section, this version of TGLF is compared with its beta version (December 2019) and with the TGLF-SAT1 version of August 2019.
Previous versions of TGLF and GLF23 were known to heavily underestimate the edge transport in L-mode plasmas, especially at low plasma current (high safety factor q) [16, 63]. In [63], it was shown that early versions of TGLF-SAT1 predict edge turbulent transport in L-mode plasmas significantly better than TGLF-SAT0, but still underestimate the edge heat flux. In a validation against DIII-D data, it was demonstrated that errors due to edge transport underprediction increase with decreasing plasma current I_p and decreasing collisionality ν^*. The cyan lines in

figures 9.8 and 9.9 demonstrate the underestimation of edge turbulent transport by the TGLF-SAT1 version of August 2019 at an example plasma at rather high ECRH power of $2.1\ \mathrm{MW}$ (and therefore low collisionality because of $\nu^* \propto T_e^{-2}$). There is a considerable pedestal-like feature in the electron and ion temperature profiles that pushes upwards the whole profiles.

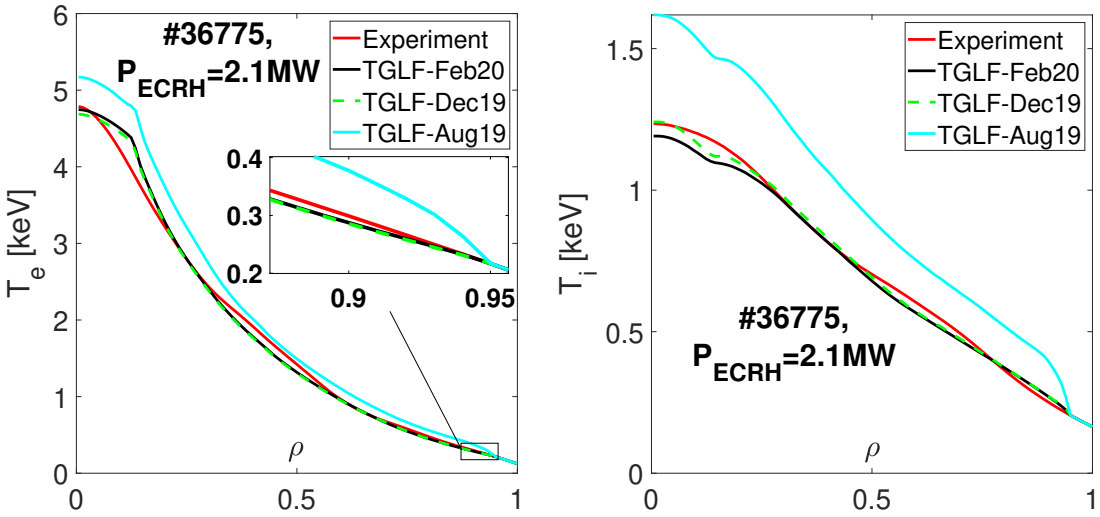

Figure 9.8: Experimental electron (left) and ion (right) temperature profiles are compared with the predicted profiles of three different versions of the trapped gyro-Landau fluid (TGLF) model.

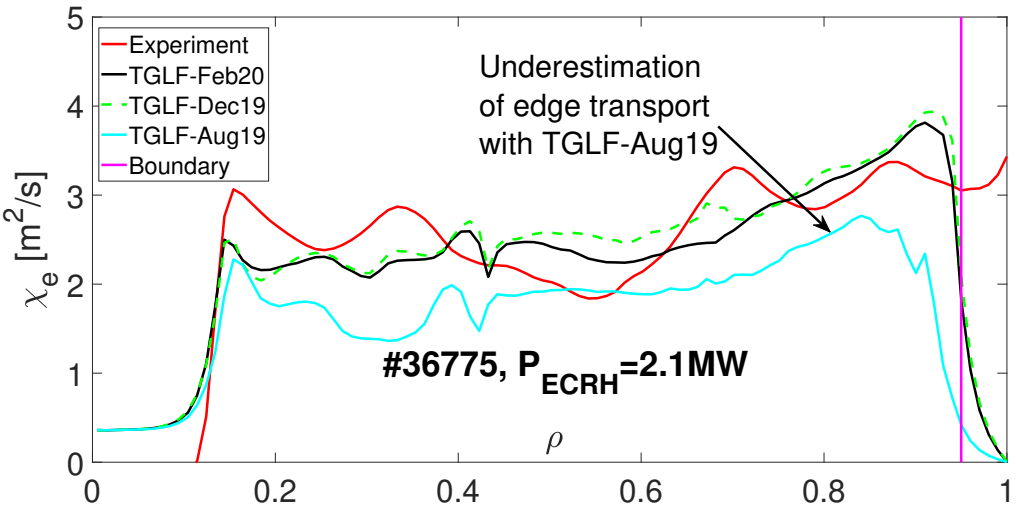

Figure 9.9: Experimental electron heat conductivity is compared with the predicted effective heat conductivities of three different versions of TGLF. See figure 9.8 (left) for the corresponding T_e-profile.

It is clearly visible in figure 9.9 that the edge electron heat conductivity χ_e is significantly better predicted with TGLF-Feb20 than with TGLF-Aug19. The same was observed for the edge ion heat conductivity χ_i. As a result, electron and ion temperature profiles predicted with TGLF-Feb20 do not show a pedestal-like feature close to the edge, but follow smoothly the experimental profile.
Between the two TGLF-SAT1 versions of December 2019 and February 2020, only minor differences were observed, as one can see in the example in figures 9.8 and 9.9. Since in the version of December 2019, a less sophisticated geometry factor is implemented, validation on plasmas with stronger shaping could reveal larger discrepancies between the latest two versions of TGLF-SAT1.

9.1.6 Electron temperature profiles

Electron temperature profiles close to the edge were evaluated in sections 9.1.4 and 9.1.5 and it was found that in case of L-mode plasmas, the predicted profiles follow very well the experimental profiles close to the edge. However, as it was shown in section 3.1, good prediction of third harmonic ECRH absorption in PFPO-1 especially requires well-predicted electron temperature profiles close to the centre of the plasma. The focus of this section will therefore be the prediction quality of T_e-profiles around mid-radius and close to the centre of the plasma.

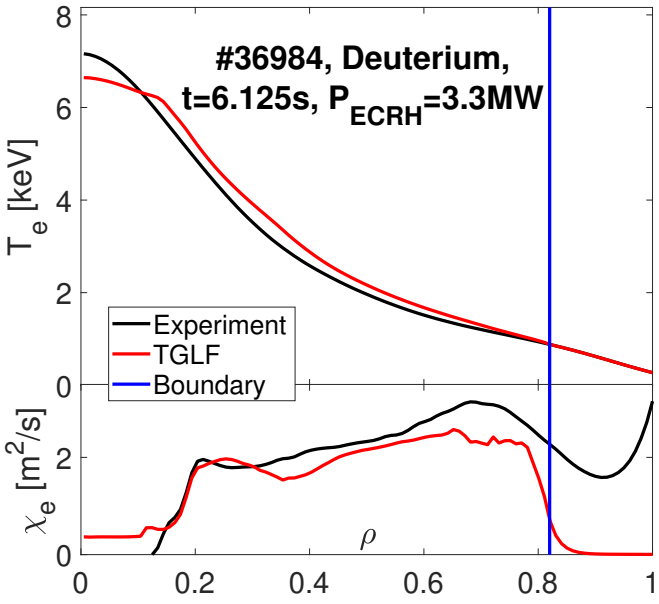

Figure 9.10: Experimental and predicted electron temperature profiles $T_e(\rho)$ and electron heat conductivities χ_e for a D plasma with $q_{95} \approx 5$.

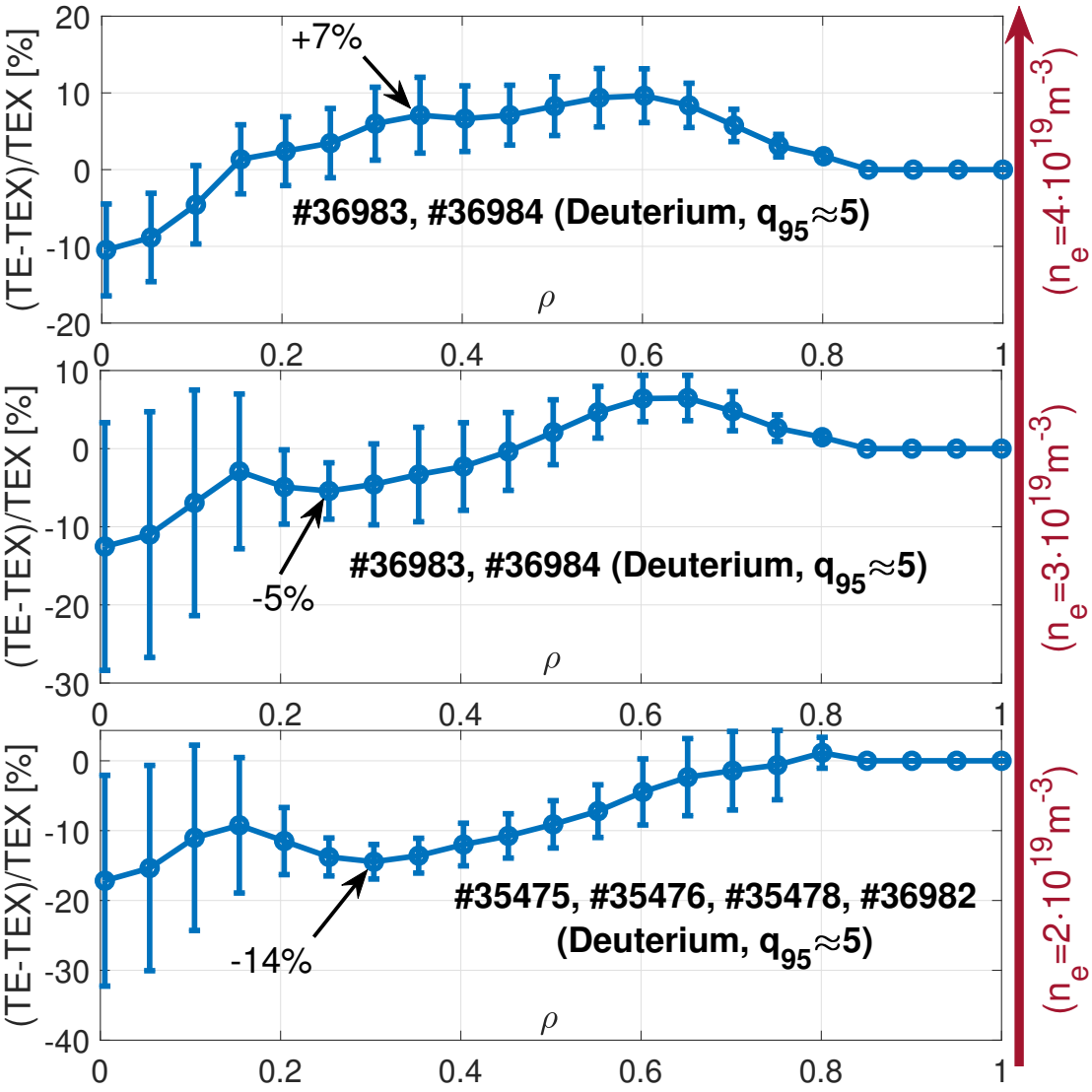

Figure 9.11: Average relative deviations of the predicted electron temperature TE (with boundary $\rho_B = 0.82$) from the experimental electron temperature TEX for deuterium plasmas at $q_{95} \approx 5$ and three different density levels.

To be able to take into account also H-mode plasmas, the following statistical analysis is based on simulations having the boundary at $\rho_B = 0.82$. For hydrogen plasmas at $q_{95} \approx 5$ which are all in L-mode, analogous results would be obtained also for $\rho_B = 0.95$. The three plots in figure 9.11 show the (average) relative deviations $(T_e(\mathrm{TGLF}) - T_e(\mathrm{Exp}))/T_e(\mathrm{Exp})$ of the predicted electron temperature profile $T_e(\mathrm{TGLF})$ from the experimental electron temperature profile $T_e(\mathrm{Exp})$ for deu-

terium plasmas at $q_{95} \approx 5$ and at three different density levels. The error bars depict the empirical standard deviation among one set of data points with approximately the same line-averaged density $\overline{n}_e$ and the same edge safety factor q_{95}.
In general, for all density levels, the relative deviation is exactly zero for all radial positions with $\rho > 0.82$ since these points are fixed in the simulation by the boundary condition. For the plasmas at $\overline{n}_e \approx 2 \cdot 10^{19}\mathrm{m}^{-3}$ shown at the bottom of figure 9.11, one observes very good predictions of the electron temperature close to the edge. For $\rho \in [0.6; 0.8]$, the zero is always within the error bars.
Towards smaller ρ, one observes that the predicted electron temperature then drops significantly below the experimental electron temperature TEX. There is a local minimum around $\rho = 0.3$ with an average relative deviation of -14%. A very representative example for such a D plasma at $q_{95} \approx 5$ and $\overline{n}_e \approx 2 \cdot 10^{19}\mathrm{m}^{-3}$ is shown on the right-hand side of figure 9.7. The reason for the considerable underestimation of T_e around mid-radius in these plasmas is the overprediction of the electron heat transport for $\rho \in [0.3; 0.7]$. At $\overline{n}_e \approx 3 \cdot 10^{19}\mathrm{m}^{-3}$, electron temperature predictions are closer to the experimental profiles and the local minimum corresponds to an average relative deviation -5%. For $\overline{n}_e \approx 4 \cdot 10^{19}\mathrm{m}^{-3}$, electron temperatures are overestimated by ASTRA-TGLF over a large part of the radius and there is a local maximum with an average relative deviation of $+7\%$. Figure 9.10 shows a typical example of such a D plasma at $q_{95} \approx 5$ and $\overline{n}_e \approx 4 \cdot 10^{19}\mathrm{m}^{-3}$.
As one can see from figure 9.11, it depends on the density whether, and how much, electron energy transport is under- or overestimated by TGLF-Feb20. The same density dependence was also found for deuterium plasmas at $q_{95} = 3.7$ with minimum relative deviations of -20% at $\overline{n}_e \approx 2 \cdot 10^{19}\mathrm{m}^{-3}$, -8% at $\overline{n}_e \approx 3 \cdot 10^{19}\mathrm{m}^{-3}$ and -4% at $\overline{n}_e \approx 4 \cdot 10^{19}\mathrm{m}^{-3}$. Also hydrogen plasmas show the same density dependence with a minimum/maximum relative deviation of -11% at $\overline{n}_e \approx 2 \cdot 10^{19}\mathrm{m}^{-3}$, -7% at $\overline{n}_e \approx 3 \cdot 10^{19}\mathrm{m}^{-3}$ and $+9\%$ at $\overline{n}_e \approx 4 \cdot 10^{19}\mathrm{m}^{-3}$.
The density dependence of $(T_e(\mathrm{TGLF}) - T_e(\mathrm{Exp}))/T_e(\mathrm{Exp})$ can also be interpreted as a collisionality dependence since $\nu^* \propto n_e$. For GLF23, such a collisionality dependence with underestimation of T_e at low ν^* and overestimation of T_e at high ν^* was already demonstrated in [32]. It was also shown in [32] that this collisionality dependence is weaker in TGLF-SAT0 than in GLF23 due to a more sophisticated model of trapped particles in TGLF. As the analysis in this section shows, there is still a significant collisionality dependence in the electron heat channel present in TGLF-SAT1 (February 2020).

Figure 9.12 shows the electron temperature T_e as a function of P_{ECRH} for two hydrogen discharges that remained in L-mode in all ECRH power levels. The predicted profiles are from simulations with boundary $\rho_B = 0.95$. Curves for $T_e(P_{ECRH})$ are shown for three different radial positions.

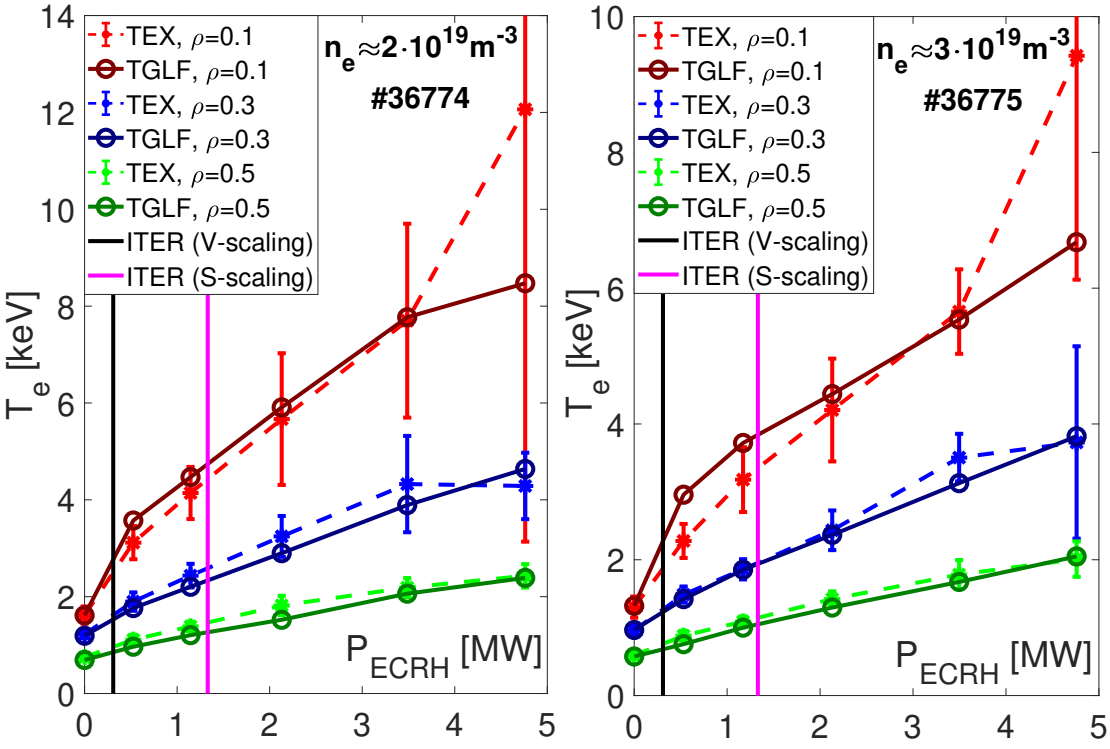

Figure 9.12: Experimental and predicted electron temperatures for two H discharges as a function of the coupled ECRH power. The electron temperatures of three different radial positions are shown.

For $\rho = 0.3$ and $\rho = 0.5$, one recovers what was already mentioned in this section: T_e tends to be underestimated for hydrogen plasmas with $\overline{n}_e \lesssim 3 \cdot 10^{19}\mathrm{m}^{-3}$. For $\overline{n}_e \approx 2 \cdot 10^{19}\mathrm{m}^{-3}$, stronger underestimation is found than for $\overline{n}_e \approx 3 \cdot 10^{19}\mathrm{m}^{-3}$. Nevertheless, for both density levels, the monotonically increasing behaviour of T_e as a function of P_{ECRH} is quite well predicted.

For $\rho = 0.1$, one observes larger deviations. This could be the result of a too simplified treatment of sawtooth instabilities. Furthermore, the measured central electron temperatures heavily shoot up for $P_{ECRH} = 4.8$ MW. This is the result of particles becoming superthermal at such high ECRH powers and can therefore not be expected to be reproduced with ASTRA-TGLF. Therefore, $T_e(\rho = 0.2)$ is

considered here to assess the prediction quality of central electron temperatures to avoid results that are influenced by superthermal particles or the model of sawtooth instabilities.
Table 9.1 contains the relative deviations $(T_e(\mathrm{TGLF}) - T_e(\mathrm{Exp}))/T_e(\mathrm{Exp})$ at $\rho = 0.2$. On average, the predictions for $T_e(\rho = 0.2)$ are very good with a mean relative deviation of 0% over the full database and a mean relative deviation of -3% for ITER-like heated plasmas. As figure 9.12 shows, many predictions of central electron temperatures are even within the intervals of experimental uncertainty. This shows that on average, TGLF provides appropriate central electron temperature predictions to be applied to the calculation of third harmonic (X3) ECRH absorption in centrally heated ITER-PFPO-1 plasmas.

Table 9.1: Average relative deviations $\pm$ standard deviations of the central electron temperatures $T_e(\rho = 0.2)$. Results are shown by taking the average over all plasmas and by taking only the most ITER-like plasmas.

	All plasmas	Plasmas with $P_{ECRH} \approx 1.3\ \mathrm{MW}$
H, $q_{95} \approx 5$	$(+2 \pm 8)\%$	$(+6 \pm 13)\%$
D, $q_{95} \approx 5$	$(-10 \pm 6)\%$	$(-11 \pm 3)\%$
D, $q_{95} \approx 3.7$	$(+9 \pm 18)\%$	$(+9 \pm 14)\%$
Full database	$(0 \pm 14)\%$	$(-3 \pm 13)\%$

9.1.7 Electron heat transport

According to the gyroBohm scaling (6.2), the electron heat conductivity would scale as $\chi_e \propto T_e^{3/2}$ with the electron temperature. To check for gyroBohm behaviour, the ratio $\chi_e/T_e^{3/2}$ is plotted in figure 9.13 for a set of L-mode discharges. Only L-mode discharges are shown to exclude effects on T_e based on a missing ETB-prediction by TGLF.
One observes that in experiment as well as in simulations, the ratio $\chi_e/T_e^{3/2}$ is approximately constant and independent of P_{ECRH} for all considered densities and isotopes. The same was found for plasmas at $q_{95} = 3.7$. This shows that plasmas in the experiment show approximately gyroBohm behaviour with respect to the electron temperature and that this gyroBohm behaviour can be reproduced by TGLF.

The gyroBohm scaling (6.2) further states that the ratio $\chi_e/T_e^{3/2}$ increases with the main ion mass m_i as $\chi_e/T_e^{3/2} \propto \sqrt{m_i}$. However, the discharges in figure 9.13 show that in fact, $\chi_e/T_e^{3/2}$ decreases with increasing main ion mass. In experiments at $\overline{n}_e \approx 2 \cdot 10^{19}\mathrm{m}^{-3}$, for example, one observes a mean value of $1.5\ \mathrm{m}^2\mathrm{s}^{-1}/(\mathrm{keV})^{3/2}$ for H, but only $1.1\ \mathrm{m}^2\mathrm{s}^{-1}/(\mathrm{keV})^{3/2}$ for D. Such an anti-gyroBohm scaling was also observed in discharges at higher density. It can be explained by the ion mass dependence of the collisional stabilization of trapped electron modes that will be discussed in detail in section 9.1.10. Whereas neither χ_B nor χ_{gB} decrease with increasing m_i, this anti-gyroBohm behaviour is correctly reproduced by TGLF as figure 9.13 demonstrates.

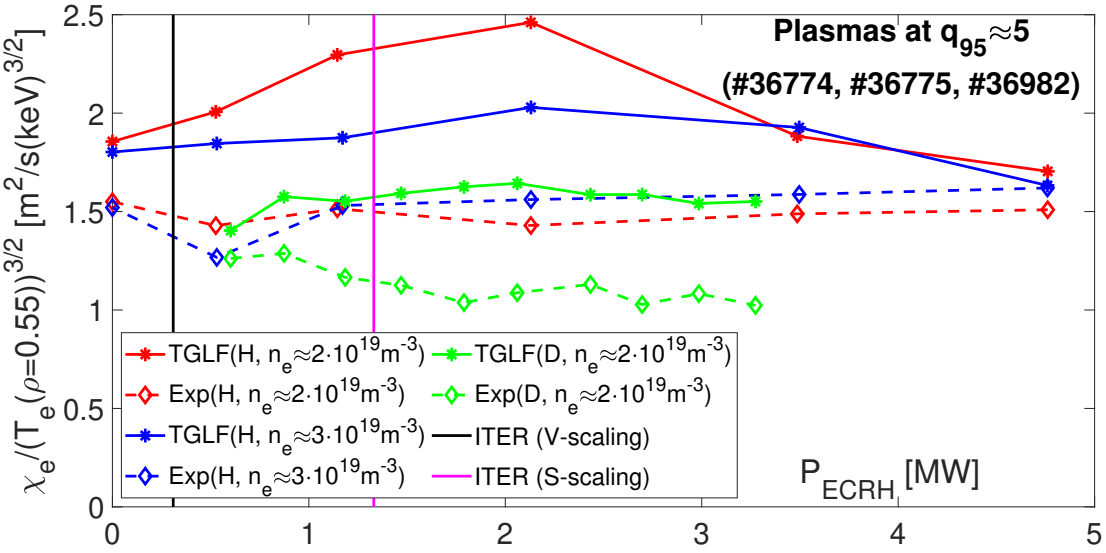

Figure 9.13: Electron heat conductivities χ_e averaged over the interval $[0.45; 0.65]$, divided by $(T_e(\rho = 0.55))^{3/2}$ to check for gyroBohm scaling. L-mode plasmas at $q_{95} \approx 5$ are shown. Simulations were performed with boundary $\rho_B = 0.95$.

Furthermore, neither χ_B nor χ_{gB} include any dependence on the plasma current I_p (or safety factor q_{95}). However, in the deuterium plasmas in the database, a significant decrease in $\chi_e/T_e^{3/2}$ is observed when the safety factor is lowered from $q_{95} \approx 5$ to $q_{95} = 3.7$, i.e. the confinement enhances with increasing plasma current I_p. This was consistently observed over all density levels. TGLF can correctly reproduce this I_p-dependence and produces lower $\chi_e/T_e^{3/2}$ at higher plasma current I_p.
Figure 9.14 shows the electron heat conductivity χ_e of two L-mode discharges as a

function of P_{ECRH}. A fitting function of the form

$$\chi_e = a \cdot (b + P_{ECRH})^c$$

with constants $a \geq 0$, $b \geq 0$ and $c \geq 0$ has been applied. The coefficient c can be estimated roughly based on the $\chi_e \propto T_e^{3/2}$-dependence of the heat conductivity. This electron temperature dependence approximately leads to $P_{ECRH} \approx Q_e \propto T_e^{5/2}$. Based on this very rough estimate yielding $T_e \propto (P_{ECRH})^{2/5}$, one expects $c \approx 0.6$. The constant b was included to take into account that electrons are also heated by Ohmic heating to a small extent. In L-mode plasmas, the fitted values for c are all in the interval $c \in [0.3; 0.9]$.

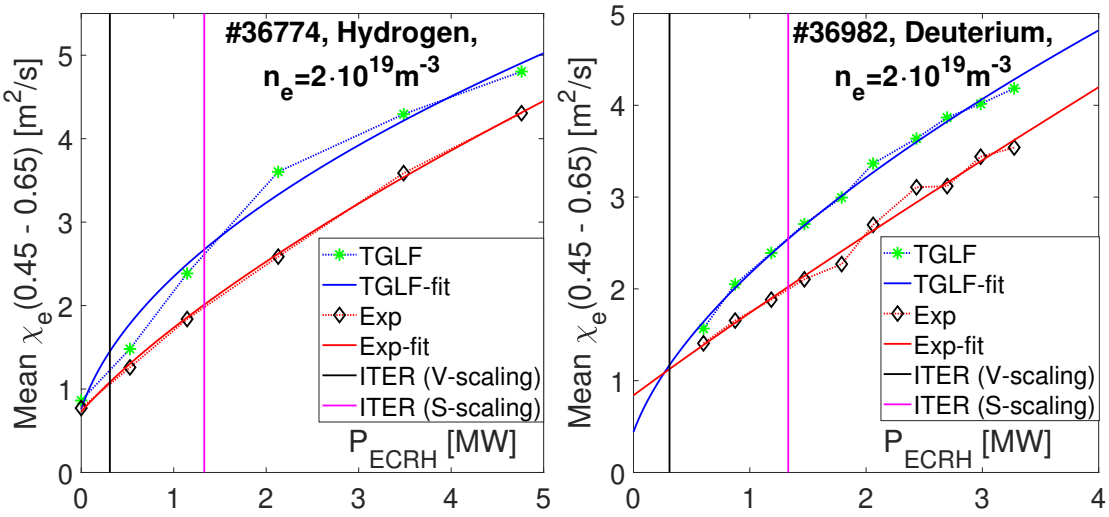

Figure 9.14: Electron heat conductivities χ_e (averaged over the interval $[0.45; 0.65]$) for a hydrogen discharge (left) and a deuterium discharge (right), both at $\overline{n}_e \approx 2 \cdot 10^{19}\mathrm{m}^{-3}$ and $q_{95} \approx 5$ and entirely in L-mode.

In figure 9.14, one observes that experimental and predicted electron heat conductivities χ_e are closer together at low ECRH powers and differ more from each other towards higher ECRH powers. This leads to good predictions of T_e especially in Ohmic plasmas, as figure 9.12 demonstrates. This is a valuable observation since especially at low P_{ECRH}/ low electron temperatures, X3 ECRH absorption is very sensitive on central electron temperatures (see figure 3.2). Good estimates for χ_e especially at low P_{ECRH} ensure good predictions of third harmonic ECRH absorption at low ECRH heating powers and in Ohmic plasmas.

9.1.8 Ion temperature profiles

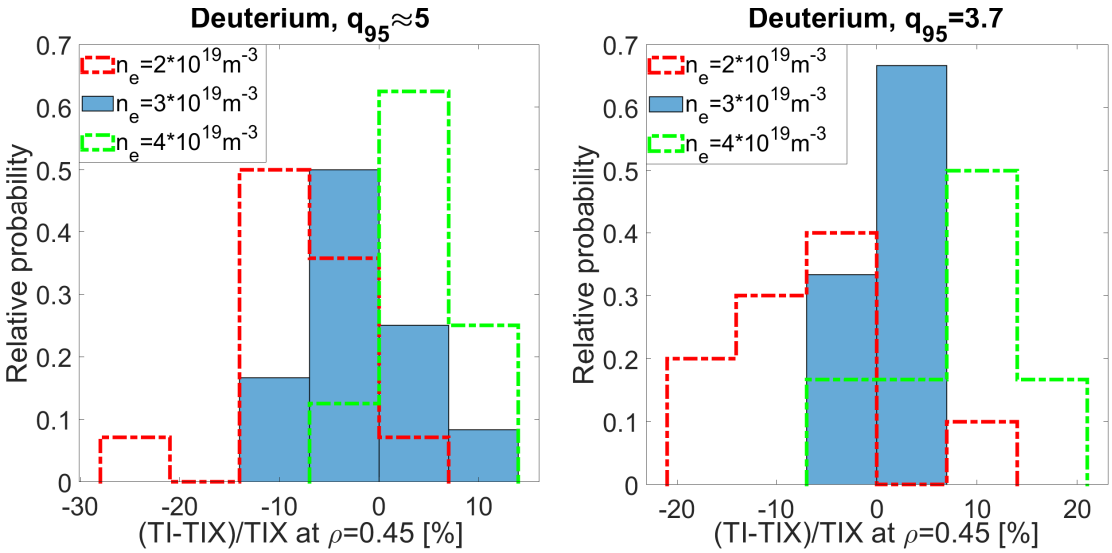

Figure 9.15: Histograms of the relative deviations of the predicted ion temperature TI (with boundary $\rho_B = 0.82$) from the experimental ion temperature TIX for deuterium plasmas at $q_{95} \approx 5$ (left) and $q_{95} = 3.7$ (right) for three different density levels.

TGLF-SAT0 is known to better reproduce ion temperature profiles than its predecessor GLF23 [32] and it has been shown in section 9.1.5 that TGLF-Feb20 further improves the prediction quality of T_i close to the edge. This section will focus on TGLF-Feb20 predictions around mid-radius and close to the magnetic axis. Like section 9.1.6, it starts with a statistical analysis for which all available data points were taken into account and therefore simulations with $\rho_B = 0.82$ are considered. Figure 9.15 (left) shows the relative deviations $(T_i(\mathrm{TGLF}) - T_i(\mathrm{Exp}))/T_i(\mathrm{Exp})$ between the experimentally measured ion temperature $T_i(\mathrm{Exp})$ and the predicted ion temperature $T_i(\mathrm{TGLF})$ at $\rho = 0.45$ for D plasmas at $q_{95} \approx 5$. At low density ($\overline{n}_e \approx 2 \cdot 10^{19}\mathrm{m}^{-3}$), the ion temperature tends to be underestimated by ASTRA-TGLF. One observes an average ($\pm$ standard deviation) relative deviation of $(-7 \pm 7)\%$. To determine the cause of this this underestimation, one has to consider that ion temperature profiles are determined by ion heat transport χ_i as well as electron-ion heat transfer (or ion heat flux Q_i). It can be shown that the dominant reason for the underestimation of $T_i(\rho = 0.45)$ is an overestimation of ion heat transport by TGLF for $\rho \gtrsim 0.5$.

At $\overline{n}_e \approx 3{\cdot}10^{19}\mathrm{m}^{-3}$, ion temperatures at $\rho = 0.45$ tend to be better predicted with relative deviations of only $(-2{\pm}7)\%$. This is the result of comparably better predictions of χ_i for $\rho \gtrsim 0.5$. For $\overline{n}_e \approx 4 \cdot 10^{19}\mathrm{m}^{-3}$, overpredictions for $T_i(\rho = 0.45)$ are observed with relative deviations from experimental T_i of $(+4 \pm 5)\%$. These overepredictions of $T_i(\rho = 0.45)$ are caused by an underestimation of the ion heat transport in the interval $\rho \in [0.5; 0.8]$ as the example in figure 9.16 demonstrates.

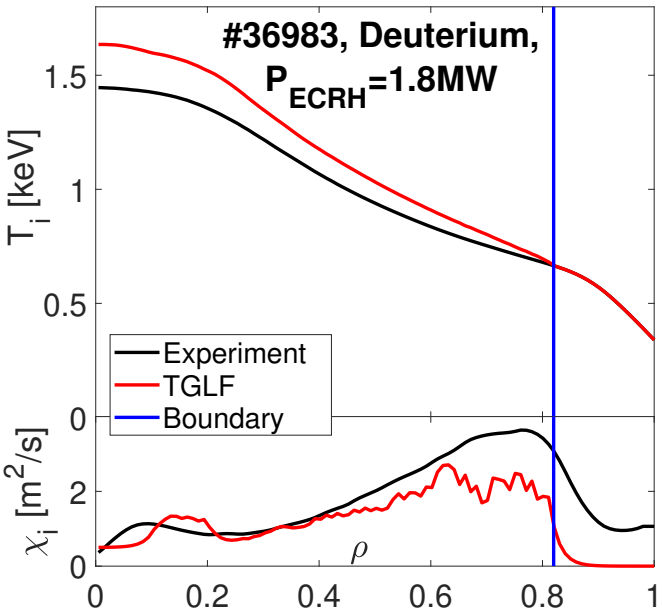

Figure 9.16: Experimental and predicted ion temperature profiles $T_i(\rho)$ and ion heat conductivities χ_i for a D plasma with $q_{95} \approx 5$ and $\overline{n}_e \approx 4 \cdot 10^{19}\mathrm{m}^{-3}$.

Similarly, one observes that the value for $(T_i(\mathrm{TGLF}) - T_i(\mathrm{Exp}))/T_i(\mathrm{Exp})$ increases with increasing line-averaged density $\overline{n}_e$ also in deuterium plasmas at $q_{95} = 3.7$ (see figure 9.15, right) and in hydrogen plasmas. As already outlined in section 9.1.6, such a dependence on the density can also be interpreted as a dependence on the collisionality $\nu^* \propto n_e$. Like for the electron energy transport, one observes a tendency of TGLF-Feb20 to overestimate ion energy transport at low collisionalities and underestimate the ion energy transport at higher collisionalities ν^*.

Figure 9.17 shows ion temperatures for two hydrogen discharges at different line-averaged density as a function of P_{ECRH}. For curves at $\overline{n}_e \approx 2 \cdot 10^{19}\mathrm{m}^{-3}$ (left), one recognizes the existence of a maximum in $T_i(P_{ECRH})$. Highest ion temperatures are achieved for ECRH heating powers between $0.5\ \mathrm{MW}$ and $1.5\ \mathrm{MW}$. The existence of such a maximum can be explained by the combined effect of an increasing ion heat transport χ_i with increasing P_{ECRH} and the monotonically increasing ion heat flux $Q_i(P_{ECRH})$ that reaches saturation at higher ECRH powers. As figure 9.17 (left) shows, ASTRA-TGLF is able to reproduce the existence of that maximum. At

$\overline{n}_e \approx 3 \cdot 10^{19}\mathrm{m}^{-3}$ (right), $T_i(P_{ECRH})$ increases over a wider range of ECRH powers since $Q_i(P_{ECRH})$ goes slower into saturation at higher density.

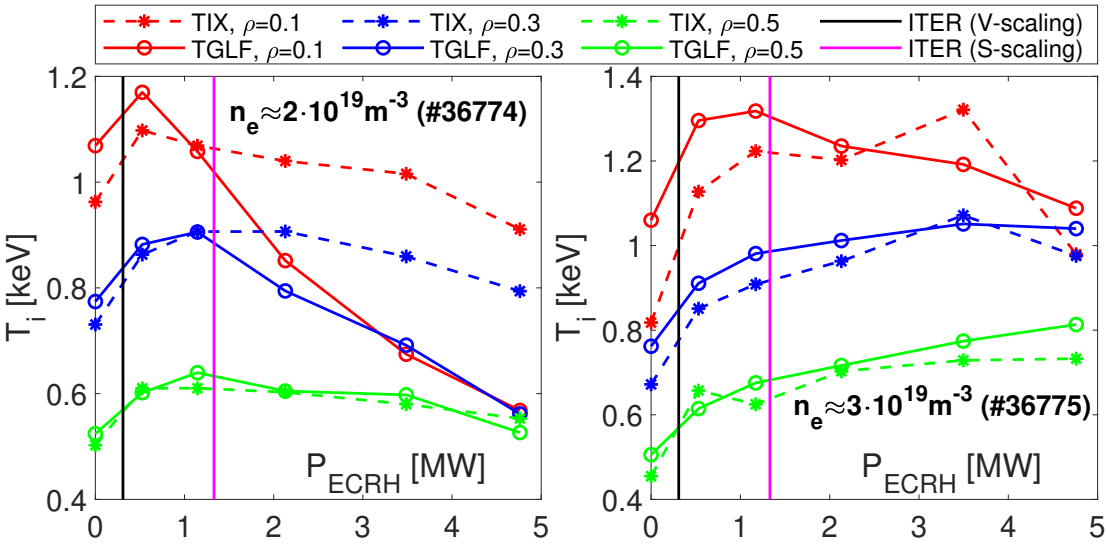

Figure 9.17: Experimental and predicted ion temperatures for two H discharges as a function of the coupled ECRH power. The ion temperatures of three different radial positions are shown. Simulations were performed with boundary at $\rho_B = 0.95$.

Around mid-radius ($\rho = 0.5$), the ion temperature is well-predicted by ASTRA-TGLF at both density levels. As already discussed, $T_i(\rho = 0.5)$ is slightly more overestimated in plasmas at $\overline{n}_e \approx 3 \cdot 10^{19}\mathrm{m}^{-3}$ than at $\overline{n}_e \approx 2 \cdot 10^{19}\mathrm{m}^{-3}$.
Closer to the magnetic axis ($\rho \leq 0.3$), the ion temperature is still well-estimated for plasmas at $\overline{n}_e \approx 3 \cdot 10^{19}\mathrm{m}^{-3}$. However, at $\overline{n}_e \approx 2 \cdot 10^{19}\mathrm{m}^{-3}$, central ion temperatures $T_i(\rho \leq 0.3)$ are heavily underestimated at higher ECRH powers. This was not only observed for hydrogen (see figure 9.17, left) but also for deuterium plasmas at $\overline{n}_e \approx 2 \cdot 10^{19}\mathrm{m}^{-3}$ at both safety factors $q_{95} \approx 5$ and $q_{95} = 3.7$. It is the result of a heavy overestimation of ion energy transport at high values of T_e/T_i in these low-density-plasmas at high ECRH powers. Nevertheless, at ITER-like heating powers of $P_{ECRH} \approx 1.3$ MW, predictions of central ion temperatures are still very good. The relative deviation of the predicted ion temperature $T_i(\rho = 0.1)$ from the experimental ion temperature is only $(-4 \pm 14)\%$ for ITER-like heated plasmas (average over all plasmas with $0.8\ \mathrm{MW} \leq P_{ECRH} \leq 1.8\ \mathrm{MW}$).

9.1.9 Edge ion heat fluxes

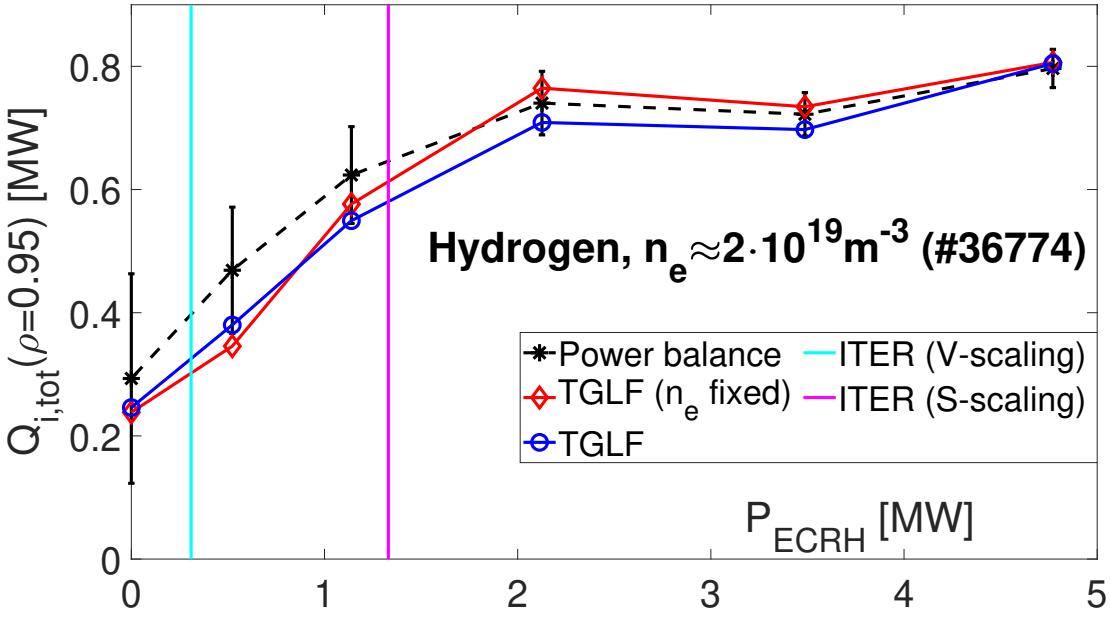

Figure 9.18: Edge ion heat fluxes obtained from power balance simulations are compared with edge ion heat fluxes obtained from ASTRA-TGLF simulations with prescribed and with evolving density. Simulations were performed with boundary at $\rho_B = 0.95$.

The edge ion heat flux is presently considered to potentially be the fundamental quantity governing the occurrence of L-H transitions (see section 5.4). Therefore, correctly predicting L-H transitions requires high precision in the prediction of the edge ion heat flux $Q_{i,edge}$. To assess the prediction quality for $Q_{i,edge}$, a set of simulations with prescribed density profiles (and only evolving temperature and poloidal flux profiles) was performed in addition to the simulations with evolving density.
As the hydrogen example in figure 9.18 shows, the predicted $Q_{i,edge}$ follows very well the curve obtained from power balance (PB) simulations. Most predictions are even inside of experimental error bars.
Figure 9.19 and table 9.2 give a summary of the predicted edge ion heat fluxes for all plasmas in the database. One recognizes that in simulations with evolving density as well as in simulations with prescribed density, TGLF-Feb20 tends to underestimate the value for $Q_{i,edge}$ slightly. In simulations with evolving density, the average ($\pm$ standard deviation) relative deviation $(Q_{i,edge}(\mathrm{TGLF}) - Q_{i,edge}(\mathrm{PB}))/Q_{i,edge}(\mathrm{PB})$

was $(-8 \pm 13)\%$, in simulations with prescribed density, it was $(-10 \pm 23)\%$. Especially at lower ECRH powers (and around ITER-relevant $P_{ECRH} \approx 1.3$ MW), one observes large negative relative deviations between experimental and predicted edge ion heat fluxes. This is a result of a higher sensitivity of $P_{ei} \propto (T_e - T_i)/T_e^{3/2}$ against errors in the temperature profiles at lower ECRH powers, as examined in figure 8.2. The strong outlier with $Q_{i,edge}(\mathrm{PB}) = 2.2$ MW can be explained by its high line-averaged density of $\overline{n}_e = 4.5 \cdot 10^{19}\mathrm{m}^{-3}$ making $P_{ei} \propto n_e^2$ very sensitive to errors in the predicted temperature profiles.

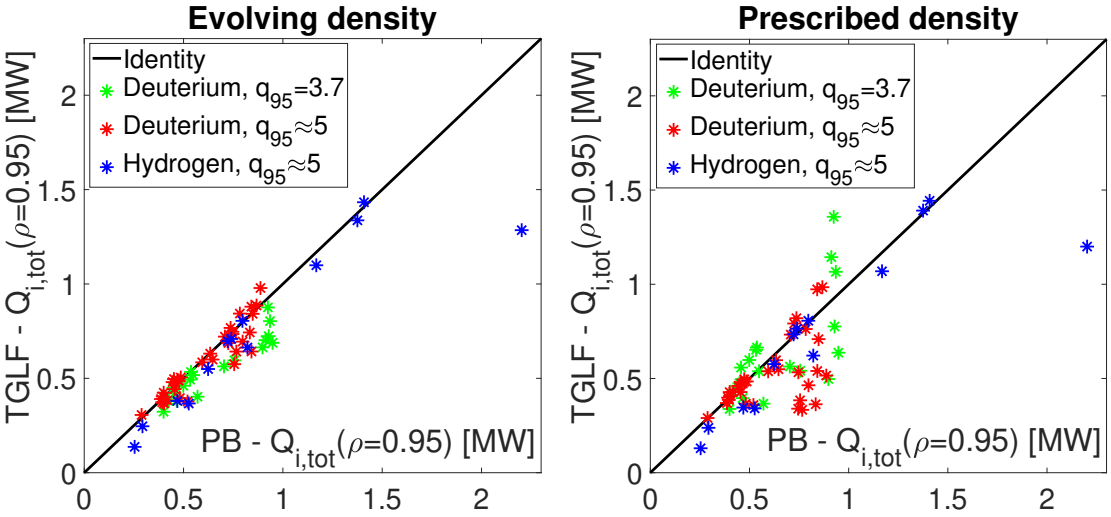

Figure 9.19: For all 66 datapoints, the edge ion heat fluxes obtained from power balance simulations are compared with the edge ion heat fluxes obtained from ASTRA-TGLF simulations with evolving density (left) and with prescribed density (right). Simulations were performed with boundary $\rho_B = 0.95$.

Rather underestimating than overestimating $Q_{i,edge}$ is considered to be beneficial since it makes results about L-H transitions in PFPO-1 a bit conservative, i.e. if ASTRA-TGLF predicts $Q_{i,edge} > Q_{i,edge}^{LH}$, one can assume with higher certainty that there is indeed an L-H transition taking place.

Note that in simulations with prescribed n_e-profile, larger fluctuations of the predicted $Q_{i,edge}$ around its power balance value are observed. This is probably the result of a misprediction of the (ion and electron) energy transport caused by IDA profiles not matching the real density profile and therefore yielding the wrong normalized logarithmic gradients of density R/L_{ne}.

Table 9.2: Average ($\pm$ standard deviation) relative deviations of the edge ion heat flux $Q_{i,edge}$. Results are shown by taking the average over all plasmas, only over L-mode plasmas and only over ITER-like heated plasmas.

	All plasmas	L-mode plasmas	$P_{ECRH} \in [0.8\ \mathrm{MW}; 1.8\ \mathrm{MW}]$
H, $q_{95} \approx 5$	(-15 ± 16)%	(-13 ± 15)%	(-16 ± 6)%
D, $q_{95} \approx 5$	(-3 ± 10)%	$(+1 \pm 11)$%	(-4 ± 9)%
D, $q_{95} \approx 3.7$	(-14 ± 10)%	(-15 ± 10)%	(-12 ± 6)%
Full database	(-8 ± 13)%	(-9 ± 14)%	(-7 ± 9)%

Of particular interest in this study is the prediction quality of $Q_{i,edge}$ in L-mode plasmas since the critical value $Q_{i,edge}^{LH}$ has to be exceeded in L-mode before a transition to H-mode occurs. Only considering L-mode plasmas still yields very precise estimates for $Q_{i,edge}$ with relative deviations from PB-simulations of only $(-9 \pm 14)\%$ (see table 9.2). Another important subset of the available data points are ITER-like heated plasmas for which the relative deviations were only $(-7 \pm 9)\%$.
According to F. Ryter, the edge electron heat flux is irrelevant for the prediction of L-H transitions. [58] Therefore, $Q_{e,edge}$ will not be examined in detail here.

9.1.10 Isotope effect

For ITER-PFPO-1 simulations, it is considered to be a problem that TGLF-SAT0 and TGLF-SAT1-Aug19 are calibrated exclusively on GYRO simulations for deuterium plasmas. [35] Therefore, transport simulations were performed with deuterium mass in [35] although all discharges in PFPO-1 will be either hydrogen or helium. In TGLF-Feb20, the ten CGYRO simulations performed to determine the fitting coefficients, were run for pure D plasmas, too. [64] Thus, the mass dependence of the transport predicted by TGLF-Feb20 will be examined a bit more in detail in this section.

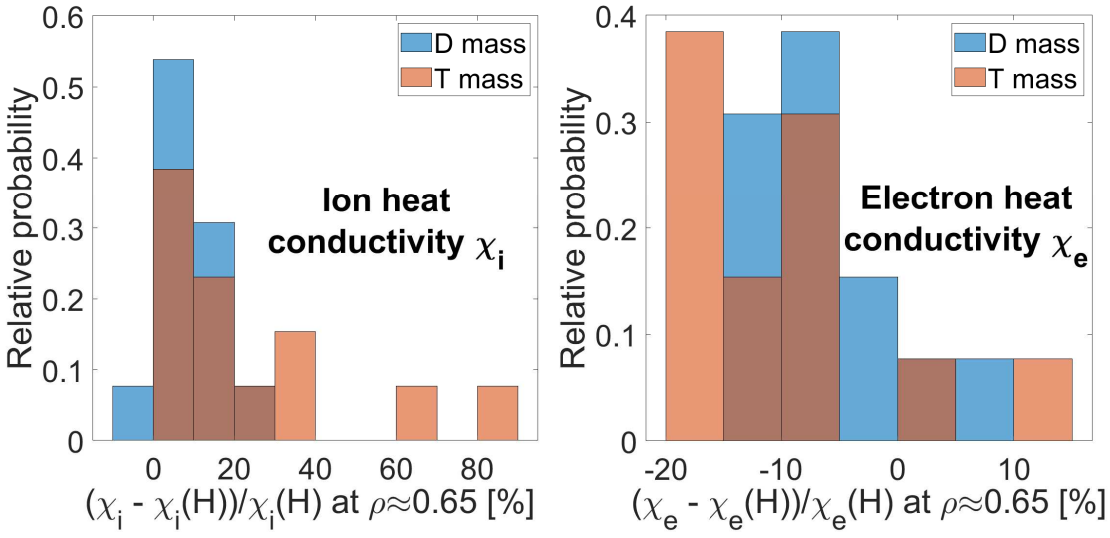

Figure 9.20: Histograms of the relative deviation of the predicted ion (left) and electron (right) heat conductivities. The deviations between simulations with correct ion mass and modified ion mass are shown. Heat conductivities were averaged over the interval $[0.5; 0.8]$.

For this purpose, two further sets of simulations with boundary $\rho_B = 0.95$ were performed for the 13 hydrogen plasmas in which the main ion mass m_i was varied as follows:

- Heat and particle transport is determined by TGLF-Feb20 with either setting the mass to the deuterium mass ($m_i = m_\mathrm{D}$) or to the tritium mass ($m_i = m_\mathrm{T}$)
- The source of cold neutrals and their penetration into the plasma is determined with the hydrogen mass ($m_i = m_\mathrm{H}$)
- The energy exchange between electrons and ions P_{ei} is determined as in a hydrogen plasma

Isotope effects in TGLF on particle transport were already studied in section 9.1.3. Also in these simulations in which m_i was varied, R/L_{ne} tends to decrease with increasing main ion mass m_i as expected from discussions about the particle flux presented in [2].
A first investigation of the isotope effect on electron heat transport was performed in section 9.1.7 where it was found that $\chi_e/T_e^{3/2}$ decreases with increasing main ion mass m_i. Consistently with these results, the electron heat conductivity $\chi_e(\rho \approx$

$0.65)$ at the end of the simulations presented here decreases by $(-6 \pm 7)\%$ if the mass is increased to $m_i = m_\mathrm{D}$ and by $(-10 \pm 9)\%$ if the mass is increased to $m_i = m_\mathrm{T}$ (see figure 9.20, right). Opposite behaviour is found for the ion heat conductivity $\chi_i(\rho \approx 0.65)$ which increases by $(+7 \pm 10)\%$ by setting the main ion mass to $m_i = m_\mathrm{D}$ and by $(+24 \pm 26)\%$ by setting the mass to $m_i = m_\mathrm{T}$ (see figure 9.20, left). Note here, that also the kinetic profiles from which χ_e and χ_i were determined, change slightly due to modifications of the main ion mass.

Linear gyrokinetic simulations presented in [42] can explain the reported result: Energy transport by ITG modes increases with increasing main ion mass m_i for arbitrary collisionalities. Similar mass dependence is found for TEM in the collisionless limit. However, at finite collisionality, collisional stabilization of TEM increases with increasing main ion mass m_i. Therefore, opposite mass dependence (decreasing heat transport with increasing m_i) is found for TEM at finite collisionality. This explains the anti-gyroBohm mass dependence of electron heat transport and the gyroBohm-like mass dependence of ion heat transport which is (at least qualitatively) correctly reproduced by TGLF-Feb20.

For central electron and ion temperatures, predictions do not significantly improve or worsen by setting the mass to m_D or m_T. For predictions of the edge ion heat flux $Q_{i,edge}$, lowest absolute relative deviations $|Q_{i,edge}(\mathrm{TGLF}) - Q_{i,edge}(\mathrm{PB})|/Q_{i,edge}(\mathrm{PB})$ were found in simulations with the correct mass with $(16 \pm 16)\%$. Simulations for hydrogen plasmas with deuterium mass and tritium mass performed worse with deviations of $(19 \pm 14)\%$ and $(23 \pm 17)\%$, respectively. Therefore, this section shows that TGLF-Feb20 is well-suited to predict transport for other isotopes than just deuterium and that TGLF can and should be applied to the actual experimental mass.

9.2 ICRH-heated JET plasmas

9.2.1 Modelling setup

Like for ASDEX Upgrade plasmas, TGLF-simulations for JET plasmas were performed as close as possible to the conditions present in the power balance (PB) simulations (see section 8.2). The profiles for T_e, T_i and n_e were evolving according to the transport equations (4.2) with boundary condition $\rho_B = 0.82$. Additional sets of simulations were performed in which either the temperature profiles or the n_e-profile were prescribed. The current profile was evolving with a sawtooth-induced redistribution of central current density by the modified `MIXINT` subroutine as described in section 9.1.1.
Electron and ion heat sources P_e and P_i were computed as in PB simulations according to equations (8.6) and (8.7). The subroutine `NEUT` was applied to determine the particle source S_e.
Like for ASDEX Upgrade plasmas, electron and ion heat conductivities were calculated as the sum of a neo-classical part χ_{neo}, an effective turbulent conductivity χ_{turb} and a component χ_{saw} providing additional (time-averaged) transport due to sawtooth instabilities. In JET simulations, χ_{saw} was set to the experimental heat conductivity χ_{exp} close to the centre: $\chi_{\mathrm{saw}} = \chi_{\mathrm{exp}} \cdot \mathbb{1}_{[0;0.15]}$. In this equation, $\mathbb{1}$ is the indicator function. Correspondingly, particle transport in JET simulations takes into account turbulent transport, neo-classical transport, the Ware pinch and an average sawtooth effect.
In total, 14 processors were dedicated to TGLF calculations. In contrast to AUG-simulations, four particle species were taken into account in these simulations (main ions, electrons and two impurities, namely beryllium and nickel). Simulations for JET were performed exclusively with TGLF-SAT1 (version February 2020).

9.2.2 Temperature profiles

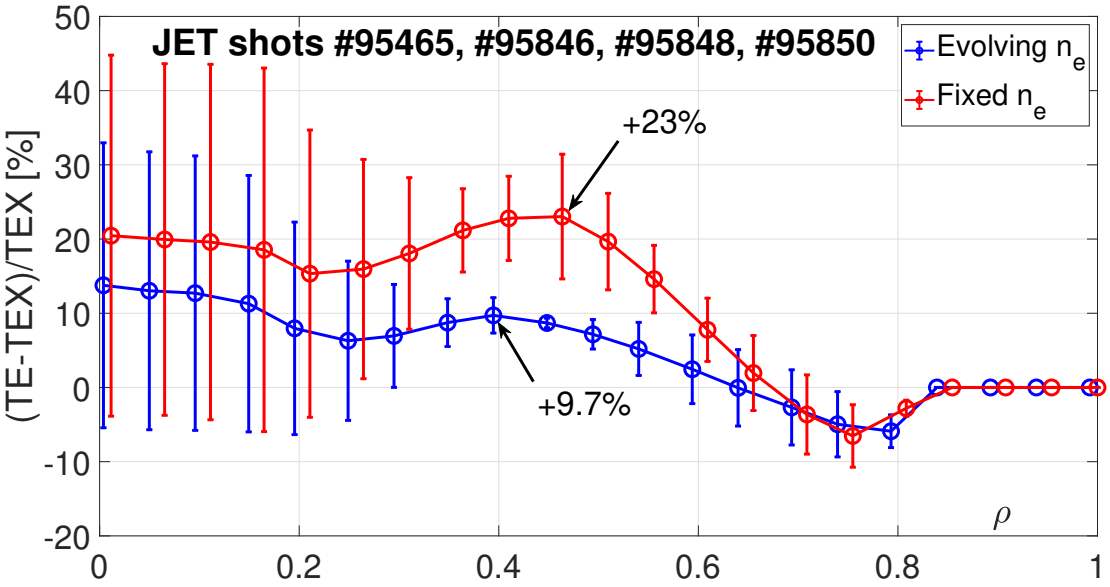

Figure 9.21: Average relative deviations of the predicted electron temperature TE from the experimental electron temperature TEX for simulations with evolving density and simulations with prescribed density. Error bars give the standard deviation over all four shots.

To assess the prediction quality of electron and ion temperatures by TGLF-Feb20, simulations were performed with evolving density profile and with prescribed density profile. For both simulation procedures, figure 9.21 shows the relative deviations $(T_e(\mathrm{TGLF}) - T_e(\mathrm{Exp}))/T_e(\mathrm{Exp})$ between predicted and measured electron temperatures as a function of the normalized toroidal flux radius. Since the boundary was set to $\rho_B = 0.82$, the deviations are zero for $\rho \geq 0.82$. Figure 9.22 shows a rather centrally heated JET plasma that exemplifies the most important results.
Around mid-radius, electron temperatures are significantly overestimated by TGLF-Feb20. This is the result of an underestimation of electron heat transport for $\rho \geq 0.4$. In simulations with evolving density, one finds a maximum relative deviation of $(+9.7 \pm 2.4)\%$ at $\rho = 0.40$. In simulations with prescribed n_e-profiles, one finds significantly larger overestimations with a maximum of $(+23 \pm 8)\%$ at $\rho = 0.45$. This shows that the underprediction of χ_e by TGLF for $\rho \geq 0.4$ is not a result of a misprediction of the density profile. In fact, simulations with evolving density profile also predict slightly stronger density peaking than in the experiment

(see section 9.2.3) which enhances χ_e, thereby compensating the actual underprediction of electron heat transport. For ASDEX Upgrade deuterium plasmas at $q_{95} \approx 5$, a density dependence of $(T_e(\mathrm{TGLF}) - T_e(\mathrm{Exp}))/T_e(\mathrm{Exp})$ was found that was interpreted as a collisionality dependence (see section 9.1.6). Underestimation of electron energy transport was found for plasmas at $\overline{n}_e \approx 4 \cdot 10^{19}\mathrm{m}^{-3}$ that exhibit the highest collisionality ν^* with $\overline{n}_e R_0/T_e^2(\rho = 0.5) = 1.9 \cdot 10^{19}\mathrm{m}^{-2}(\mathrm{keV})^{-2}$. Under the assumption of similar Z_{eff}, a comparable value for the collisionality is found for the considered JET plasmas with $\overline{n}_e R_0/T_e^2(\rho = 0.5) = 2.2 \cdot 10^{19}\mathrm{m}^{-2}(\mathrm{keV})^{-2}$. Thus, underprediction of electron heat transport is found in plasmas of comparably high collisionality across two machines which suggests a tendency of TGLF to underpredict χ_e at high ν^*.

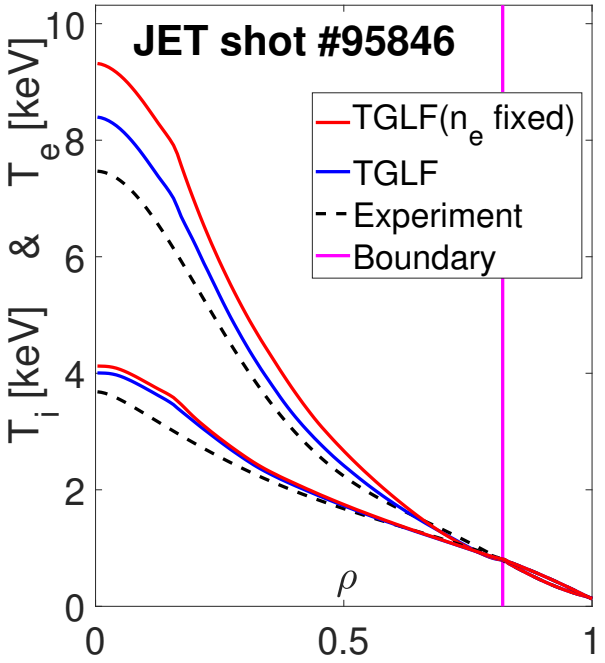

Figure 9.22: Electron and ion temperature profiles from simulations and from experiment.

For very central regions in the plasma, stronger fluctuations of the predicted elctron temperature around $T_e(\mathrm{Exp})$ appear. This might not be a result of predictions by TGLF alone, but also of the predicted power deposition by PION. Nevertheless, on average, $T_e(\rho = 0)$ is very well predicted with a relative deviation of $(+14 \pm 20)\%$ in simulations with evolving density and $(+21 \pm 25)\%$ in simulations with prescribed density.

In ASDEX Upgrade deuterium plasmas at $q_{95} \approx 5$ and $\overline{n}_e \approx 4 \cdot 10^{19}\mathrm{m}^{-3}$, transport is not only underestimated in the electron heat channel, but also in the ion heat channel (see figure 9.15, left). The same feature is observed for JET plasmas, too. Here, the ion heat conductivity χ_i is systematically underestimated for $\rho \lesssim 0.65$. Therefore, the normalized logarithmic gradients of the ion temperature R/L_{Ti} are larger in simulations than in experiment (see figure 9.23). This holds for simulations with evolving density as well as simulations with prescribed density.

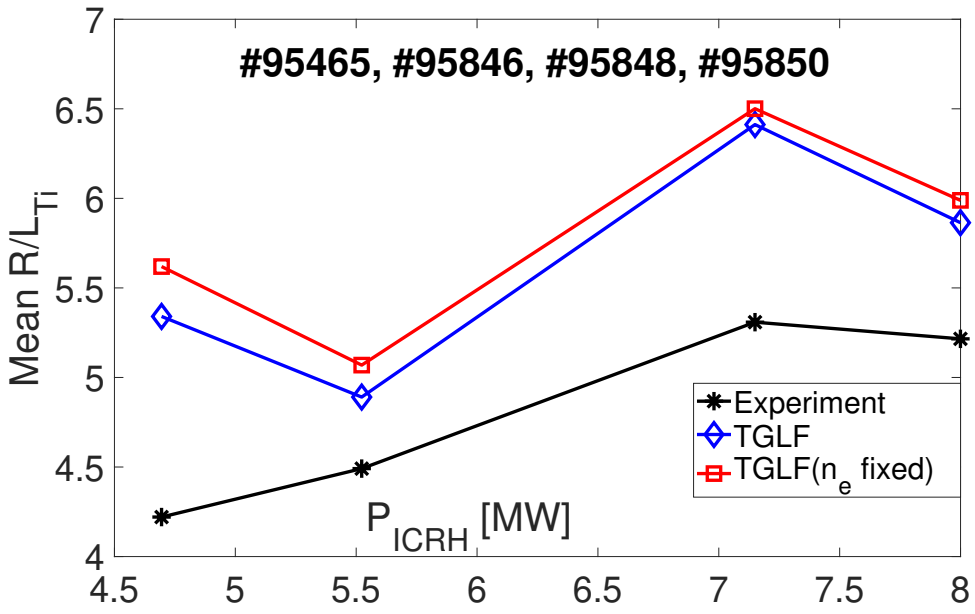

Figure 9.23: Normalized logarithmic gradients of ion temperature from simulations and from experiment. Averages are taken over $\rho \in [0.38; 0.62]$.

The overestimated R/L_{Ti} around mid-radius push the predicted ion temperatures slightly above the experimental profile. Nevertheless, central ion temperatures are very well predicted. In simulations with evolving density, the average ($\pm$ standard deviation) relative deviation of $T_i(\rho = 0)$ is only $(T_i(\mathrm{TGLF}) - T_i(\mathrm{Exp}))/T_i(\mathrm{Exp}) = (+4 \pm 5)\%$. In simulations with prescribed density, $T_i(\rho = 0)$ is overestimated by only $(+5 \pm 6)\%$.

9.2.3 Density profile

In JET, the experimental density profiles were obtained from the High Resolution Thomson Scattering (HRTS) diagnostic which is known to be a very reliable diagnostic. This allows for a more thorough analysis of the prediction quality of particle transport by TGLF than for ASDEX Upgrade plasmas.
Figure 9.24 (left) shows an example for the density profile of a JET plasma. In simulations with evolving n_e-profiles as well as evolving temperature profiles, the predicted density profiles are significantly steeper than the measured profiles. There is a too strong inward pinch that leads to an overestimation of the normalized loga-

rithmic gradient of density R/L_{ne} around mid-radius (see figure 9.24, right).
In a second set of simulations, the temperature profiles $T_e(\rho)$ and $T_i(\rho)$ were prescribed to maintain the correct normalized logarithmic gradients of the temperature profiles (within experimental uncertainties). This approach allows one to check for the origin of the too strong inward pinch observed in simulations with evolving T-profiles. Since the particle source in the simulation domain $\rho \leq 0.82$ is negligibly small, the density profiles evolve to match the zero flux condition.

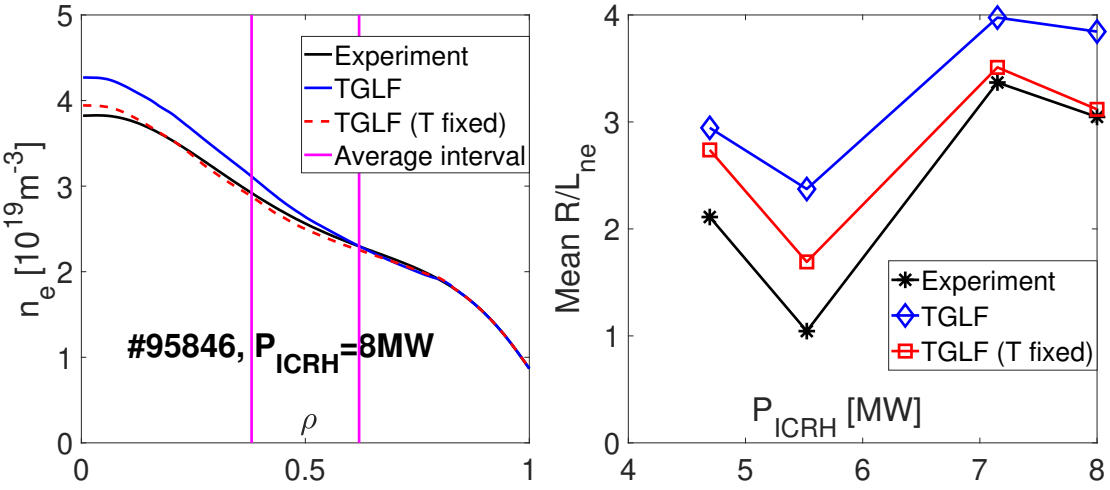

Figure 9.24: Left: Density profile for an ICRH-heated JET-plasma. Right: Normalized logarithmic gradients of density (averaged over the interval $[0.38; 0.62]$) for all four JET shots. Results from the HRTS diagnostic are shown together with simulation results.

In simulations with fixed T-profiles, the predicted density profiles are closer to the experimental ones and R/L_{ne} around mid-radius is significantly better predicted than in simulations with evolving temperature profiles. This shows that the too steep density profile in simulations with evolving T-profiles is a result of the considerably too steep electron and ion temperature profiles. A stronger inward pinch, and thus, a too peaked n_e-profile is observed when R/L_{Ti} and R/L_{Te} are overestimated. This is consistent with results from linear GS2 simulations presented in [15] that show that the NLG R/L_{ne} of the stationary density profile satisfying the zero flux condition increases with increasing R/L_{Te}.

9.2.4 Edge Ion Heat Fluxes

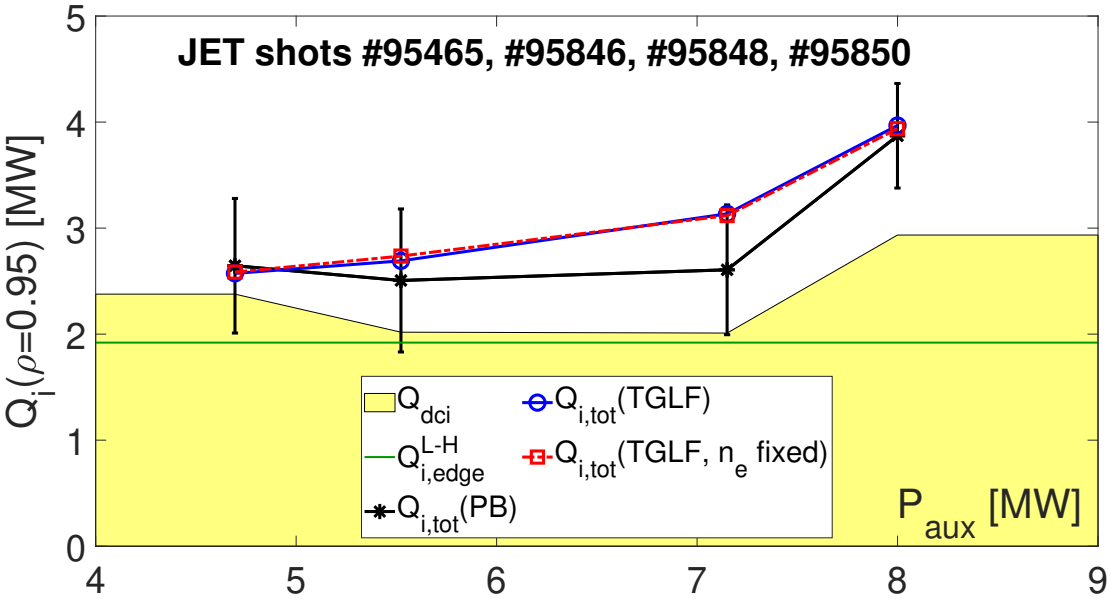

Figure 9.25: Edge ion heat fluxes as determined from TGLF simulations compared to the power balance values. The horizontal green line gives the L-H threshold determined from equation (5.19).

In ICRH-heated JET-plasmas, ion heat fluxes $Q_{i,tot}$ are not exclusively determined by core transport, but also by the fraction of the ICRH power that is directly deposited to the ion heat channel. Neglecting effects on $Q_{i,tot}$ from cold neutrals ionization, one can write the ion heat flux as $Q_{i,tot} \approx Q_{dci} + Q_{ei}$. Core transport, and therefore TGLF, only influences ion heat fluxes through the collisional electron-ion heat exchange Q_{ei}.

Figure 9.25 shows predicted edge ion heat fluxes from simulations with fixed density and from simulations with evolving density together with the values obtained in the power balance analysis. Since (in contrast to some ECRH-heated ASDEX Upgrade plasmas) for ICRH-heated JET plasmas the temperature profiles $T_i(\rho)$ and $T_e(\rho)$ are close together such that $T_e(\rho) < 3 \cdot T_i(\rho)$ for all $\rho \in [0; 1]$ and for all plasmas, it is simple to determine effects of the temperature profiles on the edge ion heat fluxes: Ceteris paribus, overestimating T_e leads to overpredictions in $Q_{i,edge}$ and overestimating T_i leads to underpredictions on $Q_{i,edge}$. On average, TGLF is a very good predictor for edge ion heat fluxes $Q_{i,edge}$ also for ICRH-heated JET plas-

mas. In simulations with evolving density as well as in simulations with prescribed density, predicted edge ion heat fluxes deviate by only $(+7 \pm 10)\%$ from the power balance values for $Q_{i,edge}$. For all four plasmas, the predictions are even within the experimental uncertainty.

9.3 Spectra of micro-instabilities

In this section, the predicted spectra of the growth rate γ and the real frequency ω_r after convergence of the TGLF simulations are analyzed. Since there is no experimental data on these spectra, their plausibility is examined by comparison to expectations from (analytic) theory and to linear gyrokinetic simulations performed with the GKW code. [47]

Figure 9.26 shows the spectra for 14 radial positions $r/a \in (0.66; 0.82)$ of an ITER-like heated hydrogen plasma of AUG shot #36775. In the considered radial domain, the normalized logarithmic gradients vary over the intervals $R/L_{Te} \in (12.0; 15.0)$, $R/L_{Ti} \in (6.3; 10.1)$ and $R/L_{ne} \in (3.1; 5.6)$. The spectrum of the growth rate shows two peaks, one on the ion Larmor radius scale ($k_\theta \rho_s < 1$) and one on the electron Larmor radius scale ($k_\theta \rho_s > 1$). Since the convention in TGLF assigns positive real frequencies to the electron drift direction and negative real frequencies to the ion drift direction, the peak at $k_\theta \rho_s < 1$ corresponds to ITG modes whereas the peak at $k_\theta \rho_s > 1$ corresponds to ETG modes. Other plasmas in the database also show TEMs (see figure 9.27, bottom).

In the spectrum of the growth rate, one observes that $\gamma/(k_\theta \rho_s)$ increases with increasing radius r/a for all wavenumbers k_θ. This can be explained by the increase in the drives R/L_{Te} and R/L_{Ti} of these instabilities with increasing r/a. Equation (5.11) shows that for ITG modes, it is $\gamma/(k_\theta \rho_s) \propto \sqrt{R/L_{Ti}}$. In [26], an analytic expression for the growth rate of ETG modes is derived. For $R/L_{Te} \gg R/L_{Te,crit}$, this expression yields approximately $\gamma/(k_\theta \rho_s) \propto \sqrt{R/L_{Te}}$ in units of c_s/a. Since both, R/L_{Ti} and R/L_{Te} increase with r/a over a large part of the radius, the predicted values for $\gamma/(k_\theta \rho_s)$ follow the theoretical expectations. In plasmas with unstable TEMs, one also observes increasing values for $\gamma/(k_\theta \rho_s)$ because R/L_n increases over a large part of the radius, too.

It is interesting to note that the plasma shown in figure 9.26 is dominated by ETG instabilities at $r/a \approx 0.7$ (value for $\gamma/(k_\theta \rho_s)$ is maximum for $k_\theta \rho_s > 1$) whereas it is dominated by ITG modes at $r/a \approx 0.8$. This does not contradict the theoretical expectations since R/L_{Ti} increases stronger than R/L_{Te} in the considered radial domain $(0.66; 0.82)$. Therefore, the growth rate increases stronger for ITG modes than for ETG modes with increasing r/a.

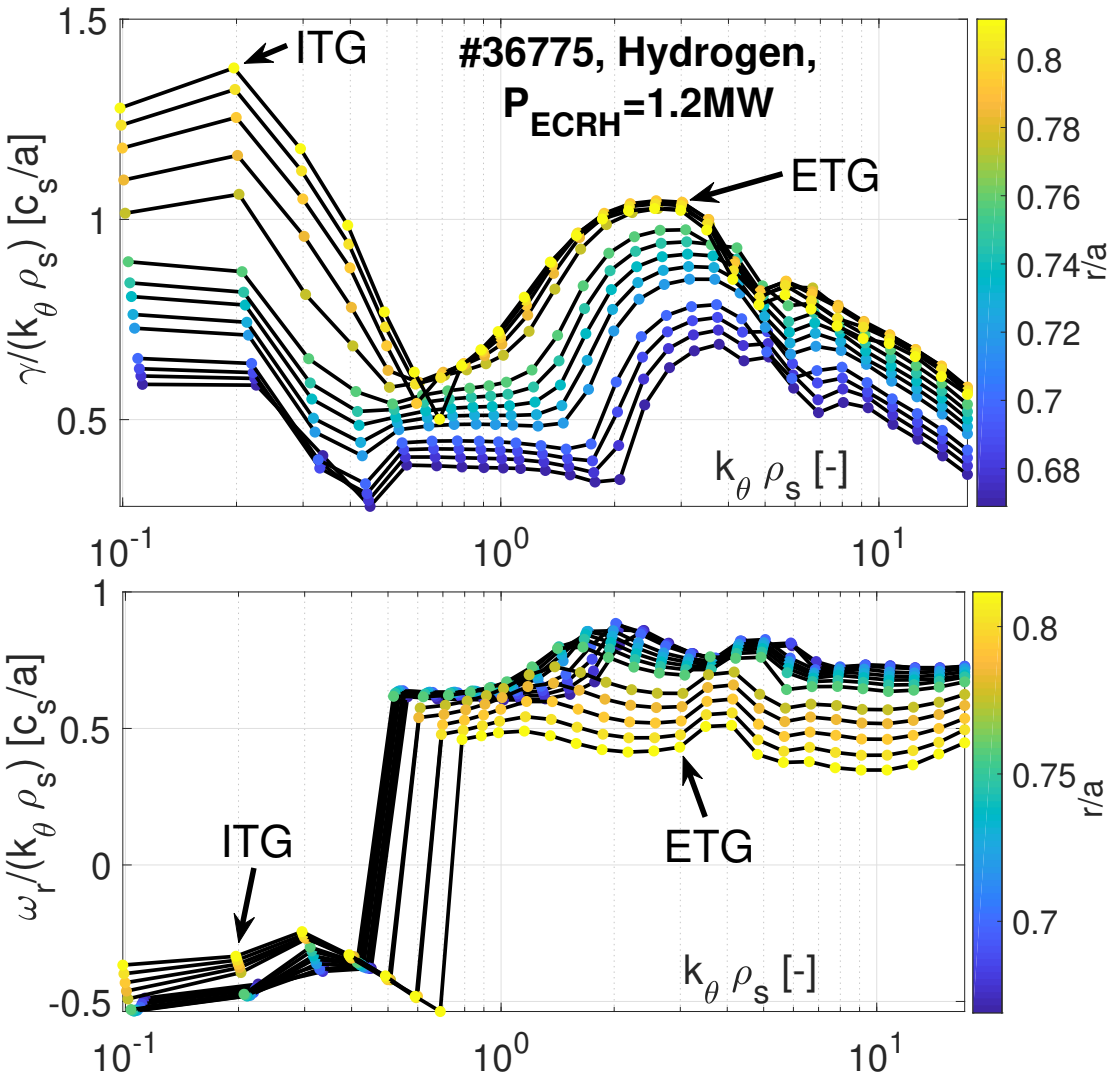

Figure 9.26: Spectra of the growth rate γ (top) and the real frequency ω_r (bottom) of a hydrogen plasma at $\overline{n}_e \approx 3 \cdot 10^{19} \mathrm{m}^{-3}$. Results for different radial positions r/a are shown.

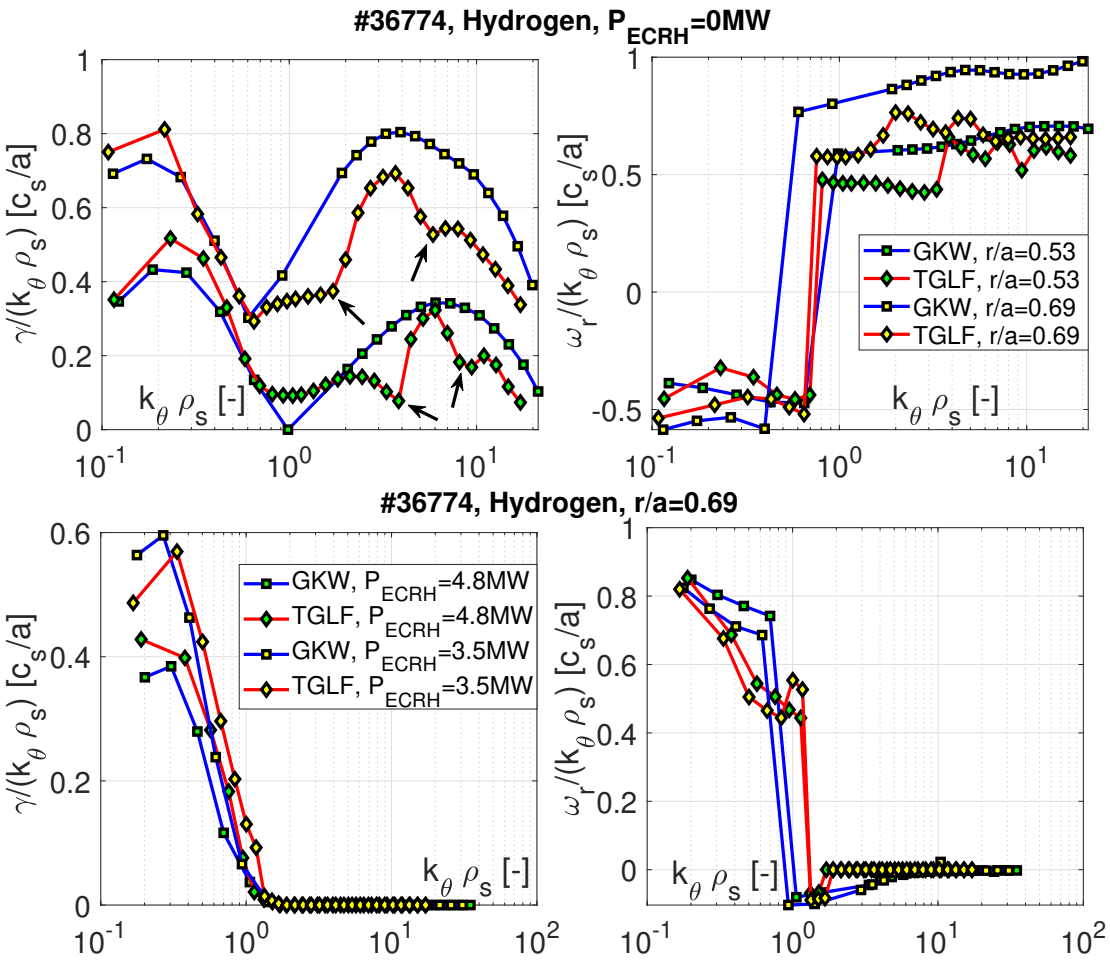

Figure 9.27: GKW and TGLF spectra of the growth rate and the real frequency of a hydrogen discharge at $\overline{n}_e \approx 2 \cdot 10^{19}\mathrm{m}^{-3}$. Top: Results for different radial positions r/a are shown. Arrows mark dips in the ETG profile. Bottom: Results for different ECRH powers are shown.

For twelve hydrogen plasmas, linear gyrokinetic simulations with GKW were performed for the two radial positions $r/a = 0.53$ and $r/a = 0.69$. A subset of these results is shown in figure 9.27.

In the spectrum of the growth rate, one commonly observes dips in the profiles of ETG modes (see figure 9.27, top). These dips are not recovered in GKW simulations. As a result of that, ETG spectra predicted with TGLF tend to be narrower than the corresponding profiles computed by GKW. If plasmas are dominated by ion-scale turbulence ($\gamma \lesssim k_\theta V_{ZF}$ at electron scale), these too narrow γ-profiles will not change the transport predictions by TGLF. However, in case of ETG-dominated

plasmas, this will affect the constructed effective growth rate γ_{model} and therefore also the predicted transport.

For large r/a, TGLF systematically predicts lower values for the maximum $\gamma/(k_\theta \rho_s)$ on electron scales than linear GKW simulations. For $r/a = 0.69$, the maximum $\gamma/(k_\theta \rho_s)$ on high-k_θ scales is underestimated by $(-9 \pm 8)\%$ on average. In the example at the top of figure 9.27, this leads to the prediction of an ITG-dominated plasma by TGLF although according to GKW, the plasma would be in the ETG streamer regime with the maximum $\gamma/(k_\theta \rho_s)$ being on the electron Larmor radius scale leading to considerable ETG transport. At $r/a = 0.53$, relative deviations are comparably weak.

To check why the origin of the relative deviation of $\max(\gamma/(k_\theta \rho_s))$ on the electron-scale is radially dependent, Pearson correlations between the relative deviation of $\max(\gamma/(k_\theta \rho_s))$ at $k_\theta \rho_s > 1$ and the quantities R/L_{ne}, R/L_{Te}, R/L_{Ti}, T_i/T_e and ν^* have been computed. Strongest Pearson correlations were found for the collisionality ν^* with -0.52 and for the temperature ratio T_i/T_e with -0.48. This shows that TGLF underestimates electron-scale growth rates at high collisionalities ν^* or high ratios T_i/T_e.

The set of GKW simulations also contains six cases for which ETG turbulence is entirely suppressed due to high T_e/T_i. In all six spectra, TGLF successfully predicts stability against ETG turbulence as well. This shows that at least for these cases, TGLF correctly predicts the threshold $R/L_{Te,crit}$ for ETG instabilities. Two example spectra without electron-scale turbulence are shown at the bottom of figure 9.27.

Quantitatively, there are some differences between the spectra of linear GKW simulations and TGLF simulations. However, qualitatively, TGLF spectra match very well theoretical expectations. This can be seen in figure 9.28 that shows the predicted dominant micro-instability (highest $\gamma/(k_\theta \rho_s)$) for all examined hydrogen plasmas in a machine-dependent (left) and a machine-independent (right) representation. With increasing ECRH power, the NLG R/L_{Te} and the ratio T_e/T_i increase. Since both drives TEM turbulence, one observes predominantly TEMs at high ECRH power. With increasing density n_e, also the collisionality $\nu^* \propto n_e R Z_{eff}/T_e^2$ increases. As a result of that, one expects ITG modes to be dominant in high density plasmas since TEMs are stabilized by collisions whereas ITG modes are almost unaffected by collisions. This is correctly predicted by TGLF.

It should be noted that not only the total auxiliary heating power, but also the heating method determines the micro-instability with the highest $\gamma/(k_\theta \rho_s)$. Since JET plas-

mas were heated by ICRH which deposits large fractions of the power directly into the ion heat channel, R/L_{Ti} is comparably large and R/L_{Te} is comparably small for the JET plasmas. Therefore, the maximum $\gamma/(k_\theta \rho_s)$ corresponds to ITG modes in all JET spectra at $r/a \in [0.5; 0.8]$.

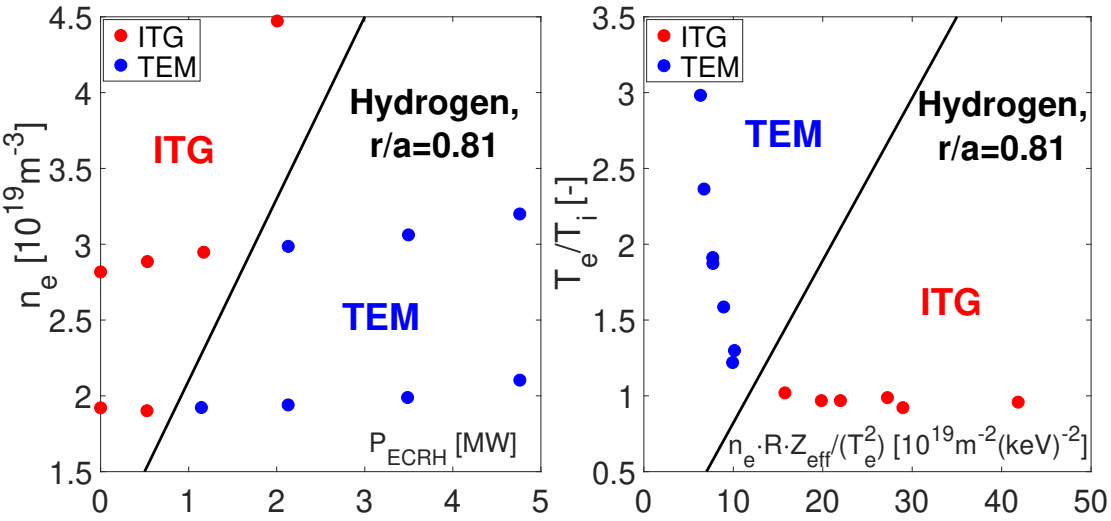

Figure 9.28: Left: Dominant micro-instability of all H plasmas for different ECRH powers P_{ECRH} and different line-averaged densities. Right: Dominant micro-instability at different collisionalities ν^* and different ratios T_e/T_i.

ITER-PFPO-1 plasmas will have $20\ \mathrm{MW}$ of ECRH power corresponding to $P_{ECRH} = 1.3\ \mathrm{MW}$ in ASDEX Upgrade. As one observes in the left plot of figure 9.28, such ITER-like heated hydrogen plasmas can be ITG-dominated or TEM-dominated, depending on the density of the plasma.

Figure 9.29 shows the dominant instability for all plasmas in the database that were either ITG- or ETG-dominated according to TGLF. Since R/L_{Ti} is the drive of

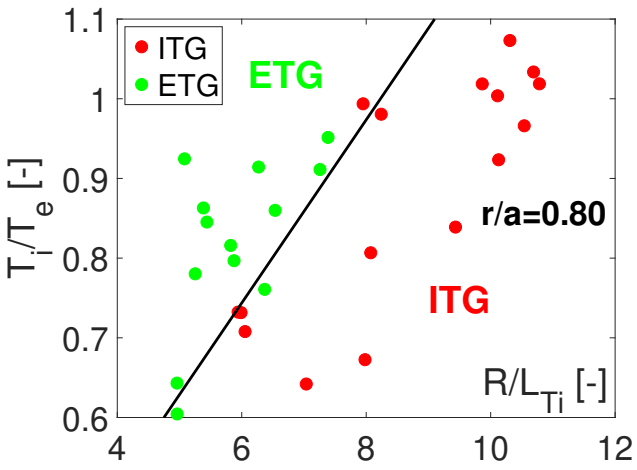

Figure 9.29: Dominant instability for all plasmas with either ETG- or ITG-dominated turbulence.

ITG modes, one expects predominantly ITG turbulence at high R/L_{Ti}. The ratio T_i/T_e is known to destabilize ETG modes and stabilize ITG modes which should lead ETG-dominance at high T_i/T_e. Both is correctly recovered by TGLF.

10 QuaLiKiz simulations

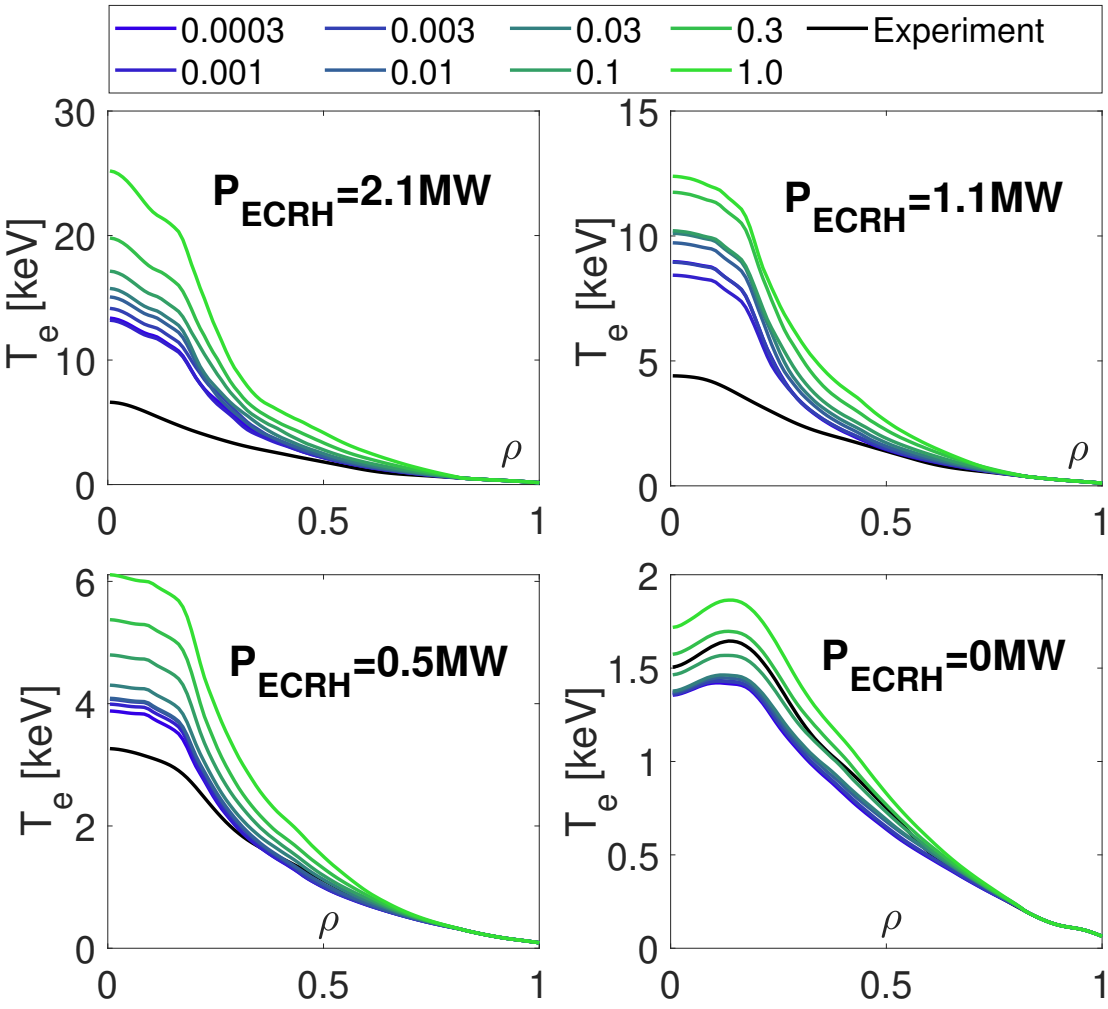

Figure 10.1: Electron temperature profiles from experiment and QuaLiKiz simulations for the hydrogen shot #36774. The collisionality ν^* has been multiplied by the values given in the legend.

Simulations with QuaLiKiz were performed for the six different ECRH power levels of the hydrogen shot #36774 ($\overline{n}_e \approx 2 \cdot 10^{19}\mathrm{m}^{-3}$). The modelling setup for QuaLiKiz simulations was almost identical to the TGLF simulations for ASDEX Upgrade plasmas (see section 9.1.1). However, the effective heat conductivities χ_{turb} were determined with QuaLiKiz (version 2.5.5) [10] and χ_{saw} was set to the experimental heat conductivity χ_{exp} close to the magnetic axis like in TGLF simulations for JET (see section 9.2.1). All simulations were performed with boundary $\rho_B = 0.82$ and with evolving poloidal flux, density and temperature profiles.

It is known that regimes with dominant electron heating (large Q_e/Q_i at mid-radius and therefore large T_e/T_i) and non-negligible collisionality are very challenging for QuaLiKiz. [73] This is due to the combination of strong TEM drive on the one hand and considerable collisional stabilization on the other hand. Therefore, collisionality scans were performed for each plasma in which the true collisionality ν^* has been multiplied by a constant between 0.0003 and 1.0. Simulations with $0.0003 \cdot \nu^*$ can be considered as approximately collisionless. Results of the collisionality scans are shown in figures 10.1 and 10.2. Simulations for plasmas at $P_{ECRH} = 4.8\ \mathrm{MW}$ and $P_{ECRH} = 3.5\ \mathrm{MW}$ which are not shown in the two figures behaved very similar to the $2.1\ \mathrm{MW}$ case.

One observes that with the true collisionality $1.0 \cdot \nu^*$, electron temperatures are overestimated significantly for all plasmas. In plasmas with $P_{ECRH} \geq 0.5\ \mathrm{MW}$, central electron temperatures are also overestimated with reduced collisionality, even in the nearly collisionless case with $0.0003 \cdot \nu^*$. The generally observed lower electron temperatures with reduced collisionality can be explained by the collisional stabilization of TEM turbulence.

It was shown in [73] that the Krook collision operator produces an overstabilization of TEMs in TEM-dominated plasmas. This leads to considerable underestimation of electron heat transport in TEM-dominated plasmas. Since shot #36774 is TEM-dominated for $P_{ECRH} \gtrsim 1\ \mathrm{MW}$ (see figure 9.28), this explains the heavy overestimation of T_e in the higher-power cases that is observed for all collisionalities. However, it should be noted that for these TEM-dominated plasmas, T_e-profiles are even overpredicted for $\nu^* \to 0$ showing that the collision operator is not the only problem QuaLiKiz is suffering from.

For the ion temperatures, one observes good predictions for $P_{ECRH} = 0\ \mathrm{MW}$, i.e. in the ITG regime, and considerably too flat profiles in TEM-dominated regimes ($P_{ECRH} \gtrsim 1\ \mathrm{MW}$). The data point at $P_{ECRH} = 0.5\ \mathrm{MW}$ marks the transition

between these regimes. This behaviour of the T_i-profiles can be explained with results from comparisons between GKW and QuaLiKiz shown in [73]. Results from [73] suggest that in TEM-dominated plasmas, QuaLiKiz predicts higher ratios Q_i/Q_e than quasilinear gyrokinetic simulations with GKW for the same input parameters.

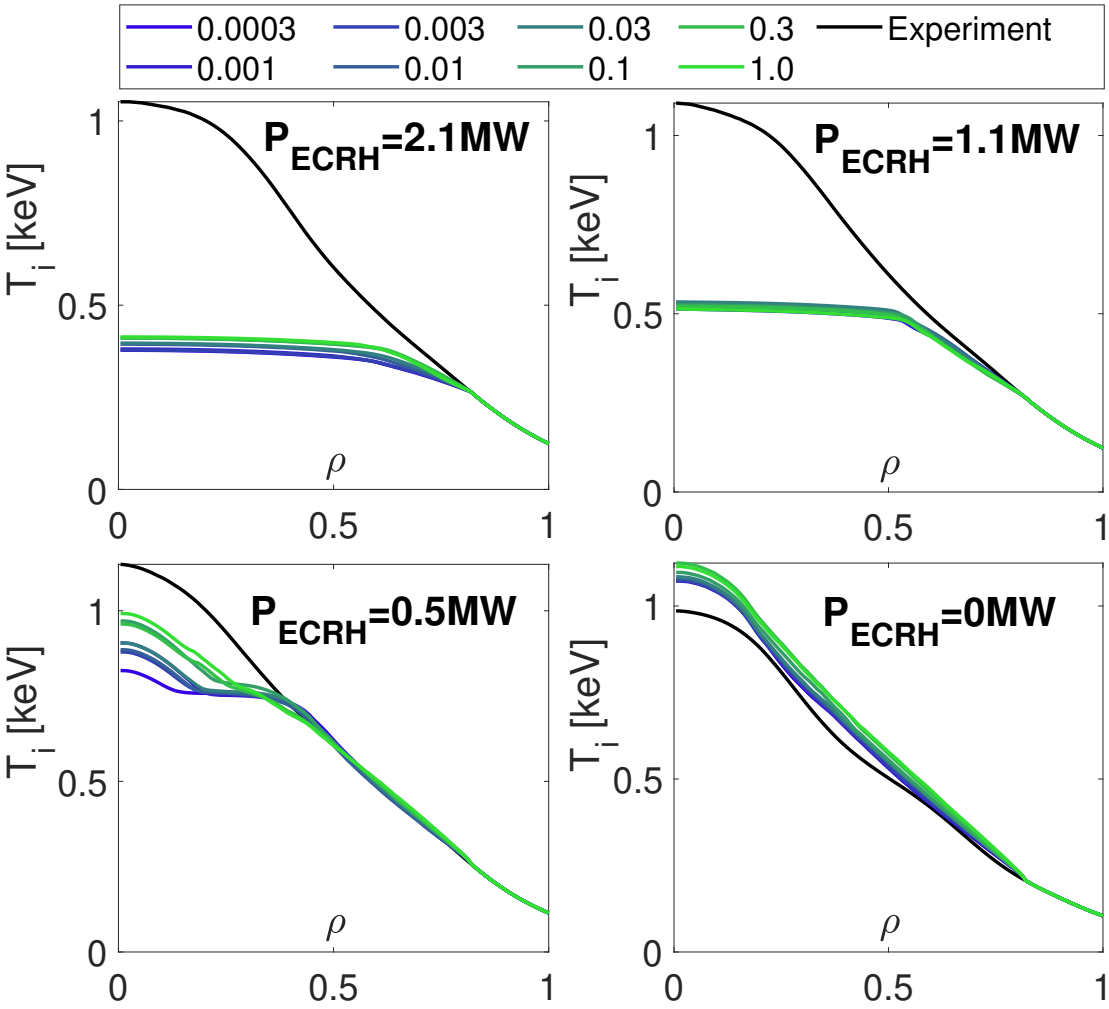

Figure 10.2: Ion temperature profiles from experiment and QuaLiKiz simulations for the hydrogen shot #36774. The collisionality ν^* has been multiplied by the values given in the legend.

This coincides with observations made here that QuaLiKiz overpredicts χ_i/χ_e over a large part of the radius in the TEM-dominated AUG plasmas. Since this overestimation of the ion heat transport compared to electron heat transport appears also for nearly collisionless plasmas, it cannot be a result of the collision operator, but

has to be connected to the eigenfunctions in the fluid limit or the saturation rule.
As figure 9.28 shows, low-density plasmas in ITER-PFPO-1 can be expected to be TEM-dominated. Due to large discrepancies between experiment and QuaLiKiz simulations in TEM-dominated regimes that were found in this analysis, the current version of QuaLiKiz is not recommended to be used for ITER-PFPO-1 predictions. Results from [73] support this statement. However, there is currently a new Krook collision operator under development that could lead to significant improvements in QuaLiKiz predictions.

11 Conclusions

The predictions of the quasi-linear turbulent transport models TGLF and QuaLiKiz have been compared to experimental results from ASDEX Upgrade and JET. In particular, the precision of edge ion heat flux predictions has been examined since this quantity is considered to determine whether the plasma transitions into H-mode or not. Another focus was the validation of central electron temperature predictions since PFPO-1 scenarios at $B_t = 1.8\ \mathrm{T}$ rely on third harmonic heating for which the absorption of EC radiation is highly dependent on central T_e.

Since ASDEX Upgrade offers a comparably large amount of ECRH power of more than $5\ \mathrm{MW}$, the transport models could be tested over an unprecedented range of parameters. In particular, the database includes plasmas with electron heating powers per surface element comparable to the ones in PFPO-1, but also plasmas with considerably lower or higher ECRH power. JET plasmas with ICRH in the database contributed to an even more extensive range of parameters. The temperature ratio T_e/T_i around mid-radius, for example, reaches from values as small as $T_e/T_i = 1.1$ to values as large as $T_e/T_i = 5.7$.

With the newest version of TGLF-SAT1 (February 2020), electron and ion temperature profile predictions do not suffer from a shortfall of edge energy transport, as it was the case in the previous version of August 2019. Instead, predicted temperature profiles in L-mode plasmas follow very well the experimental profiles close to the edge. In L-mode plasmas, this allows one to push the simulation boundary further outside until $\rho_B = 0.95$, maybe even further.

Around mid-radius, the deviation of predicted electron temperatures from the experimental profile was found to depend on the line-averaged density $\overline{n}_e$. For low densities, TGLF-Feb20 predicts a too large electron heat transport whereas for high densities, TGLF-Feb20 underestimates electron heat transport. An analogous result was obtained for ion temperature predictions around mid-radius. JET simulations confirm that such a density dependence of the relative deviation can also be

interpreted as a collisionality dependence with underestimation of electron and ion heat transport at high ν^* and overestimation at low ν^*.

Close to the magnetic axis, electron temperature predictions are very good on average. For $T_e(\rho = 0.2)$, relative deviations of $(0 \pm 14)\%$ were found across the full database of ASDEX Upgrade plasmas and $(-3 \pm 13)\%$ for ITER-like heated plasmas with $P_{ECHR} \approx 1.3\ \mathrm{MW}$. In JET simulations with ICRH, also high prediction quality for central electron temperatures was found. Such a high accuracy in the modelling of central electron temperatures gives confidence for reliable predictions of third harmonic EC absorption in ITER-PFPO-1.

Good predictions were also found for the edge ion heat flux with only a slight tendency to underestimate $Q_{i,edge}$. Across all ASDEX Upgrade plasmas in the database, the relative deviation between TGLF-Feb20 and power balance is $(-8 \pm 13)\%$; for ITER-like heated plasmas, it is (-7 ± 9)%. Therefore, TGLF-SAT1 can be expected to provide reliable predictions of the edge ion heat flux for projections of H-mode accessibility in ITER-PFPO-1. The slight tendency to underestimate $Q_{i,edge}$ assures predictions of L-H transitions to be conservative such that no L-H transition should be predicted if there is none.

Although TGLF-SAT1 is exclusively calibrated on deuterium (^{2}H) plasmas, the model yields good predictions for hydrogen (^{1}H) plasmas as well. Predicted isotope effects like decreasing R/L_{ne} with increasing main ion mass due to a reduced inward pinch were found to coincide with experimental observations and expectations from analytic theory. Best predictions for $Q_{i,edge}$ in hydrogen plasmas were obtained when the hydrogen mass was used. It is therefore recommended to always use the actual experimental mass in TGLF simulations.

Comparisons with GKW and theoretical expectations show that TGLF predicts the correct dominant micro-instabilities in different regimes. For the value of the maximum of $\gamma/(k_\theta \rho_s)$ on the electron Larmor radius scale, underestimations were found for high collisionalities ν^* and/or high ratios T_i/T_e. Since the database spans over different heating powers and line-averaged densities, regimes with radially local ITG-dominance, ETG-dominance and TEM-dominance could be explored. Therefore, this study certainly covers the turbulent transport conditions which will be present in ITER PFPO-1.

In QuaLiKiz simulations, serious discrepancies have been found between experiment and model predictions, especially in TEM-dominated plasmas at high ECRH-power. The collision operator produces a too strong stabilization of trapped elec-

tron modes which results in heavy overestimations of central electron temperatures. Furthermore, QuaLiKiz significantly overpredicts the ratio χ_i/χ_e between ion and electron heat transport in TEM-dominated plasmas, even in the collisionless limit. This results in too high T_e-profiles together with too flat T_i-profiles even for $\nu^* \to 0$. Therefore, the application of the current version of QuaLiKiz to ITER-PFPO-1 plasma conditions is not recommended. On the other hand, TGLF-Feb20 delivered very good results under ITER-like conditions and promises high accuracy in predicting central electron temperatures and edge ion heat fluxes.

Since theorists always find new ways to develop new transport models, their verification is a never-ending task. In October 2020, an entirely new saturation rule, SAT2, was released for TGLF. [64] For TGLF-SAT2, a validation against an extensive dataset is still pending and will require further research.

12 Acknowledgement

Hundreds of people worldwide are working towards the realization of the first practical nuclear fusion reactor. Also the success of this master thesis would not have been possible without the support and assistance of many people. At this point, I want to express my deepest appreciation and gratitude to all people that contributed directly or indirectly to that work.

First of all, special thanks goes to Clemente Angioni for his exceptional guidance and assistance throughout this master project. I am very grateful to him for his unwavering support in many technical, physical and organizational issues.

Many thanks go to Prof. Emanuele Poli for giving me the opportunity to do my master thesis at the Max Planck Institute for Plasma Physics and for examining my work. Lots of thanks also go to Prof. Johannes Hecker Denschlag, the second examiner of this thesis.

A part of the research for this master thesis was carried out at Culham Centre for Fusion Energy. I am thankful to the PROMOS scholarship for financial support and to Hyun-Tae Kim, Francis Casson and Philip A. Schneider for tremendous organizational support. Simulations of JET plasmas benefited greatly from Nicola Bonanomi's and Paola Mantica's knowledge and assistance for which I also want to show my gratitude at this point.

I would also like to express my sincere appreciation to Giovanni Tardini and Emiliano Fable for their help with the installation and usage of the ASTRA modelling suite. Indeed, I am grateful to all members of the transport group for fruitful discussions and enormous support in various ways.

A ASTRA source code for ECRH

Power balance simulations of ECRH-heated ASDEX Upgrade plasmas:

```
!Template for ASTRA for ECRH heated AUG plasmas
!(based on template by Emiliano Fable)
!All profiles created in ASTRA downstairs are now done
!in RHO (rho_tor)

!GENERAL PARAMETERS BLOCK--------------------------------

!Time step definition
TAUMIN=0.050;  TAUMAX=0.050;
CF7 = 5.0*TAUMAX;

!----------------------------
AMAIN=AMJ; ZMAIN=ZMJ; !Mass & charge of main ion species
AIM1=10;  !mass of main impurity (boron)
ZIM1=5;   !charge of main impurity (boron)
AIM2=14;  !Nitrogen
ZIM2=7;   !Nitrogen
AIM3=4;   !Helium
ZIM3=2;   !Helium

ZEF=ZEFX; !Use the values of ZEF which where determined
!inside of ASTRA beforehand
!ZEF=min(6.0,max(1.0,ZEF*(1.0-0.1*(UPLB-ZRD28X)/ZRD28X)));
!Adjust ZEF such that loop voltage converges to
!experimental loop voltage

```

```
27 CF15=1.0;
28 NIZ1=(ZEFX-ZMJ)*NE/((ZIM1-ZMJ)*ZIM1);
29 !NIZ1=CF15*CAR44X;
30 NIZ2=0.0*CAR44X;
31 NIZ3=0.0*CAR44X;
32
33 !DENSITY BLOCK-----------------------------------------
34 !Particle sources
35 NNCL=0.00001; !Cold neutrals
36 NNWM=0.0000; !Warm neutrals
37 NEUT:0.05:0.1:;
38 SNN=SNNEU;
39
40 !Density of main plasma (mix of H and D):
41 NDEUT=NE-ZIM1*NIZ1-ZIM2*NIZ2-ZIM3*NIZ3;
42 NMAIN=NDEUT;
43 NI=NDEUT+NIZ1+NIZ2+NIZ3;
44
45 ATREQ = 0.2;
46 CNBI1 = 8; CNBI2 = 1; CNBI2 = 3; CNBI4 = 1;
47 CHI2=0.20;
48 TORBA_T(PEECR, CUECR, 0.d0, CHI2)>::0.15:0.5:;
49 !3rd argument: dumping files for TORBEAM stand-alone,
50 !0.=no, 1.=yes
51 RABBIT2(CHI2)>::0.25:0.5:;
52 !CHI2=delay of first RABBIT2 call w.r.t. t_beg
53 SN=SNEBM;
54
55 PRAD = PRADX;
56 PE=POH+PEBM+PEECR-PEICL2-PRAD;
57 PI=PIBM+PEICL2;
58
59 !Plasma rotation
60 VPOL=VPSWW; !Poloidal rotation
61 VTOR=VTORX; !Toroidal rotation
```

```
ER=BTOR*(VDIA-VPOL)+BTOR*AMETR*MU*VTOR/RTOR;

!Initial condition for density and temperatures
NE=NEX;
TE=TEX;
TI=TIX;
NE:AS;
TE:AS;
TI:AS;

SF1 = 0.0; SFF1=0.0;

!CURRENT BLOCK-----------------------------
!CU:AS;
CU:EQ;
MU=MUX;
!Bootstrap coefficients
HC=HCSA;
DC=DCSA; XC=XCSA;
CC=CNSA; CD=CUBM+0.*CUECR;

IPL=IPLX; !Total plasma current equal to
!experimental value

!Output------------------------------------------

DBPBout:0.02:0.02::;

!!!!!!!!!!!!!!!!!!!!!!!!!!!!!!!!!!!!!!!!!!!!!!!!!!
!Plotting radial profiles

!Pag1
Te\TE\\TEX\-2; ne\NE\\NEX\-5;
NZ1\NIZ1\\CAR44X\-13; VTOR\VTOR\\VTORX;
Jpar\CU\-4; q\1./MU\-21;
```

```
\; CUE\CUECR;

Ti\TI\\TIX\-2; ni\NI\-5;
\; NIBM\NIBM;
Jbs\CUBS\-4; shir\SHEAR; ZEF\ZEF\\ZEFX; CUB\CUBM\;

!Pag2
QET\QETOT\5; QIT\QITOT\5; QNT\QNTOT\50; PEI\PEICL\-22;
PE\PE\-22; PI\PI\-22; PECH\PEECR;  \;

QE\QE\5; QI\QI\5; QN\QN\50;  PEI2\PEICL2\-22;
PEBM\PEBM\-22; PIBM\PIBM\-22; PRD\PRAD\-22; POH\POH\-22;

!Plotting Time Traces
Te0_TE(0); Teb_TEB; Ti0_TI(0);
TeTi_TE(0)/TI(0); vloo_UPL(ROC)_5;
Teib_TE(ROC)/TI(ROC); neb_NE(ROC);
q0_1./MU(0); QeB_QEB;
q1_1./MU(ROC); Zef_ZEF(0); Ipl_IPL; Icd_ICD(ROC);
Ibs_IBS(ROC); Iohm_IOHM(ROC);
Itot_ICD(ROC)+IBS(ROC)+IOHM(ROC);
Ecrh_VINT(PEECR,ROC);
abc_AMETR(ROC); g2_G22(ROC);
!-------------------------------------------------------
```

B ASTRA source code for ICRH

Power balance simulations of ICRH-heated JET plasmas:

```
!JET ICRH equ file for PB simulations
!Author: Christian Karl Kiefer
!(based on equ-file by Paola Mantica)

!CAR vectors legend
!CAR11x       ! pdce
!CAR12x       ! pdci
!CAR7X        ! pde
!CAR27X       ! NBI fast ions density

!-------------------------------------------------------
!Mass and charge of main ion species
AMAIN = AMJ;   ZMAIN=ZMJ;

TAUMIN=0.050;  TAUMAX=0.050;

!Initial conditions
TE=TEX;          TI=TIX;          NE=NEX;
MU=1./MUX; !q-profile in exp-file

!power profiles definition
PEBM=CAR11X;   !icrh pdce
PIBM=CAR12X;   !icrh pdci
PEICR=CAR7X;   !icrh pde
PIICR=0.;
PRAD=F3X;
```

```
27 SNEBM=0;            !electron source from NBI
28 NIBM=CAR27X; !total fast ion density NBI+ICRH
29 PBLON=0.;
30 PBPER=0.;
31
32 !Parameters NNCL and NNWM defined in exp-file
33 NEUT:0.01:0.05::;
34 SNN=SNNEU;
35 SN=SNEBM;
36
37 ZIM1=4.;  AIM1=9.;  !first thermal impurity (Be)
38 ZIM2=24.; AIM2=58.; !second thermal impurity (Ni)
39 !zim3=0.;
40 ZIM3=1.;  AIM3=1.;  ! fast ions from ICRH
41
42 NIZ1=0.03*nex;
43 NIZ2=0.002*nex;
44 NIZ3=NIBM + 1.0e-6; !Avoid zero
45 !niz3=0.;
46 NIX=NEX-ZIM1*0.03*NEX-ZIM2*0.002*NEX-ZIM3*NIZ3+0.03*NEX+0.002*NEX;
47 !NDEUT has to satisfy quasineutrality
48 NDEUT = NE-ZIM1*NIZ1-ZIM2*NIZ2-ZIM3*NIZ3;
49 NI=NDEUT+NIZ1+NIZ2;   !these are only thermal species!
50 NMAIN = NDEUT ;   !just main ions
51 ZEF=(NDEUT+NIZ1*ZIM1**2+NIZ2*ZIM2**2+NIZ3*ZIM3**2)/NE;
52
53 !Impurity density sources
54 SF1 = 0.0; SFF1 = 0.0;
55
56 VTOR=(RTOR+SHIF+AMETR)*VTORX;
57 !exp-file contains angular frequency
58 ER=BTOR*AMETR*MU*VTOR/(RTOR+SHIF+AMETR);
59
60 !Density and temperatures assigned
61 NE:AS;
```

```
62 TE:AS;
63 TI:AS;
64
65 PEX=PEBM + PEICR; !auxiliary electron heating power
66 PE=POH+PEX-PRAD-PENEU-PEICL2;
67 PI=PIBM+PIICR+PINEU+PEICL2;
68
69 !Poloidal flux equation
70 !CU:AS;
71 CU:EQ;
72 CC=CNSA;
73 HC=HCSA;   DC=DCSA;   XC=XCSA;
74
75 !Total plasma current fixed from experimental value
76 IPL=IPLX;
77
78 !Volume integrals
79 CAR4=vint(PEBM);                !volume integral of PDCE
80 CAR5=vint(PIBM);                !volume integral of PDCI
81 CAR6=vint(PEiCR);               !volume integral of PDE
82 car64=vint(piicr);      !volume integral of PIICR
83
84 !Electrons:
85 car53=qoh+car4+car6-qrad-qeneu-qeicl;
86 !Ions:
87 car54=car5+car64+qineu+qeicl;
88
89 !-------------------------------------------------------
90
91 DBPBoutICRH:0.02:0.02::;
92
93 !--------------------Radial outputs--------------------
94
95 Te\TE\\TEX\-2;ne\NE\\NEX\-5; nZ1\NIZ1\-13;nZ3\NIZ3\-13;
96 Jpar\CU\-4; q\1./MU\\mux; gTe\-grad(TE); gTi\-grad(TI);
```

```
97  Ti\TI\\TIX\-2; ni\NI\\NIX;  nZ2\NIZ2\-13; ZEF\ZEF\\ZEFX;
98  Jbs\CUBS\-4;shir\SHEAR; gTex\-grad(TEX);gTix\-grad(TIX);
99  !-------------------------------------------------------
100 !Between PE and PETOT should be no difference
101 !powers and their integrals
102 !-------------------------------------------------------
103 PDCE\PEBM\-776; PDE\PEICR\-776;
104 PDCI\PIBM\-776; PIIC\PIICR\-776;
105 PENEU\PENEU\-776; \; PEI2\PEICL2\-776; \;
106 PETOT\PETOT\-776;PE\PE\-776;PITOT\PITOT\-776;PI\PI\-776;
107 PINEU\PINEU\-776; PRAD\PRAD\-776; \; Poh\POH\-776;
108 !-------------------------------------------------------
109
110 QeNBI\CAR4\-500; QiNBI\CAR5\-500;
111 QRAD\QRAD\-500; QOH\QOH\-500;
112 QENEU\QENEU\-500; QINEU\QINEU\-500;
113 QEIL\QEICL\-500; QI\QI\-500;
114 QE\QE\-500; Qetot\QETOT\-500;
115 Qit\QITOT\-500; qeir\car6\-500;
116 qiir\car64\-500; qex\car53\-500; qix\car54\-500;
117
118 !*******************************************************
119 !-------------------Temporal outputs-------------------
120 !*******************************************************
121 Te0_TE(0.00); Te.1_TE(0.1*roc); Te.5_TE(0.5*roc);
122 TEB_TEB;
123 Ti0_TI(0.00); Ti1_TI(0.1*roc); Ti5_TI(0.5*roc);
124 TIB_TIB;
125 ne0_NEC; neb_NEB;
126 step_HRO;  tau_TAU;
127 q0_1./MUC;   ROC_ROC;          NA1_NA1;
128 amj_amj; aim1_aim1; aim2_aim2; aim3_aim3;
129 zmj_zmj; rtor_rtor; abc_abc; btor_btor;
```

Bibliography

[1] C. Angioni and O. Sauter. “Neoclassical transport coefficients for general equilibria in the banana regime”. In: *Physics of Plasmas* 7 (2000).

[2] C. Angioni et al. “Dependence of the turbulent particle flux on hydrogen isotopes induced by collisionality”. In: *Physics of Plasmas* 25 (2018).

[3] Clemente Angioni. *Theory of Quasi-Linear Transport Models for core transport codes*. 2009.

[4] Clemente Angioni. *Turbulent Transport Theory*.

[5] H. Biglari, P. H. Diamond, and P. W. Terry. “Influence of sheared poloidal rotation on edge turbulence”. In: *Physics of Plasmas* 2 (2007).

[6] Alexander Bock. “Generation and Analysis of Plasmas with Centrally Reduced Helicity in Full-Tungsten ASDEX Upgrade”. PhD thesis. Ludwig-Maximilians-Universität München, 2016.

[7] C. Bourdelle et al. “Core turbulent transport in tokamak plasmas: bridging theory and experiment with QuaLiKiz”. In: *Plasma Physics and Controlled Fusion* 58 (2016).

[8] A. Casati et al. “Validating a quasi-linear transport model versus nonlinear simulations”. In: *Nuclear Fusion* 49 (2009).

[9] J. Citrin et al. “Ion temperature profile stiffness: non-linear gyrokinetic simulations and comparison with experiment”. In: *Nuclear Fusion* 54 (2014).

[10] J. Citrin et al. “Tractable flux-driven temperature, density, and rotation profile evolution with the quasilinear gyrokinetic transport model QuaLiKiz”. In: *Plasma Physics and Controlled Fusion* 59 (2017).

[11] Tilman Dannert and Frank Jenko. “Gyrokinetic simulation of collisionless trapped-electron mode turbulence”. In: *Physics of Plasmas* 12 (2005).

[12] P. H. Diamond et al. “Zonal flows in plasma-a review”. In: *Plasma Physics and Controlled Fusion* 47 (2005).

[13] European Fusion Development Agreement (EFDA). *Tokamak principle*. 2011.

[14] L.-G. Eriksson et al. “Calculations of power deposition and velocity distributions during ICRH: Comparison with experimental results”. In: *Nuclear Fusion* 29 (1989).

[15] E. Fable, C. Angioni, and O. Sauter. “The role of ion and electron electrostatic turbulence in characterizing stationary particle transport in the core of tokamak plasmas”. In: *Plasma Physics and Controlled Fusion* 52 (2010).

[16] E. Fable et al. “Confinement and transport properties during current ramps in the ASDEX Upgrade tokamak”. In: *Nuclear Fusion* 51 (2011).

[17] Emiliano Fable. *ASTRA-7.0. Addendum with changes and new features.* 2012.

[18] R. Fischer. *Private communication*. 2020.

[19] R. Fischer et al. “Integrated Data Analysis of Profile Diagnostics at ASDEX Upgrade”. In: *Fusion Science and Technology* 58 (2010).

[20] T. Fujita et al. “Internal Transport Barrier for Electrons in JT-60U Reversed Shear Discharges”. In: *Physical Review Letters* 78 (1997).

[21] P. Gohil et al. “The torque dependence of the H-mode power threshold in hydrogen, deuterium and helium plasmas in DIII-D”. In: *Nuclear Fusion* 50 (2010).

[22] M. Greenwald et al. “A new look at density limits in tokamaks”. In: *Nuclear Fusion* 28 (1988).

[23] O. Gruber et al. “Physics background of the ASDEX Upgrade project”. In: *Journal of Nuclear Materials* 121 (1984).

[24] T. Hein et al. “Gyrokinetic study of the role of β on electron particle transport in tokamaks”. In: *Physics of Plasmas* 17 (2010).

[25] F. L. Hinton and R. D. Hazeltine. “Theory of plasma transport in toroidal confinement systems”. In: *Reviews of Modern Physics* 48 (1976).

[26] W. Horton, B. G. Hong, and W. M. Tang. “Toroidal electron temperature gradient driven drift modes”. In: *The Physics of Fluids* 31 (1988).

[27] W. A. Houlberg et al. “Bootstrap current and neoclassical transport in tokamaks of arbitrary collisionality and aspect ratio”. In: *Physics of Plasmas* 4 (1997).

[28] N. T. Howard et al. “Multi-scale gyrokinetic simulation of tokamak plasmas: enhanced heat loss due to cross-scale coupling of plasma turbulence”. In: *Nuclear Fusion* 56 (2015).

[29] A.A. Ivanov et al. “New Adaptive Grid Plasma Evolution Code SPIDER”. In: *32 EPS Conference on Plasma Physics*. 2005.

[30] P. Jacquet et al. “ICRH physics and technology achievements in JET-ILW”. In: *EPJ Web of Conferences*. 2017.

[31] B. B. Kadomtsev. “Disruptive instability in Tokamaks”. In: *Soviet Journal of Plasma Physics* 1 (1975).

[32] Hyun-Tae Kim et al. “Statistical validation of predictive TRANSP simulations of baseline discharges in preparation for extrapolation to JET D-T”. In: *Nuclear Fusion* 57 (2017).

[33] J. E. Kinsey, G. M. Staebler, and R. E. Waltz. “The first transport code simulations using the trapped gyro-Landau-fluid model”. In: *Physics of Plasmas* 15 (2008).

[34] Paulett C. Liewer. “Measurements of microturbulence in tokamaks and comparisons with theories of turbulence and anomalous transport”. In: *Nuclear Fusion* 25 (1985).

[35] A. Loarte et al. “H-mode plasmas in the Pre-Fusion Plasma Operation 1 phase of the ITER Research Plan”. In: *Nuclear Fusion* (to be published).

[36] T C Luce. “An analytic functional form for characterization and generation of axisymmetric plasma boundaries”. In: *Plasma Physics and Controlled Fusion* 55 (2013).

[37] A. Manini et al. “Role of T_e/T_i and ∇v_{tor} in ion heat transport of ASDEX Upgrade H-mode plasmas”. In: *Nuclear Fusion* 46 (2006).

[38] P. Manz, M. Ramisch, and U. Stroth. “Physical Mechanism behind Zonal-Flow Generation in Drift-Wave Turbulence”. In: *Physical Review Letters* 103 (2009).

[39] Y. R. Martin, T. Takizuka, and ITPA CDBM H-mode Threshold Database Working Group. “Power requirement for accessing the H-mode in ITER”. In: *Journal of Physics: Conference Series* 123 (2008).

[40] R. M. McDermott et al. “Core momentum and particle transport studies in the ASDEX Upgrade tokamak”. In: *Plasma Physics and Controlled Fusion* 53 (2011).

[41] G. McKee et al. “Impurity-Induced Suppression of Core Turbulence and Transport in the DIII-D Tokamak”. In: *Physical Review Letters* 7 (2000).

[42] Motoki Nakata et al. “Isotope Effects on Trapped-Electron-Mode Driven Turbulence and Zonal Flows in Helical and Tokamak Plasmas”. In: *Physical Review Letters* 118 (2017).

[43] ITER Organization. *ITER Research Plan within the Staged Approach (Level III - Provisional Version)*. 2018.

[44] V. V. Parail and G. V. Pereverzev. “Internal disruption in a tokamak”. In: *Soviet Journal of Plasma Physics* 6 (1980).

[45] A. G. Peeters et al. “Erratum: "Influence of the centrifugal force and parallel dynamics on the toroidal momentum transport due to small scale turbulence in a tokamak"”. In: *Physics of Plasmas* 19 (2012).

[46] A. G. Peeters et al. “Influence of the centrifugal force and parallel dynamics on the toroidal momentum transport due to small scale turbulence in a tokamak”. In: *Physics of Plasmas* 16 (2009).

[47] A. G. Peeters et al. “The nonlinear gyro-kinetic flux tube code GKW”. In: *Computer Physics Communications* 180 (2009).

[48] A.G. Peeters. *The physics of fusion power*. 2008.

[49] G.V. Pereverzev and P.N. Yushmanov. *ASTRA. An Automated System for TRansport Analysis*. 2002.

[50] G.V. Pereverzev et al. *ASTRA. An Automatic System for Transport Analysis in a Tokamak*. 1991.

[51] Alexander Piel. *Plasma Physics. An Introduction to Laboratory, Space, and Fusion Plasmas*. Second edition. Springer, 2017.

[52] U. Plank et al. “H-mode power threshold studies in mixed ion species plasmas at ASDEX Upgrade”. In: *Nuclear Fusion* 60 (2020).

[53] E. Poli, A. G. Peeters, and G. V. Pereverzev. “TORBEAM, a beam tracing code for electron-cyclotron waves in tokamak plasmas”. In: *Computer Physics Communications* 136 (2001).

[54] Emanuele Poli. *Plasma Physics: Fundamentals*.

[55] F. Porcelli, D. Boucher, and M. N. Rosenbluth. “Model for the sawtooth period and amplitude”. In: *Plasma Physics and Controlled Fusion* 38 (1996).

[56] E. Righi et al. “Isotope scaling of the H-mode power threshold on JET”. In: *Nuclear Fusion* 39 (1999).

[57] F. Ryter et al. “Experimental Study of Trapped-Electron-Mode Properties in Tokamaks: Threshold and Stabilization by Collisions”. In: *Physical Review Letters* 95 (2005).

[58] F. Ryter et al. “Experimental evidence for the key role of the ion heat channel in the physics of the L-H transition”. In: *Nuclear Fusion* 54 (2014).

[59] F. Ryter et al. “Survey of the H-mode power threshold and transition physics studies in ASDEX Upgrade”. In: *Nuclear Fusion* 53 (2013).

[60] M. Schmidtmayr et al. “Investigation of the critical edge ion heat flux for L-H transitions in Alcator C-Mod and its dependence on B_T”. In: *Nuclear Fusion* 58 (2018).

[61] Bruce D. Scott. “Tokamak edge turbulence: background theory and computation”. In: *Plasma Physics and Controlled Fusion* 49 (2007).

[62] V. D. Shafranov. “Equilibrium of a toroidal pinch in a magnetic field”. In: *Atomic Energy* 13 (1962).

[63] G. M. Staebler et al. “A model of the saturation of coupled electron and ion scale gyrokinetic turbulence”. In: *Nuclear Fusion* 57 (2017).

[64] G. M. Staebler et al. “Geometry dependence of the fluctuation intensity in gyrokinetic turbulence”. In: *Plasma Physics and Controlled Fusion* (to be submitted).

[65] G. M. Staebler et al. “The role of zonal flows in the saturation of multi-scale gyrokinetic turbulence”. In: *Physics of Plasmas* 23 (2016).

[66] U. Stroth, P. Manz, and M. Ramisch. “On the interaction of turbulence and flows in toroidal plasmas”. In: *Plasma Physics and Controlled Fusion* 53 (2011).

[67] Ulrich Stroth. “Plasma Physics. Confinement, Transport and Collective Effects”. In: Springer, 2005. Chap. Transport in Toroidal Plasmas.

[68] R. E. Waltz, J. C. DeBoo, and M. N. Rosenbluth. “Magnetic-Field Scaling of Dimensionally Similar Tokamak Discharges”. In: *Physical Review Letters* 65 (1990).

[69] A. A. Ware. “Pinch effect for trapped particles in a tokamak”. In: *Physical Review Letters* 25 (1970).

[70] J. Weiland, A. B. Jarmén, and H. Nordman. “Diffusive particle and heat pinch effects in toroidal plasmas”. In: *Nuclear Fusion* 29 (1989).

[71] M. Weiland et al. “RABBIT: Real-time simulation of the NBI fast-ion distribution”. In: *Nuclear Fusion* 58 (2018).

[72] Yuhong Xu. “A general comparison between tokamak and stellarator plasmas”. In: *Matter and Radiation at Extremes* 1 (2016).

[73] X. Yang et al. “Core tungsten transport in WEST long pulse L-mode plasmas”. In: *Nuclear Fusion* 60 (2020).

[74] Emiliano Fable et al. “Novel free-boundary equilibrium and transport solver with theory-based models and its validation against ASDEX Upgrade current ramp scenarios”. In: *Plasma Physics and Controlled Fusion* 55 (2013).

[75] M. Ono et al. “Exploration of spherical torus physics in the NSTX device”. In: *Nuclear Fusion* 40 (2000).

[76] M. Schneider et al. “Modelling one-third field operation in the ITER pre-fusion power operation phase”. In: *Nuclear Fusion* 59 (2019).

[77] S.Yu. Medvedev et al. “The negative triangularity tokamak: stability limits and prospects as a fusion energy system”. In: *Nuclear Fusion* 55 (2015).

Name: Christian Karl Kiefer Student number: 830643

Declaration

I hereby certify, that this work has been composed by myself and that no other than the mentioned sources were used. All sections of that work that use quotes or describe an argument developed by another author have been referenced.

Ulm, ...

Christian Karl Kiefer